Supplementary Information for "Quasi-Optic, Radio Frequency Joint Wireless Power Transfer and Edge Smart Sensing"

Mahmoud Wagih[1]*, Sitong Mu[1], Thomas Whittaker[2], William Whittow[2]

[1] University of Glasgow, Green RF-Enabled Electronics Lab, James Watt School of Engineering, Glasgow, G12 8QQ, United Kingdom
[2] Loughborough University, Wireless Communications Research Group, Wolfson School of Mechanical, Electrical, and Manufacturing Engineering, Loughborough, LE11 3TU, United Kingdom

*Mahmoud.Wagih@Glasgow.ac.uk

This supplementary file includes information and detailed figures about:

1. Comparison with Other Electromagnetic WPT and Passive Energy Harvesting Sensing Approaches
2. Comparison with Lens-Based/High-Gain RF WPT Systems, and 3D-Printed Lens Antennas
3. Lens and Feeding Antenna Design and Characterization
4. 2D Radiation Patterns at 5.6 and 5.8 GHz, for Different Feeds
5. Rectifier Design Details and Characterisation
6. Rectifier Large-Signal Characterisation
7. Rectenna Wireless Measurement Setup and Results
8. SAR Analysis and User Safety
9. Series Voltage Summation, and Multi-Rectenna Lens Feed.
10. Indoor Propagation Analysis and Path-Loss Exponent Reduction
11. End-to-End System Efficiency
12. Regulatory and multi-frequency operation
13. Bluetooth Sensor Powering and Associated DC Power Levels.
14. Joint Power and Sensing Setup with Antenna-Based Sensitivity Enhancement
15. Breathing Sensing Details and Signal Processing
16. Machine Learning-Assisted Sensing Setup and Classification Approach
17. Impact of the Lens on Accuracy and Results Summary
18. Localization Results Along a Vertical Path
19. Horizontal Localization Results
20. Time-Varying Data and Real-Time Detection
21. ML Training Data Size and Accuracy
22. Power Consumption of the Edge RF Sensing Receiver
23. Supplementary Video Descriptions

Supplementary Note 1. Comparison with Other Electromagnetic WPT Approaches

The radar plot of the technologies evaluation is explained in Supplementary Table 1, with Supplementary Table 2 detailing the scoring criteria.

Supplementary Table 1. Detailed comparison of the proposed system with other wireless power approaches illustrated in Figure 1(b).

	Integrated Sensing	**Scalability to Different Operation Environments**	**Resilience Against Obstructions**	**Wireless Range**	**Angular Coverage**	**Representative References**
This Work: Quasi-Optic RF Power and Sensing	**5:** ML-enabled localization in different indoor environments	**3:** multi-path mitigated through reflections from the environment and multi-beam collection	**3**: under 50% power loss observed in the investigated long-range powering environment	**4**: Up to 30 m EIRP-compliant range for powering Bluetooth sensors; >20x receiver radius	**4**: 60° half-power beamwidth in Azimuth and Elevation planes	This work
Optical power transfer (Laser)	**1:** Not reported	**5**: not dependent on or affected by an unobstructed channel	**1**: link blocked by any LoS objects. Safety/tracking required for high-power systems	**5**: >30 m range demonstrated in safe / low-power systems with 0.1 mW output; typically tested on resistive loads only.	**0**: point-to-point links only	[S1], [S2]
Omnidirectional RF power transfer	**1:** Possible based on similar technologies, e.g. RFID, but not demonstrated as a join sensing/power receiver	**2**: power transfer strongly affected by ground reflections	**2**: influenced by people / LoS obstructions[S11]; around 10 dB degradation expected	**3**: demonstrated up to 10 m at 915 MHz [S4] and 2.4 GHz [S5] using up to 6 dBi gain and multiple rectennas. Link 10x array radius.	**5**: harvesters demonstrated with full spherical 3D coverage	[S3]-[S8]
Quasistatic Fields	**1:** Not reported	**0**: fully-enclosed/shielded space required for power transfer	**5**: Unaffected by passing people and/or obstacles inside the power transfer zone	**2**: up to 1.5 m in an enclosed 3x3x2 m test room with full shielding	**2**: operation dependent on the orientation of receiving coils	[S9]-[S10]

Supplementary Table 2. Evaluation criteria for the wireless power systems compared in Figure 1(b).

	Wireless power system features				
Score (From Figure 1b)	**Integrated Sensing**	**Scalability to Different Operation Environments**	**Resilience against Obstructions**	**Wireless Range**	**Angular Coverage**
0	Not feasible	Operation only possible in a controlled / engineered environment	Fully blocked with any LoS obstructions	<1 cm, contact required	<1°: Single-point
1	Sensing feasible based on enabling technologies, but not demonstrated	Operation highly dependent on multi-path environments	Major blockage; potential safety mechanisms required	1 cm - 1 m. Receiver size comparable to the link distance	10°
2	Component demonstration	Transferrable to different environments, but multi-path effects strongly influence the link	Power loss >50%, system operation interrupted	1-5 m. Multiple wavelengths link	>60°
3	Post-processing of sensor data	Multi-path mitigation available	Observable power loss up to 50%. Safe for people interrupting the WPT path	5-10 m. Up to 10x antenna/ receiver radius	60-90° Single-plane coverage (azimuth or elevation)
4	System demonstration in controlled environment	Minimal influence of the surroundings, structure	Minimal power losses when obstructed (<50%)	10-20x antenna/receiver radius	60-90°: Full 2D coverage in azimuth and elevation
5	Full demonstration in multiple relevant environments and applications	Unaffected by multi-path propagation; non-diffracting	Unaffected by objects / people in LoS	Range independent of receiver size or wavelength	>90°: Full spherical coverage for random angles of incidence

Supplementary Note 2. Comparison with Lens-Based/High-Gain RF WPT Systems, 3D-Printed Lens Antennas, and RFID-type sensors.

The existing reports of lens-based rectennas (2D or 3D) are compared in Supplementary Table 3. While some reports did not include experimental validation of the integration system, they are included for completion.

Supplementary Table 3. Comparison of lens-based RF wireless power demonstrations.

	Frequency (GHz)	EIRP (dBm)	Max distance (m)	Power at max d (mW)	Type of Lens	Test Conditions	Notes and assumptions
This work	5.6	55	10	1.2	3D-printed Fresnel Lens	Indoor, echoic & anechoic	Distance sweep; statistical analysis; power combining in RF and DC. DC power at 33 m indoors, with capacitive load
	5.6	55	33	0.2			
[S11]	28	57.1	0.8	15.2	3D-printed GRIN Lens	Indoor, semi-anechoic	Distance approximated from Figure
[S12]	28	65	7	0.5	Planar Rotman Lens	Indoor	Single sweep measurement
[S13]	28	65	18	0.01		Indoor, corridor	
[S14]	40	55	10	0.64	3D Luneberg Lens	Indoor, single distance	Distance extrapolated based on power density for a 55 dBm EIRP, similar to our work
[S15]	94	50	0.05	10.4	Dielectric lens	Anechoic chamber	Based on chamber measurements
[S16]	3.5	20	3	0.006	PCB Metalens	Indoor and chamber	Range limited by -20 dBm at the lens-free rectenna; EIRP estimated based on gain values
[S17]	Antenna only introduced/simulated - no rectenna demonstration				Dielectric lens	n/a	n/a

As the proposed lens-based rectenna required miniaturisation beyond state-of-the-art, to enable its realisation for 5.6-5.8 GHz wireless power transfer. A comparison with recent lens antennas (not proposed for wireless power applications) is presented below. The miniaturisation is demonstrated primarily through the thickness and the focal length, while maintaining a comparable aperture efficiency to other higher volume prototypes.

It is key to note that the focus of this work is not to implement a new lens antenna design. However, the demonstrated improvements in the sensing accuracy and in the received power levels, with power combining behind the lens, open the way to new applications in lens antennas in sensing, power transfer, and communication. The findings could be extended to higher frequencies yielding further physical size reduction, in both the lens's volume and its focal distance.

Supplementary Table 4. Comparison with other reported lens antennas.

Work	Lens Type	Design or Centre Freq. (GHz)	Freq. range (GHz)	λ (m)	Radius		Thickness		Focal Length from centre		Cylindrical Volume		Max Meas Gain (dB)	Max Meas Gain improve-ment (dB)	Max Aperture Efficiency (%)	Material	E_r	TanD	Print method
					mm	λ	mm	λ	mm	λ	m^3	λ^3							
This paper	Fresnel Lens	5.70	5.6 - 5.8	0.053	123	2.34	44.2	0.84	120	2.28	2.101E-03	14.41	18.5	11.00	32.834	Premix ABS440	4.4	0.004	FDM
[18]	Shaped GRIN	13.40	13.4	0.022	60	2.68	50	2.23	80	3.57	5.655E-04	50.39	N/A	N/A	40.306	Visijet Amber	2.686	0.00168	MJP
[19]	Graded Fresnel	20.00	18 - 26.5	0.015	175.2	11.68	15	1.00	75	5.00	1.446E-03	428.38	33	N/A	37.040	Somos Nanotool	3.356	0.015	SLA
[20]	Flat GRIN	15.00	12 - 18	0.020	60	3.00	18.5	0.93	159.3	7.96	2.092E-04	26.15	24	11	70.696	PLA	2.72	0.008	FDM
[21]	Flat - transform-ed hyperbolic lens	30.00	26.5 - 40	0.010	38	3.80	12	1.20	43.3	4.33	5.444E-05	54.44	21	N/A	22.084	Premix ABS1200	12	0.004	FDM
[22]	Flat Luneberg	15.00	12 - 18	0.020	35	1.75	10	0.50	47	2.35	3.848E-05	4.81	19.1	9.1	67.230	Ceramic (MgTiO3)	17.1	0.0002	Ceramic / likely not printed
[23]	Luneberg	10.00	8 - 12	0.030	60	2.00	120	4.00	60	2.00	1.357E-03	50.27	20.3	N/A	67.855	Polymer	2.7	0.02	MJP
[24]	Transform-ed Luneberg	15.20	12.4-18	0.020	54	2.74	104	5.27	52	2.63	9.527E-04	123.92	23.6	N/A	N/A	FR4 & F4B	2.65 & 4.4	0.001 & 0.025	PCB (not 3D printed)
[25]	Meta-material lens	9.50	7-12	0.032	72	2.28	12	0.38	100.8	3.19	1.954E-04	6.21	21	9.5 (Average)	61.344	RO4350B	3.48	N/A (<0.005)	PCB (not 3D printed)

Other passive sensing systems are compared below, in Supplementary Table 5. The key difference is in the sensing taking place at the edge device, using the rectenna as a detector, and using an edge ADC to resolve the RF-DC waveforms.

Many RFID implementations were reported for various sensing applications. However, they have the same issue as radar, in the sensing taking place at the base-station, with the tags' response being read from RSSI data, which can be easily interpreted by other unintended receivers. However, the proposed approach of JSAP could be entirely implemented at the edge device with local processing, limited only by the power consumption and energy storage on the receiver.

The concept of using a rectifier as a voltage detector was explored recently in [S35], where the power consumption of standard receivers, e.g. wi-fi, was cited as a key limitation. This was demonstrated using off-the-shelf RF power receivers using standard omnidirectional antennas, with the sensing primarily shown in short, line-of-sight links, under 2 m away.

Supplementary Table 5. Comparison with other reported RF sensing approaches, with a focus on battery-free tags.

Reference	**Approach**	**Frequency (GHz)**	**RF Detection**	**Reader power (W)**	**Range (m)**	**Notes on reader power**
This work	Rectenna (JSAP), edge sensor + ML	5.6	Edge: RSSI only	10	12	ADC power consumption + BLE advertisement on RX. TX power only for PA
	Rectenna, edge sensor + FFT			10	4.2	
[S26]	RFID tags on-body	0.868	Basestation: from backscattered RFID RSSI / phase	13	4	3 W idle reader power, 13 W active for 30 dBm
[S27]	RFID, thermistor, on-body	0.868		5.5	0.6	Thingmagic reader with CP antenna
[S28]	knitted rfid onbody	0.868		13	1	Speedway reader with standard patch antenna
[S29]	Knitted RFID, movement	0.868		5	0.88	Power not reported; min RFID reader assumed
[S30]	fall prediction, contactless; wall	0.868		15	3	Impinj R720 reader
[S31]	RFID temperature sensor	0.868		5	0.4	Estimated based on battery life of the reader
[S32]	mmWave retrodirective tag, chipless	24	Basestation: broadband s-parameters using VNA + PA	400	30	VNA-based reader including power amplifiers, power consumption at least 100 W
[S33]	Rader, multi-subject vital signs monit	7.3-8	Bistatic radar	8	5.4	Author-reported power data
[S34]	Radar, occupancy (commercial)	3-10	Monostatic radar	0.02	3.5	3.5 m radius at 3 m ceiling; Novelda UWB radar

The key differences, from an architectural standpoint, compared to RFID-based, battery-free sensing are illustrated in Figure 1. The RFID approach relies on the reader (also the power source) to resolve the backscattered signal's RSSI. This raises a number of limitations including the availability of open RSSI data to eavesdropping, as well as limiting the RF sensing performance to a single RSSI per tag. This has led to various RFID sensing systems using arrays of tags.

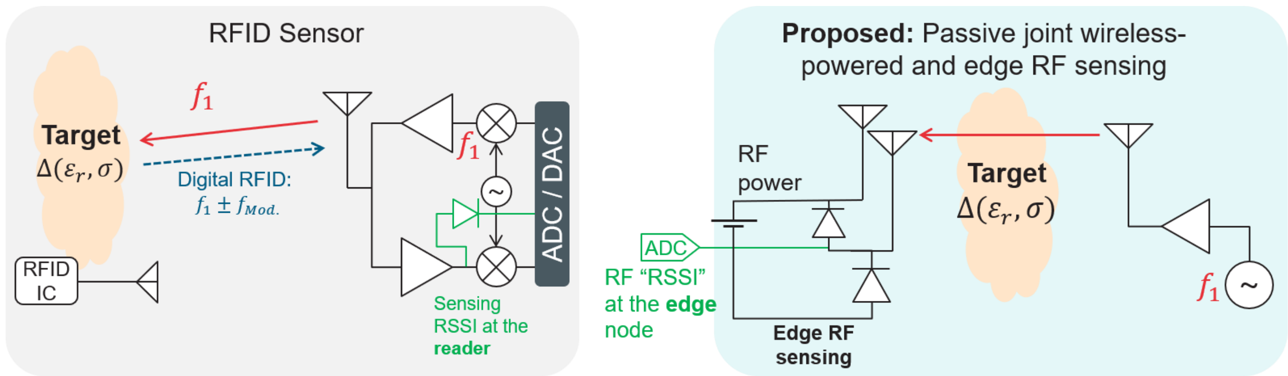

Functionality	RFID (State-of-art)	Proposed Quasi-optic Edge Sensing
Sensing range	Limited by tag turn-on power – typically 10 m	Limited by rectifier's detection range and ADC noise floor; demonstrated at 20 m+
Number of sensing antennas	1 per tag	n channels per node (limited by ADC channels or MUX); 8 in the proposed ML systen
Beamwidth and angular selectivity	>60º (typically omnidirectional)	<10º Accuracy enhanced by >20% through the quasi-optic focusing
RSSI Security	Backscatter signal strength can be sniffed on other receivers	RSSI confined to the edge receiver and not backscattered.

Supplementary Figure 1. High-level comparison of the proposed edge sensing and conventional RFID-based backscatter sensors.

RSSI Sampling at the Receiver:

By sampling the RF power levels at the receiver, indicated by a rectifier stage's output, the RSSI could be resolved without additional hardware at the edge receiver. This approach is built on a widely explored concept in other energy harvesting modalities, where the power output of the energy harvester could be used to infer changes in its surroundings, e.g. shadowing of a photovoltaic cell [S36, S37]. The adoption of this approach in the RF energy harvesting or wireless power transfer domain remains limited, as seen in the review in [S36].

At a theoretical network level, the concept of a power sampling receiver was proposed and modelled, showing its impact on the energy harvesting [S38]. The majority of the reported theoretical approaches focused on configuring the transmitting base-station to combine sensing and power transfer waveforms [S39]. This approach is similar to ISAC/JSAC based on radar-like waveforms. Nevertheless, experimental demonstrations of sensing at the receiver remained limited to investigations using off-the-shelf RF power receivers, operating at a short range [S40].

The detailed sensor evaluation in different environments, with and without machine learning, in Supplementary Notes 13-17 demonstrate the enhanced accuracy achievable through the antenna design. The results demonstrate the potential advantages over RFID in terms of spatial selectivity, due to the multi-receiver and quasi-optic beamforming, and the passive gain enhancement which increases the sensing range using the antenna gain.

Supplementary Note 3. Lens and Feeding Antenna Design and Characterization.

The printed Fresnel lens uses the PREPERM's ABS440 filament, whose relative permittivity is specified to be 4.4. This was experimentally verified for a printed sample using a single-post dielectric resonator, whose measured response is shown in Supplementary Figure 2. Supplementary Figure 3 shows the layout of the printed lens.

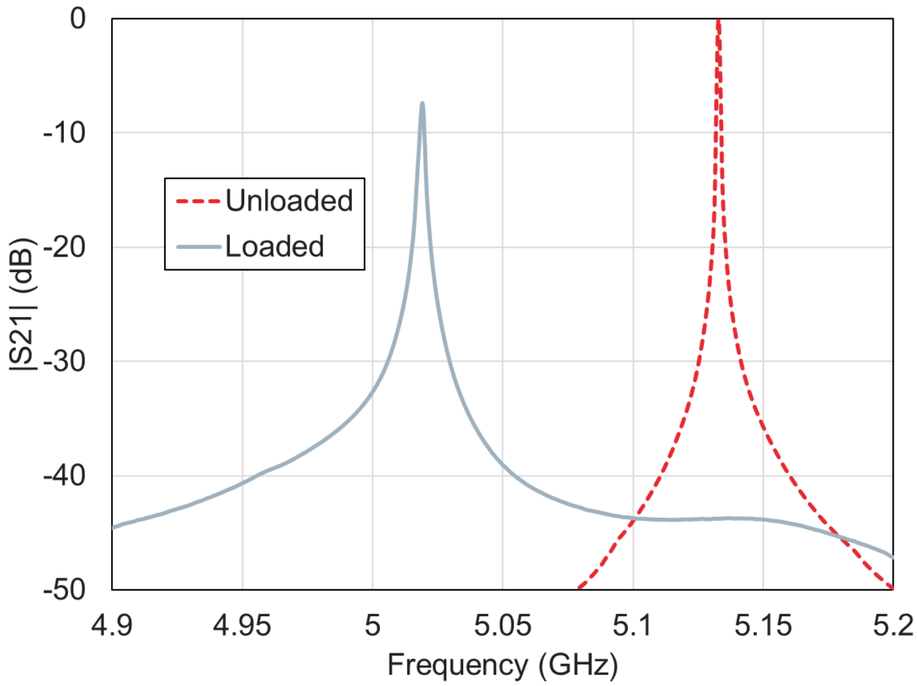

Supplementary Figure 2. Measured split-post dielectric resonator response with and without the 3D-printed sample.

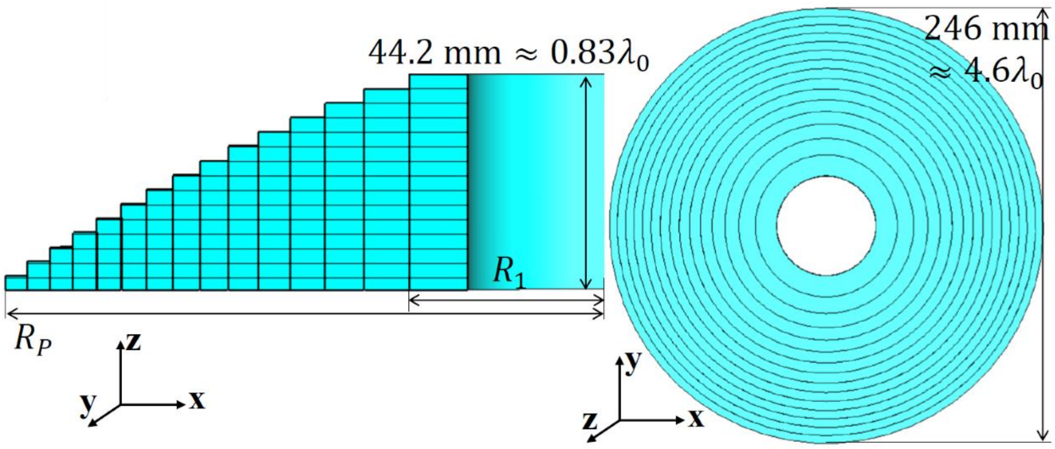

Ring no. (Inner first)	R1	R2	R3	R4	R5	R6	R7	R8	R9	R10	R11	R12	R13	R14	R15	R16
Ring outer radius (mm)	28	39.9	49.2	57.2	64.3	70.9	77.1	82.9	88.5	93.8	99.0	104	108	113	118	123
ε_r	4.4															
Ring height (mm)	0	44.2	41.2	38.3	35.3	32.4	29.5	26.5	23.6	20.6	17.7	14.7	11.8	8.8	5.9	2.9

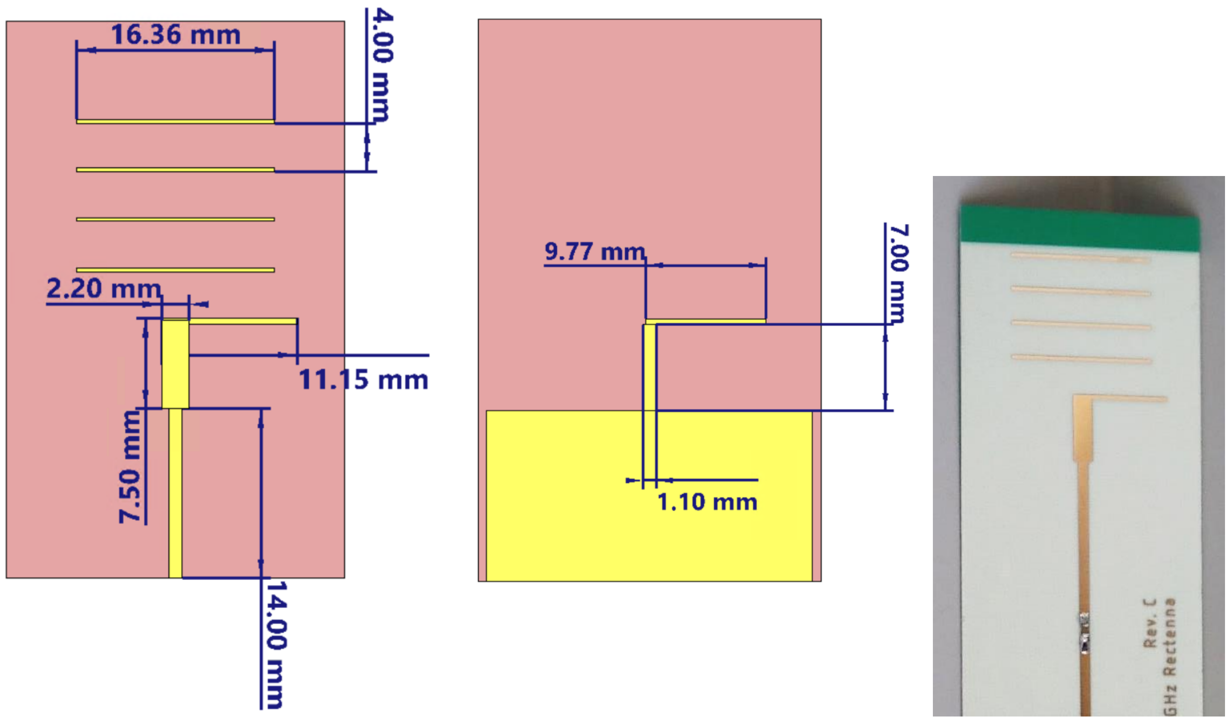

Supplementary Figure 3. The designed Fresnel lens and feeding Yagi antenna dimensions.

The dimensions of the fabricated end-fire planar Yagi-Uda-inspired dipole are shown in Supplementary Figure 3. The number of directors was chosen to achieve a gain in excess of 6 dB, creating a nearly 60º beamwidth, feeding the lens. In an array, the antennas are closely coupled with electrically unconnected grounds, to allow series DC combining between the rectifiers. The antennas are implemented on the same Rogers 4350B substrate as the rectifier.

Supplementary Figure 4 shows the measured input reflection coefficient of the antenna, and the mutual coupling (|S21|) between two adjacent antennas, in the array configuration used.

Supplementary Figure 3. Layout and dimensions of the Yagi-Uda-inspired dipoles used in the rectennas.

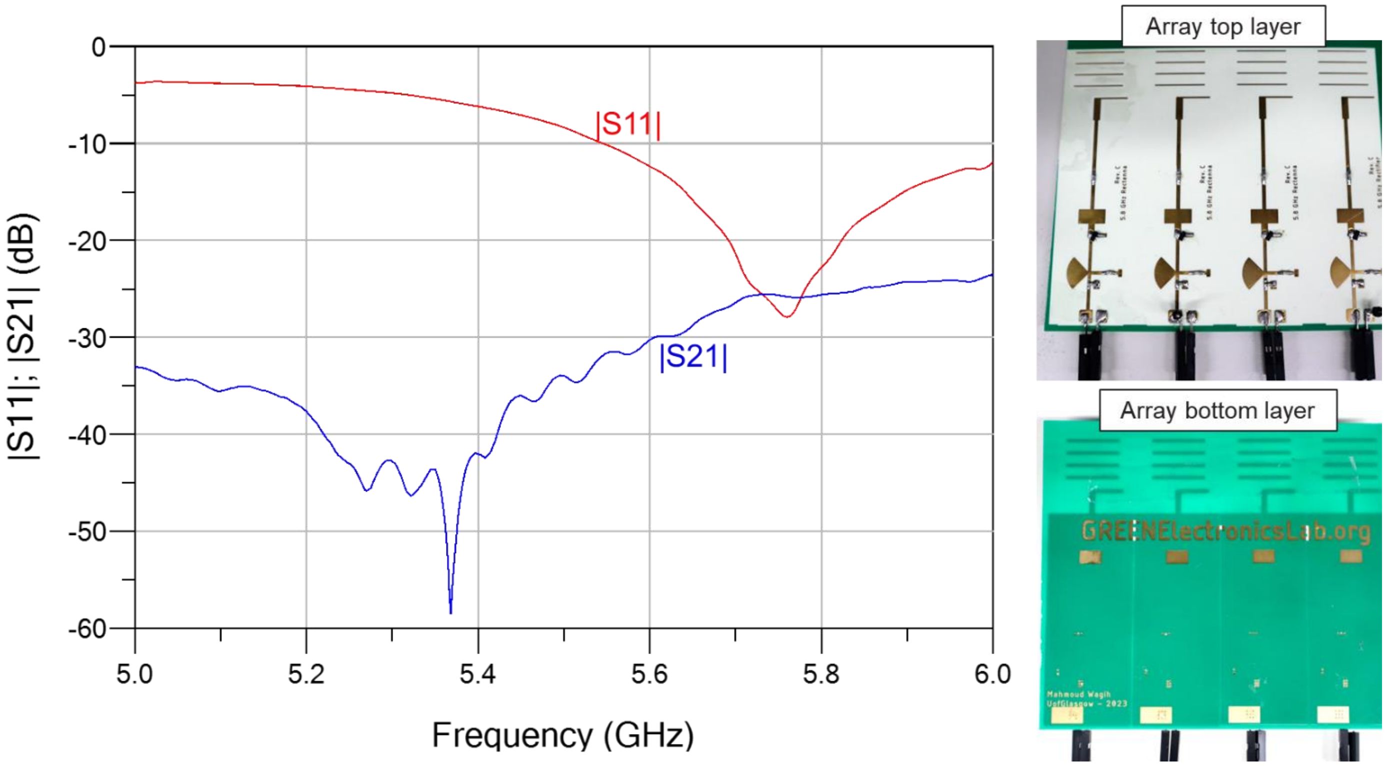

Supplementary Figure 4. Measured s-parameters of the antenna, showing a matched bandwidth between 5.6 and 6 GHz, and the inter-element coupling in the array configuration.

Supplementary Note 4. 2D Radiation Patterns at 5.6 and 5.8 GHz, for Different Feeds.

The measured normalised radiation patterns are illustrated in Supplementary Figures 5-7.

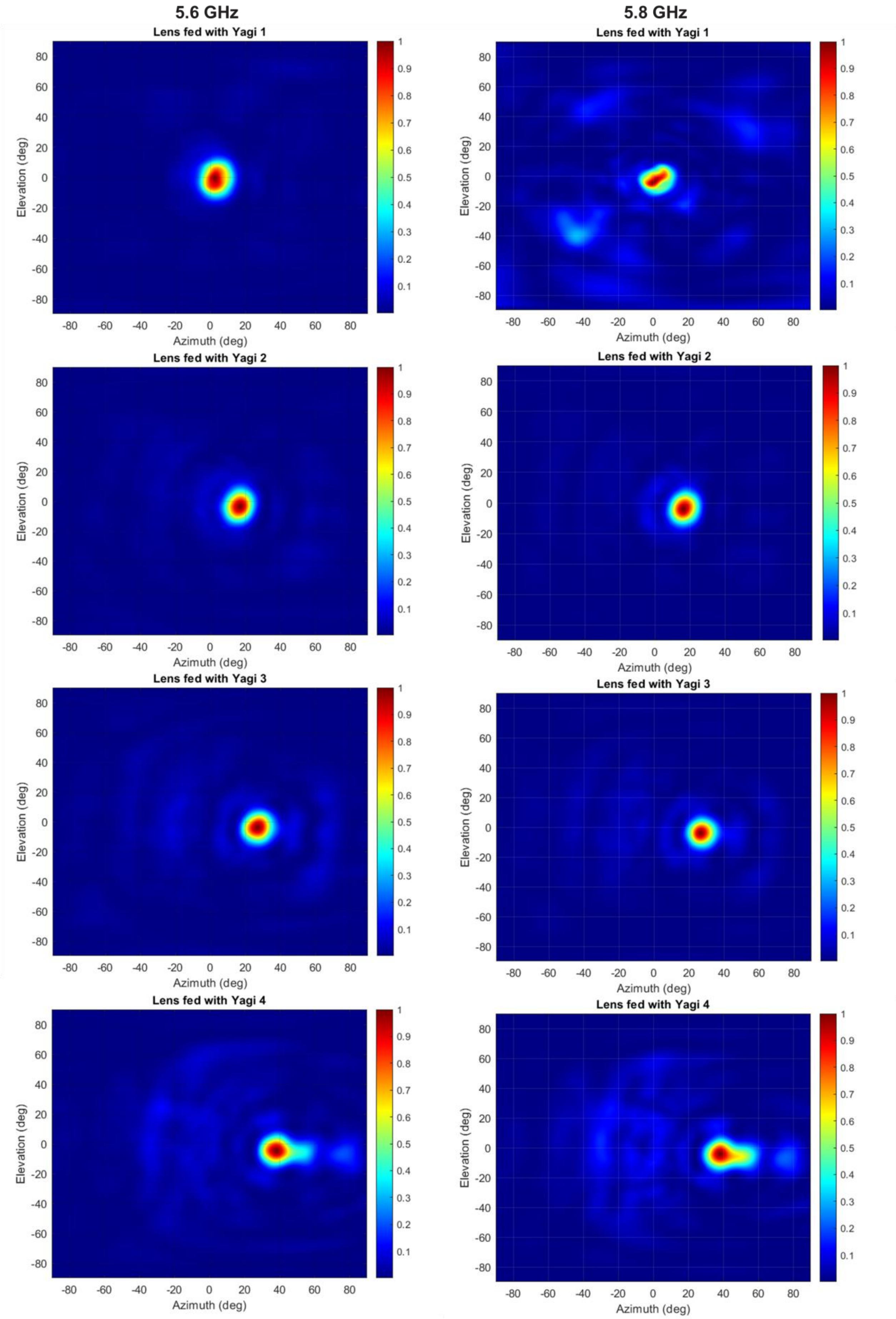

Supplementary Figure 5, measured radiation patterns showing the 2D beam steering using the four horizontally-offset Yagis, at 5.6 and 5.8 GHz, for 4 feeding antennas.

For different feeding positions and feeding antennas, the focused beams exhibit high similarity. This is demonstrated in Supplementary Figures 7 for an open-ended waveguide feed, alongside the more compact and lower in cost, proposed planar feed.

5.6 GHz

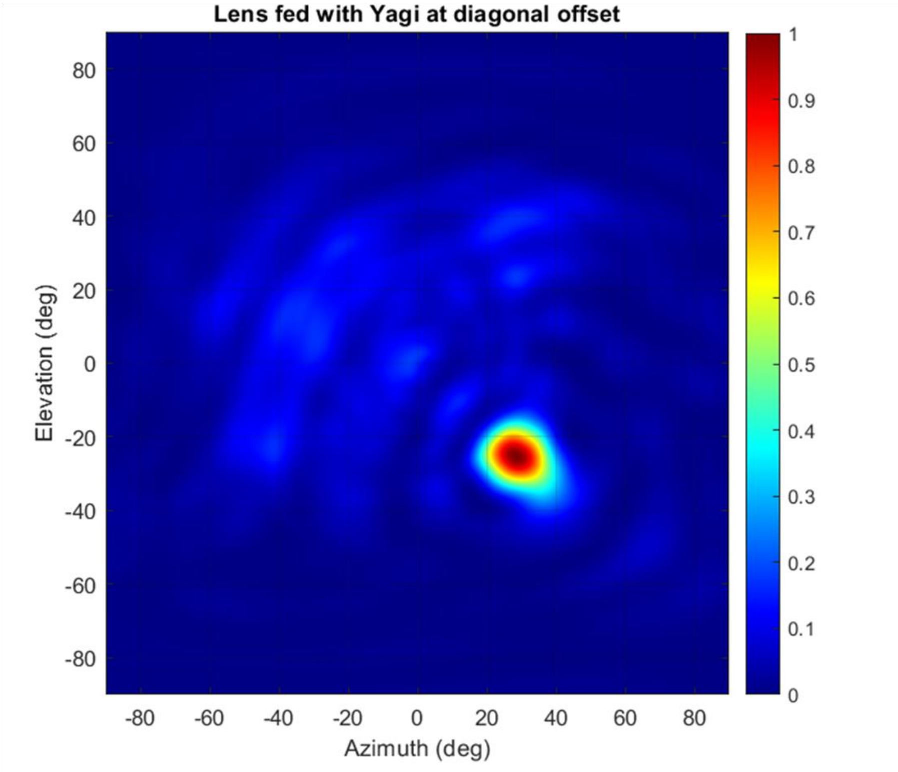

5.8 GHz

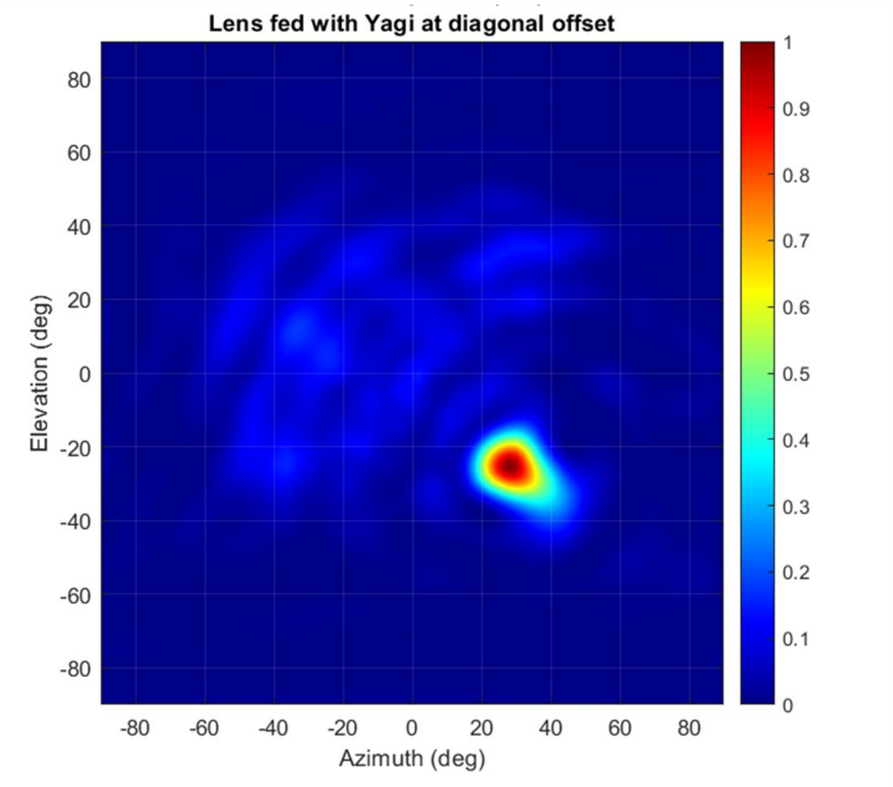

Supplementary Figure 6. 2D beam scanning demonstration using diagonally-offset Yagi feeds, at 5.6 and 5.8 GHz.

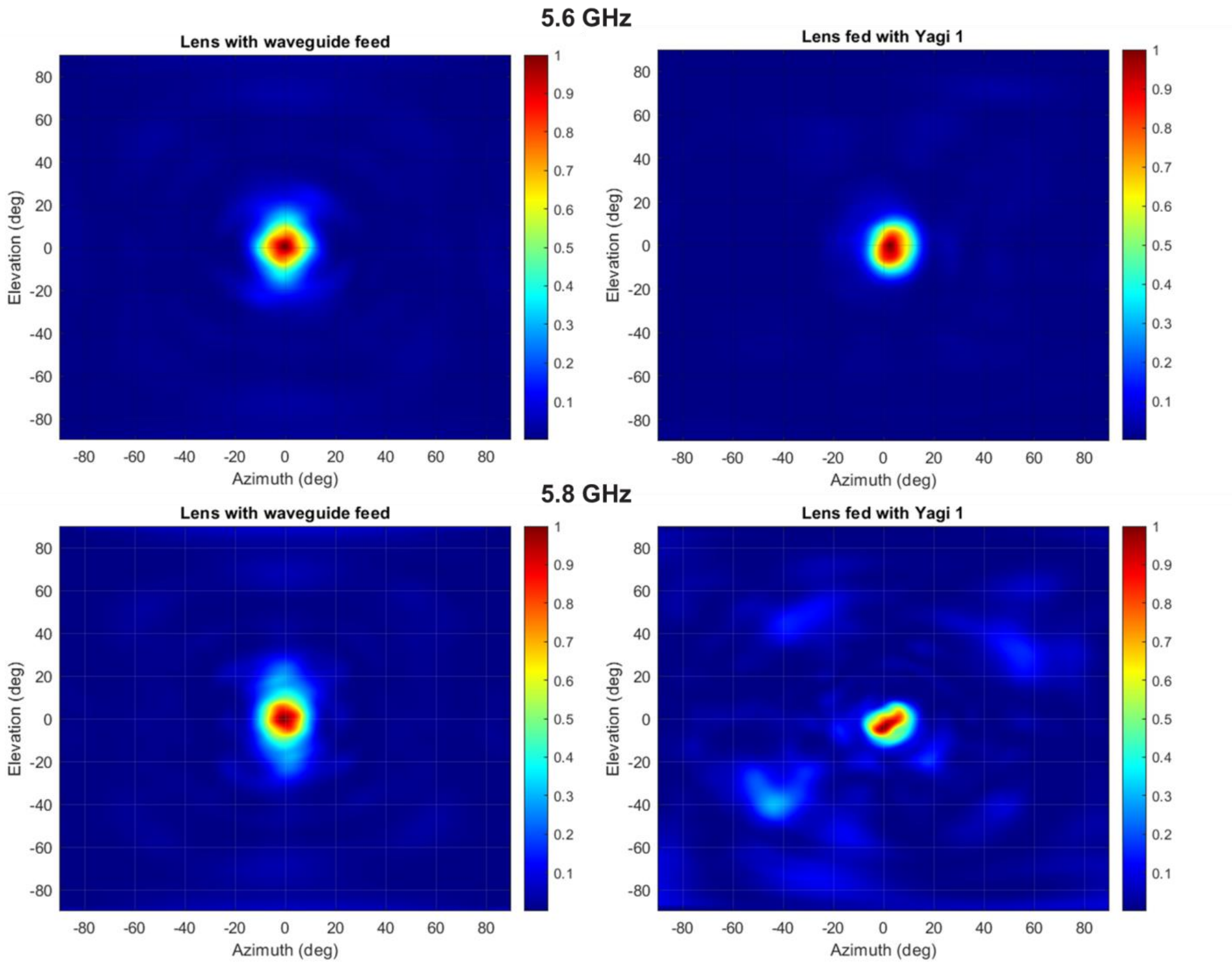

Supplementary Figure 7. Comparison of the normalised radiation pattern with a WR187 open-ended waveguide feed and using the Yagi antennas adopted in the rectenna array.

Supplementary Note 5. Rectifier Design Details and Characterisation

The rectifier design is based on a shunt diode rectifier with microstrip matching and harmonic termination at the output. The design was implemented on a mainstream Rogers 4350b PCB with a 0.76 mm thickness. Supplementary Figure 8 shows the layout and dimensions, and a photograph of the rectifier.

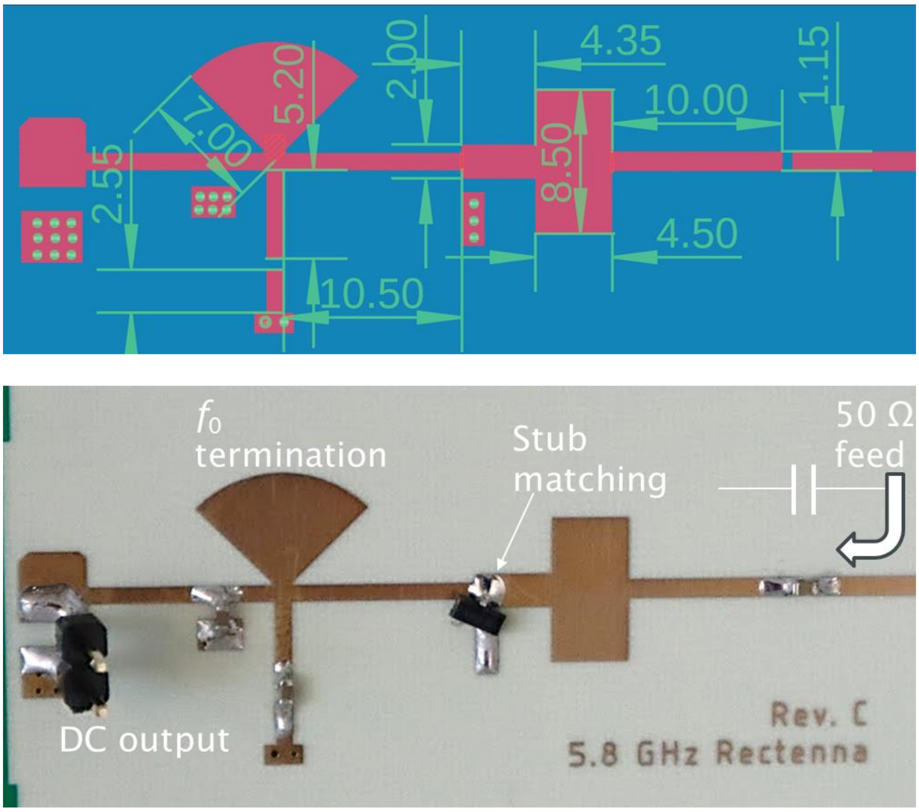

Supplementary Figure 8. Rectifier layout and dimensions (in mm), and photograph of the implemented prototype.

The diode used is the BAT15-04R, owing to its low forward voltage and relatively high breakdown voltage of 4 V, allowing a DC output of up to 4 V to be achieved per rectenna element. The efficiency seen in Figure 3(b) is predominantly limited by the diodes' losses and is in line with state-of-the-art rectifiers operation around 5.6 or 5.8 GHz [S11-S12]. Higher power conversion efficiencies could be achieved by using specialist diodes, e.g., VDI ZBD.

Supplementary Note 6. Rectifier Large-Signal Characterisation

Prior to performing the power measurements, the matching of the rectifier was evaluated using large-signal s-parameters, at varying input power levels and load impedances. Owing to the non-linearity of the diode, its RF input impedance will vary depending on the DC current passing through its junction, and based on the input RF power level. Supplementary Figure 9 shows the measured S11 response, both magnitude and input impedance, for the expected load conditions.

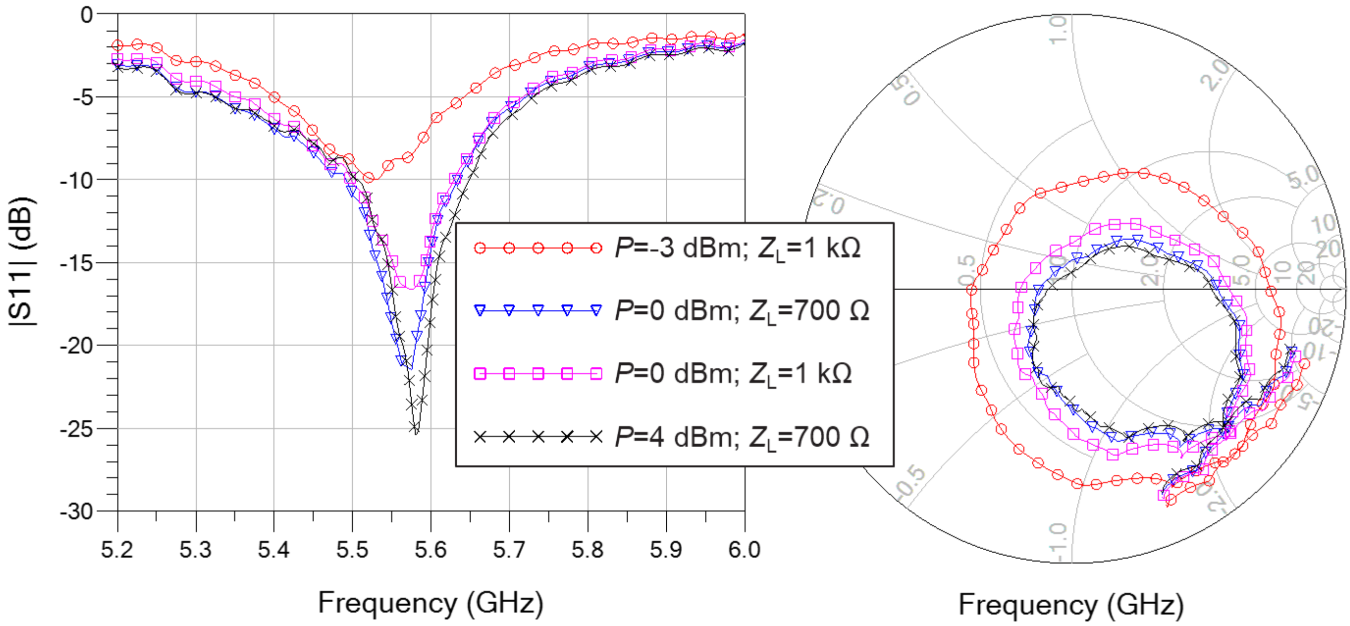

Supplementary Figure 9. Measured S11 response of the rectifier at varying input power levels and load conditions.

For the maximum power level available from the VNA (1.5 dBm) the DC current and RF-DC efficiency as a function of the load voltage level are shown in Supplementary Figure 11. From these results, the maximum efficiency is observed for a 0.661 V output, corresponding to a 1 kΩ load impedance. As a result, all further wireless-powering experiments were performed with a 1 kΩ load, except where a capacitor is directly charged to power the load.

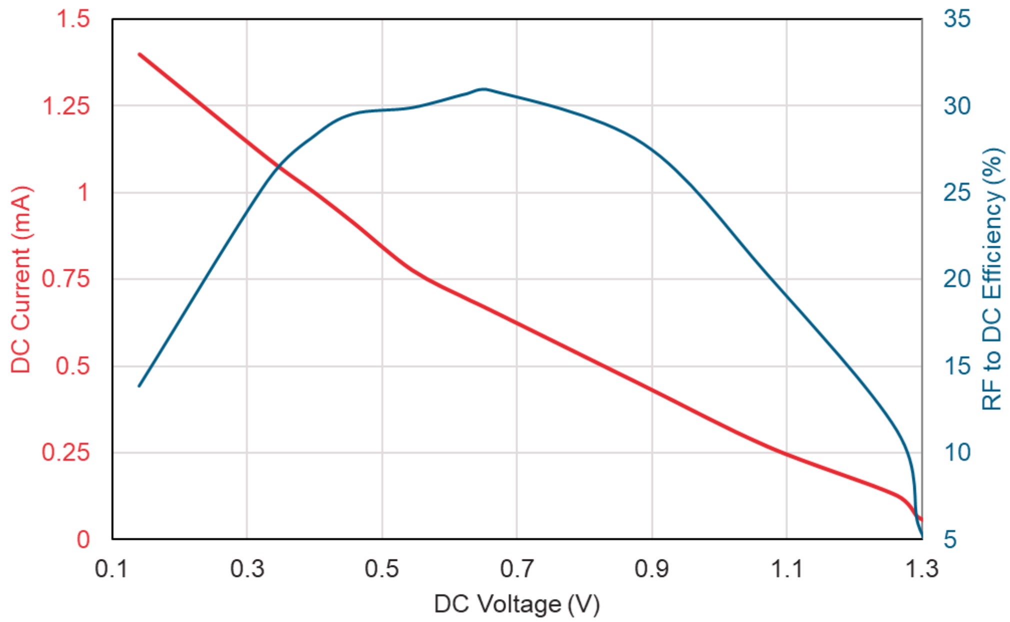

Supplementary Figure 10. Measured DC output as a function of varying load conditions.

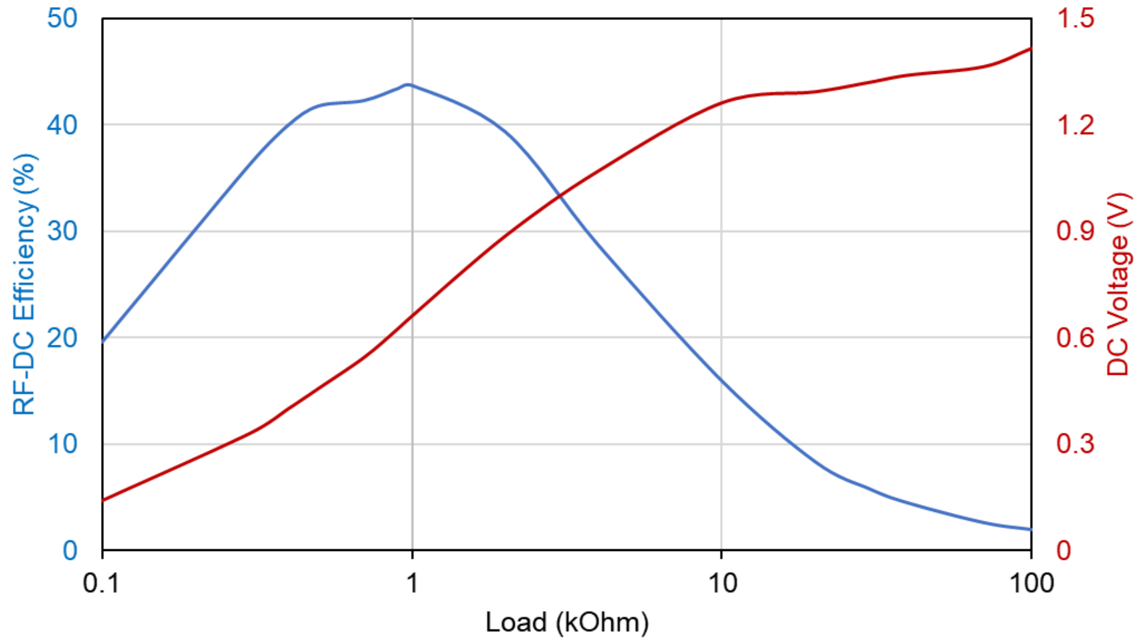

Supplementary Figure 11. The DC power output and voltage level at approximately 1.5 dBm input to the rectifier.

Supplementary Note 7. Rectenna Wireless Measurement Setup and Results

The integrated wireless rectenna was characterised using a gain-standard dual-ride horn antenna, as a transmitter, fed by a 5 W power amplifier. The input to the amplifier

A 4-channel oscilloscope was used to monitor the DC output voltage over a fixed load impedance for all rectennas. The received power level was calculated as

$$P_{RX} = \frac{P_{TX}G_{TX}}{4\pi d^2} \times A_{eff}$$

where A_{eff} is the effective area of the rectenna, and $P_{TX}G_{TX}$ represent the equivalent isotropic radiated power (EIRP) of the transmitter, at distance d. The RF to DC power collection efficiency, in Figure 3(e), is calculated as:

$$\text{RFDC Efficiency} = \frac{P_{DC}}{P_{RX}}$$

To verify the accuracy of this method, to ±1 dB, the channel gain between the horn and the dipoles was measured using a VNA through the S21.

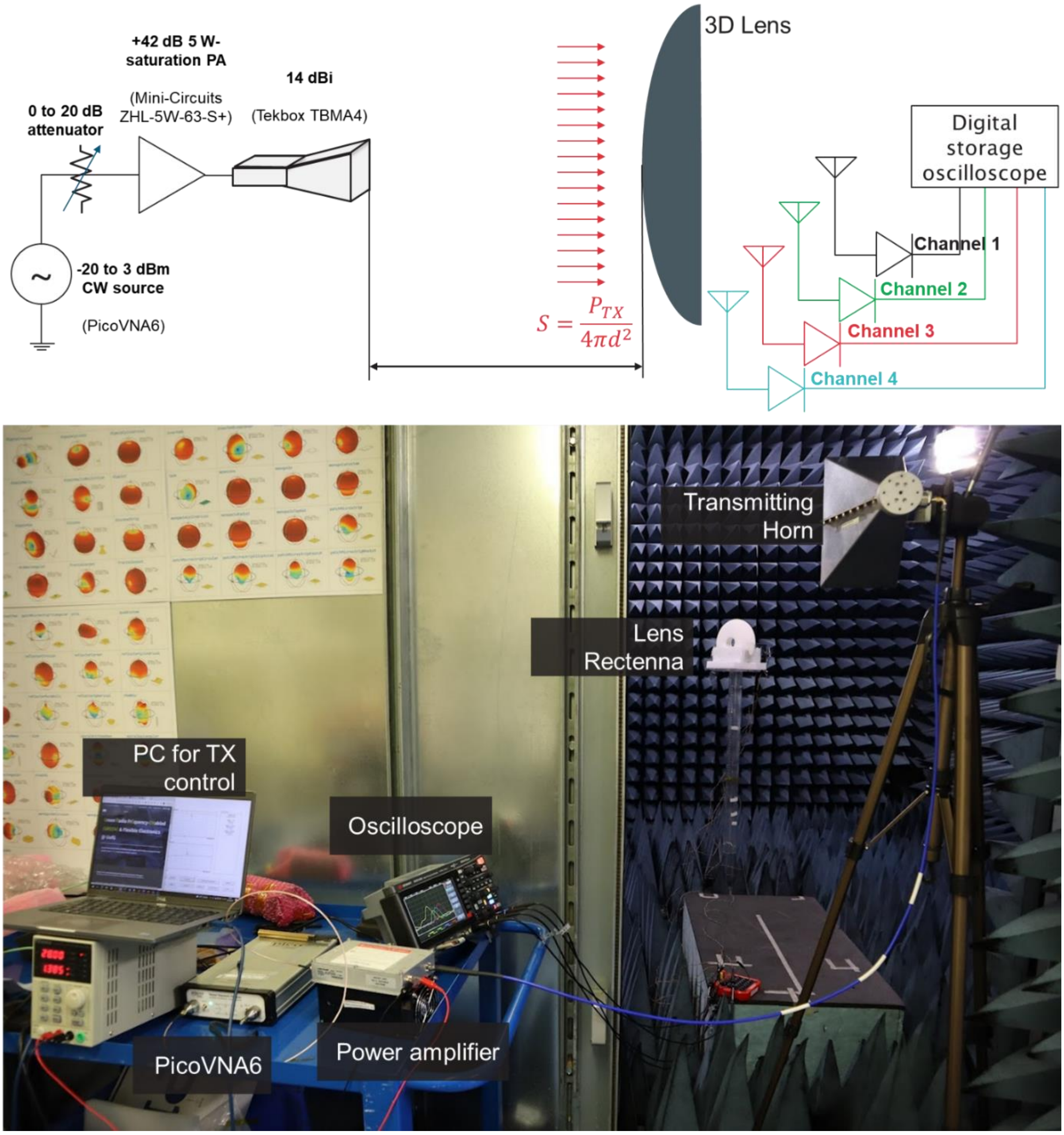

Supplementary Figure 13. Details of the measurement setup in the anechoic chamber.

The measured DC power output and DC voltage for varying input power densities are shown in Supplementary Figures 14 and 15, at 5.6 GHz and across 1 kΩ load.

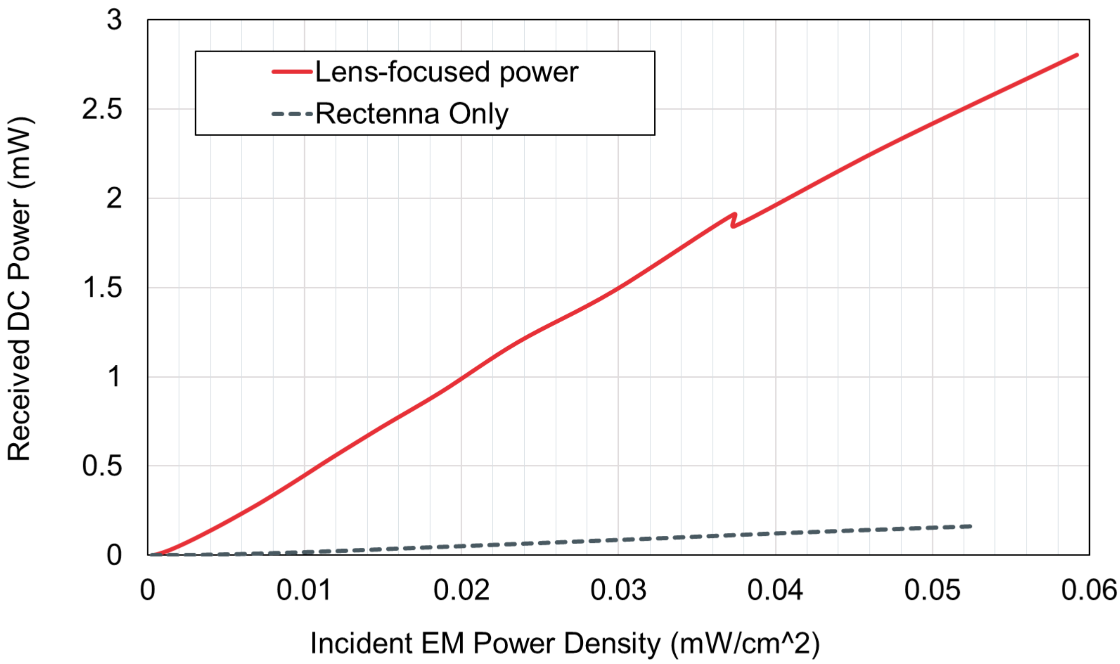

Supplementary Figure 14. measured DC power output as a function of the incident power density, with and without the lens focusing, for a single receiver in the anechoic chamber.

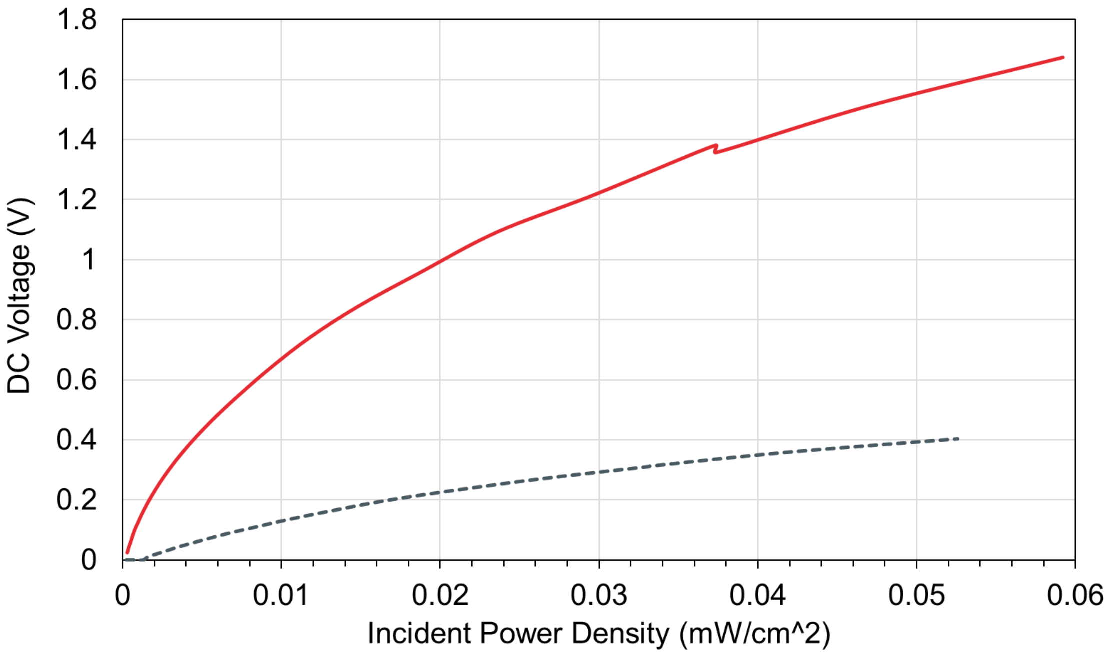

Supplementary Figure 15. measured DC power output as a function of the incident power density, with and without the lens focusing, for a single receiver in the anechoic chamber.

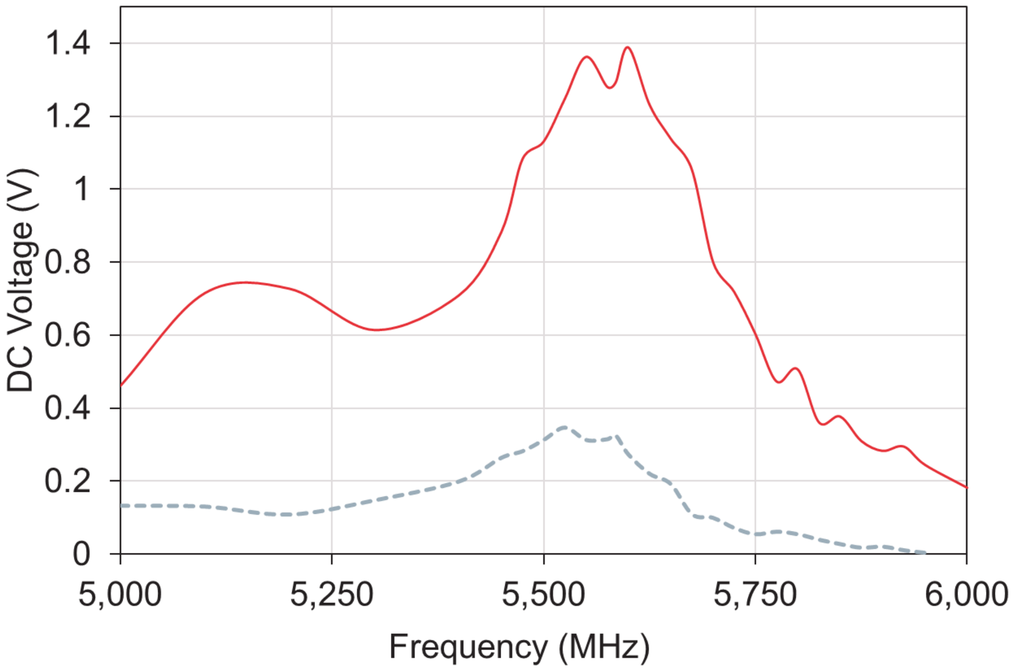

Supplementary Figure 16. measured DC voltage output as a function of the incident power density, with and without the lens focusing; the power is shown in Main Text Figure 3(f).

Supplementary Note 8. Series Voltage Summation, and Multi-Rectenna Lens Feed.

To harness the multi-path effects to improve the power received by the rectenna, the output of different numbers of rectenna elements was combined in series for voltage summation. The measurement setup is shown in Supplementary Figure 17.

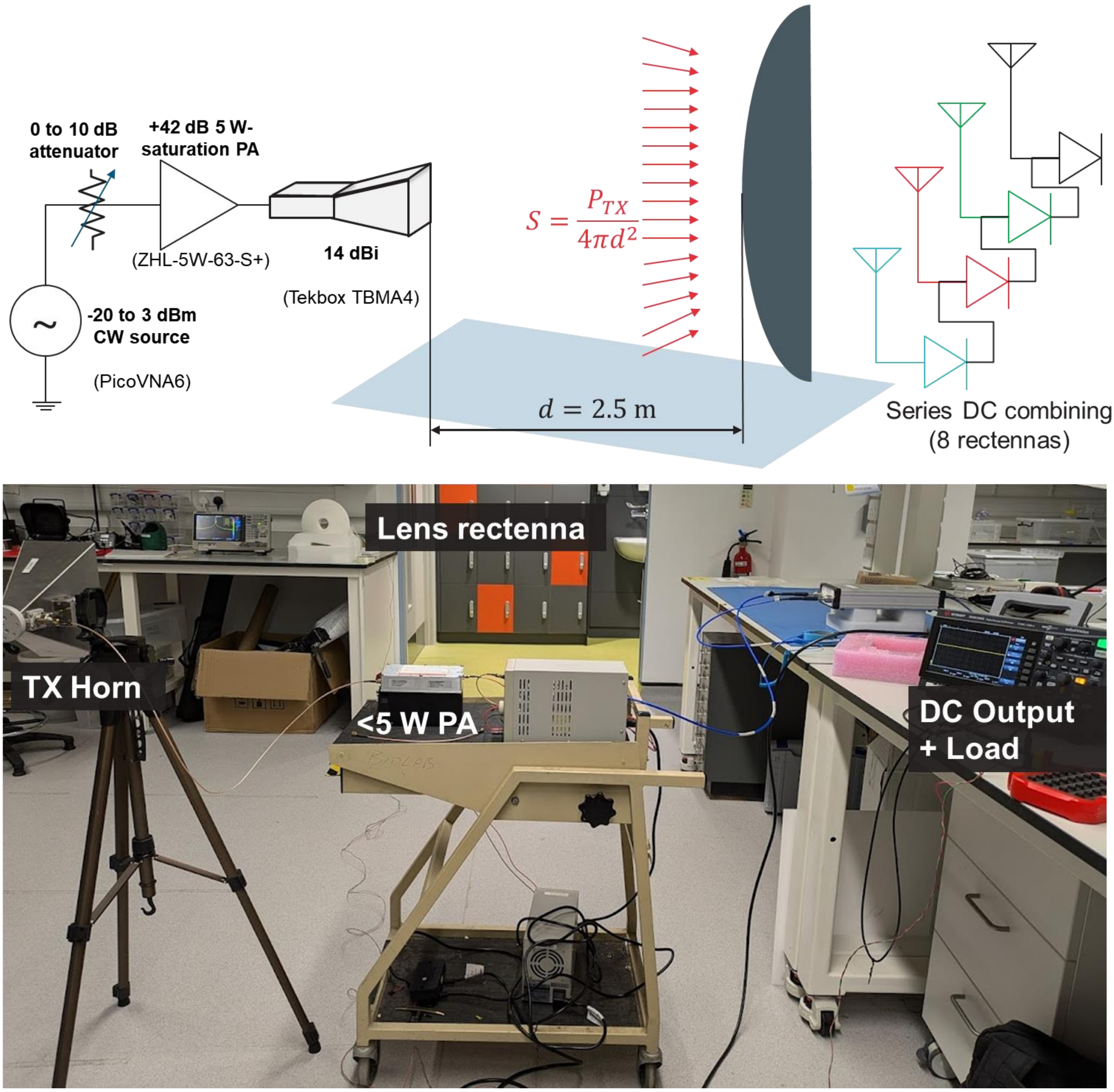

Supplementary Figure 17. the reflective indoor environment testing setup for the lens rectenna, to illustrate the benefits of DC combining behind the lens.

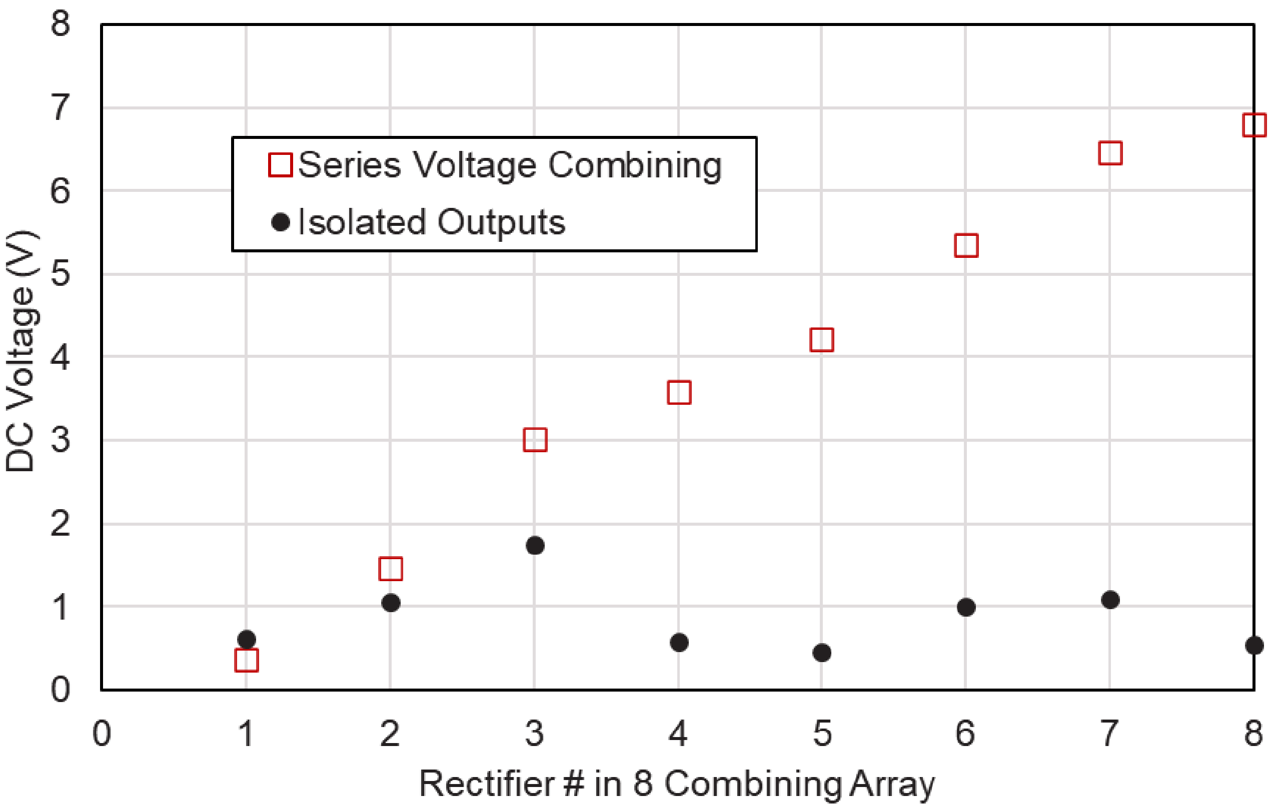

Supplementary Figure 18. Measured enhancement in the received power through combining the output of multiple rectifiers.

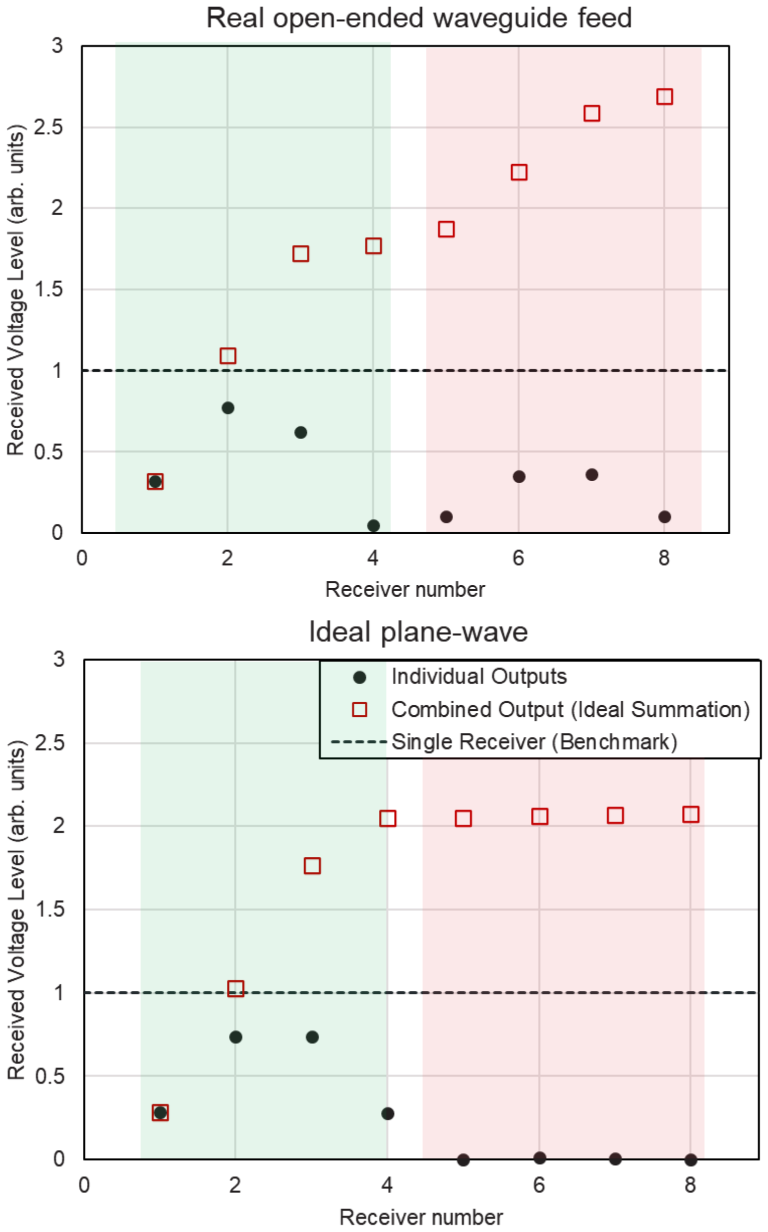

(a)

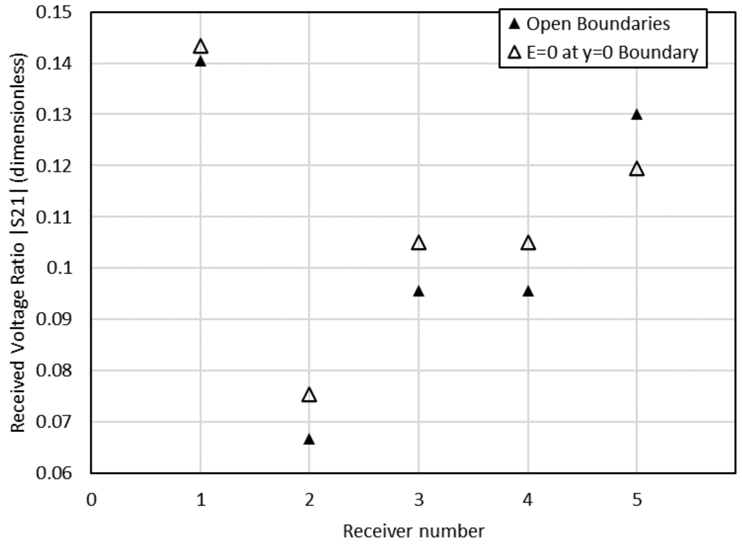

(b)

Supplementary Figure 19. Simulated power combining effects: (a) comparison of the ideal power summation for a waveguide/plane-wave feed; the shaded regions show the centre (green) and top (red) rows of rectennas. (b) Received voltage level on 5 waveguide ports behind the lens; open (non-reflective) and PEC boundaries were explored in the minimum z direction (emulating ground reflections).

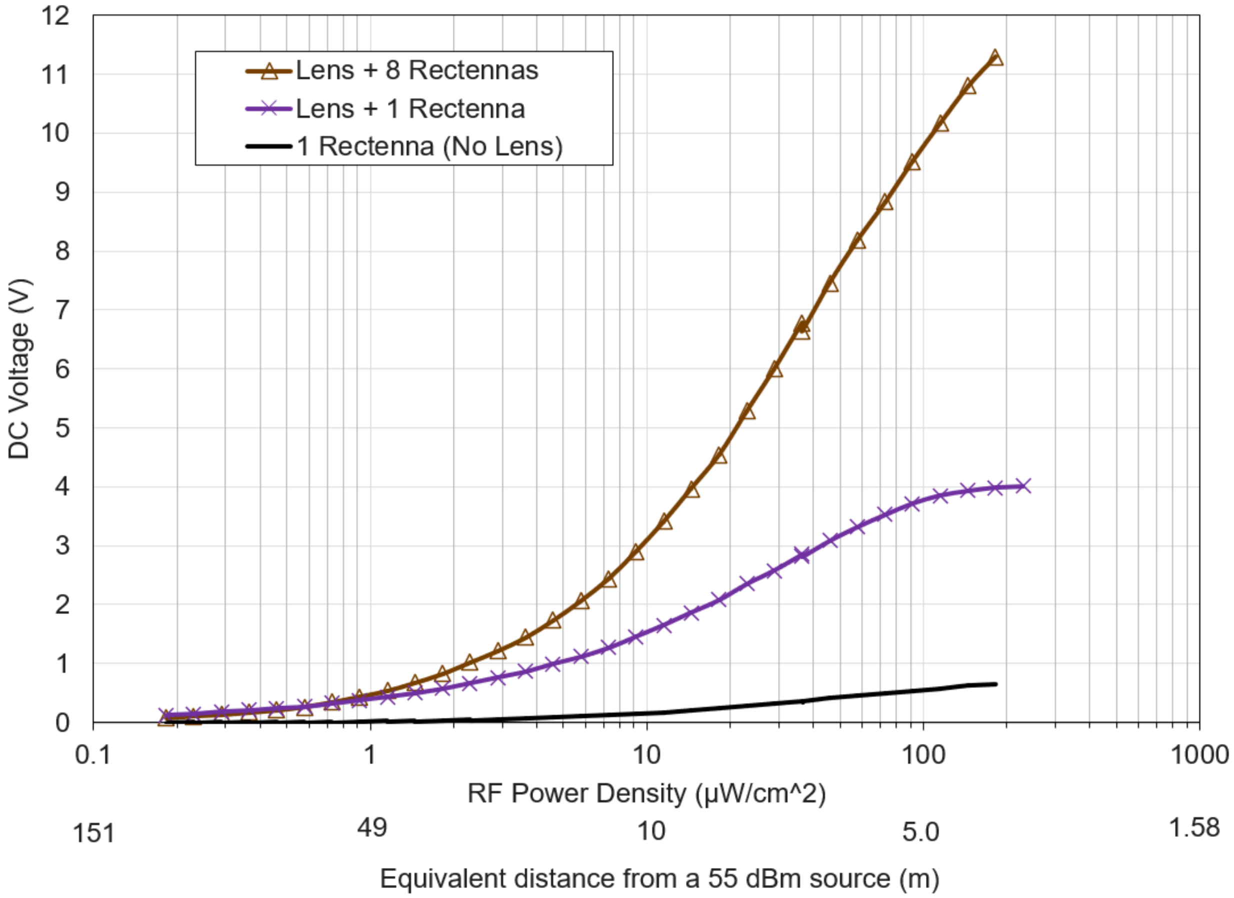

(a)

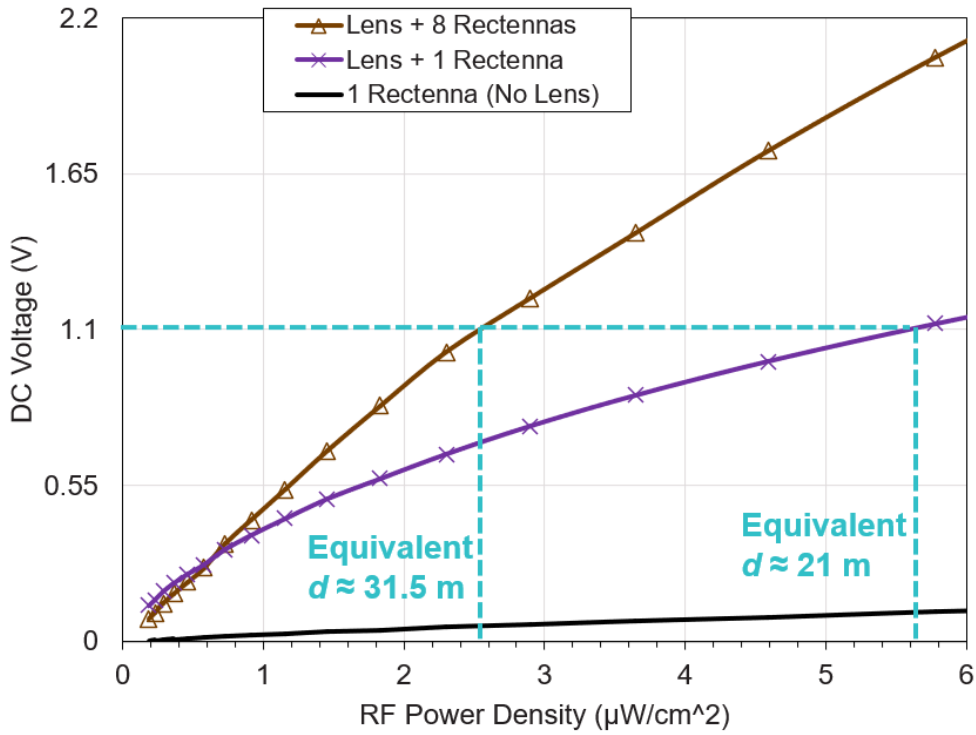

(b)

Supplementary Figure 20. (a) The DC voltage output across a 1 MΩ load (approximating the open-circuit/low-current load conditions) for the different rectennas/combining arrangements explored. The lens+8 rectennas scenario most closely resembles the long-range powering experiments in Figure 4.(b) Illustration of the estimated maximum operation distances for a 1.1 V load, representing the IN100 Bluetooth tag used in the long-range powering experiments.

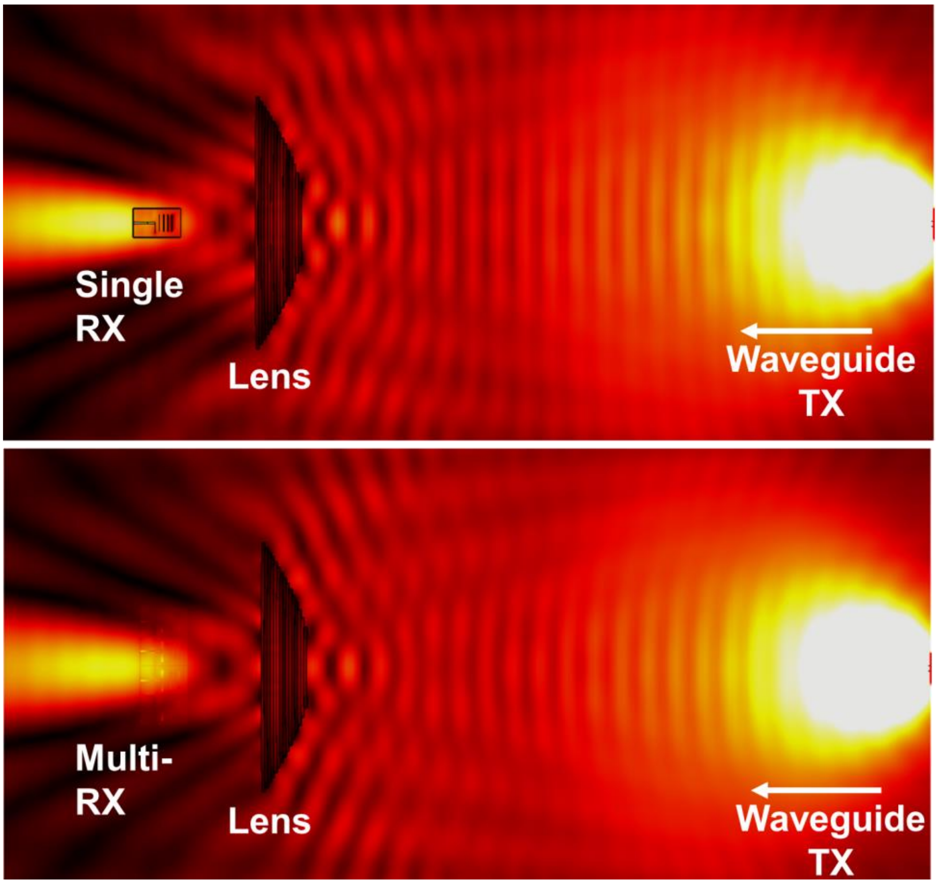

(a)

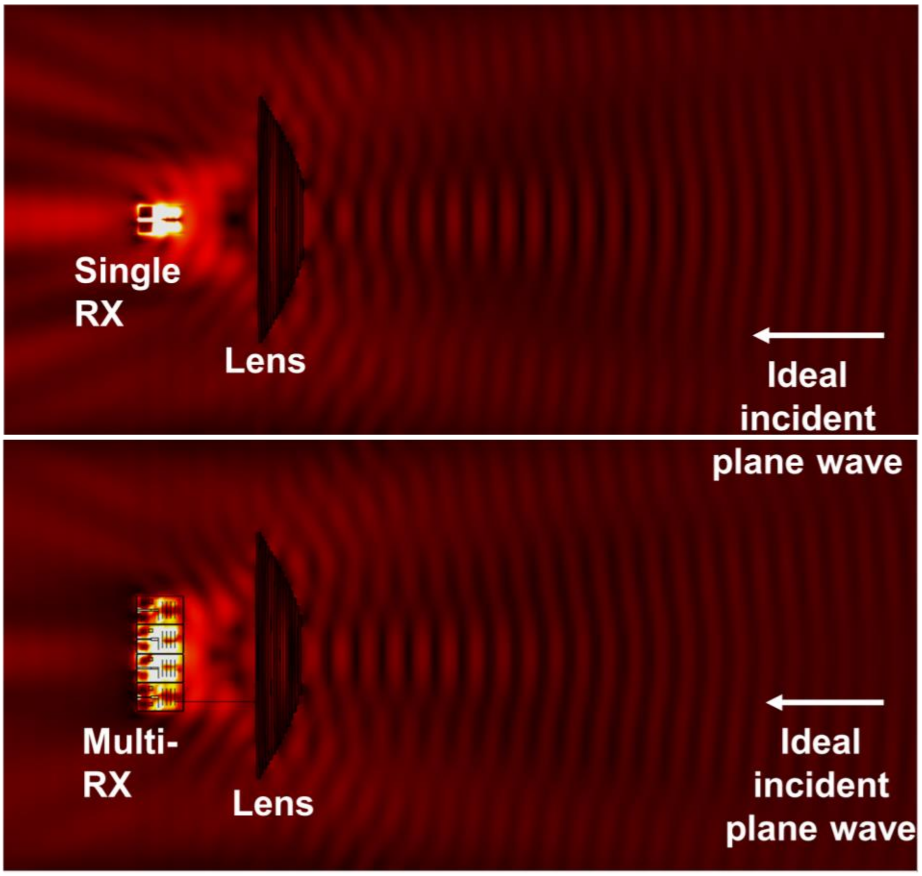

(b)

Supplementary Figure 21. Simulated maximum E-fields around the lens, for (a) a practical waveguide feed, and (b) an ideal incident plane wave. Both results show how the harvested power level can be enhanced through the use of multiple receivers, with further enhancement for the semi-spherical incident wave.

The DC voltage summation affects the optimum load, with the inclusion of the lens allowing a higher DC current output to be obtained, evident through the reduction in the optimum load impedance compared to the 8-rectenna array (without the lens).

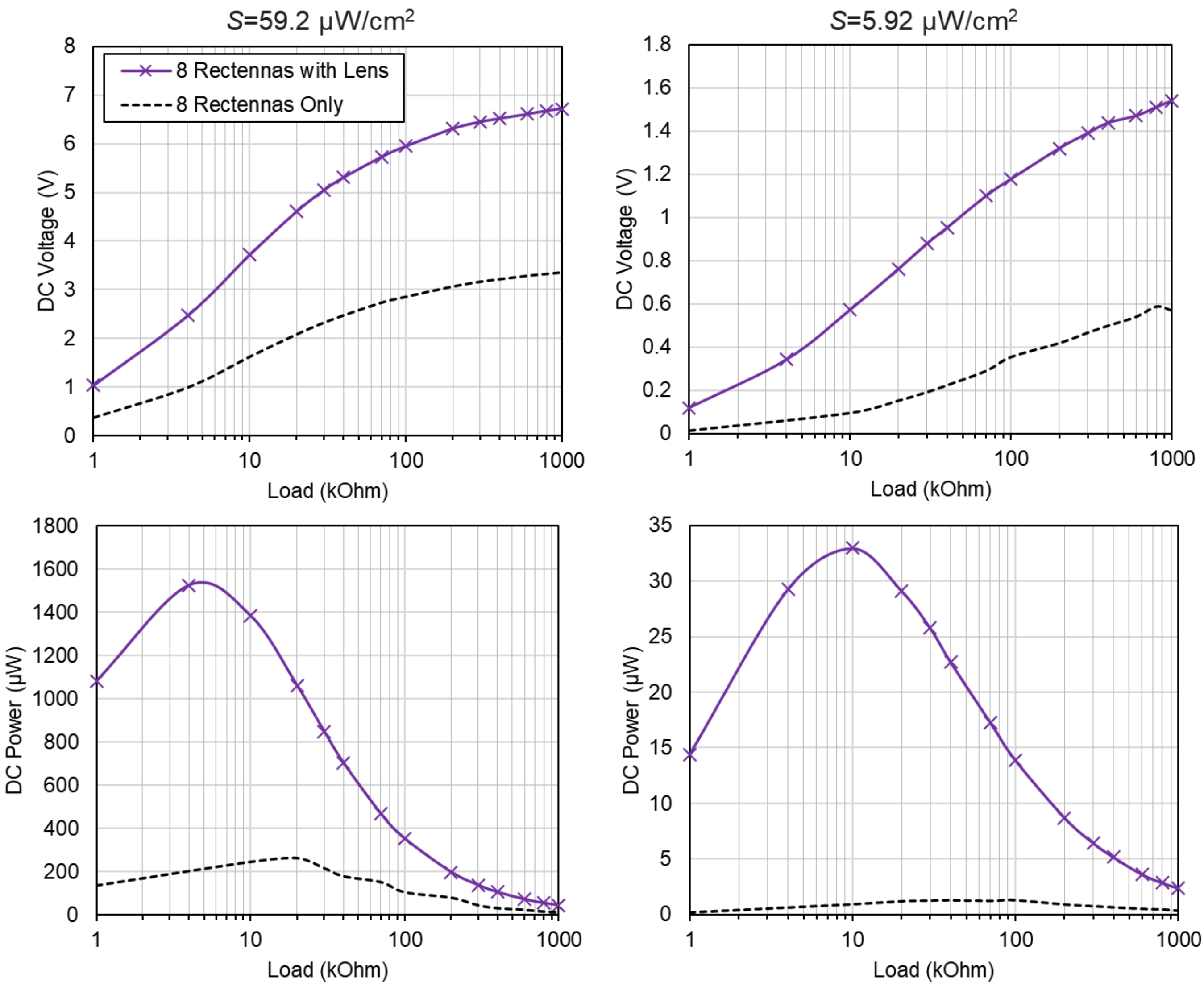

Supplementary Figure 22. The DC output as a function of the load, showing an improvement in the DC power output with the lens for an array of 8 rectennas connected in series. The rectennas cover the full azimuth range of the lens, and are not arranged to maximise the power output from the bore-sight transmitter.

The net DC power output improvement in the 8-rectenna power-combining array is shown in Supplementary Figure 23. It can be seen that the most improvement is observed for high power loads, due to the sensitivity enhancement offered by the lens, which is most impactful at very low power densities, due to the non-linearity of the rectifiers.

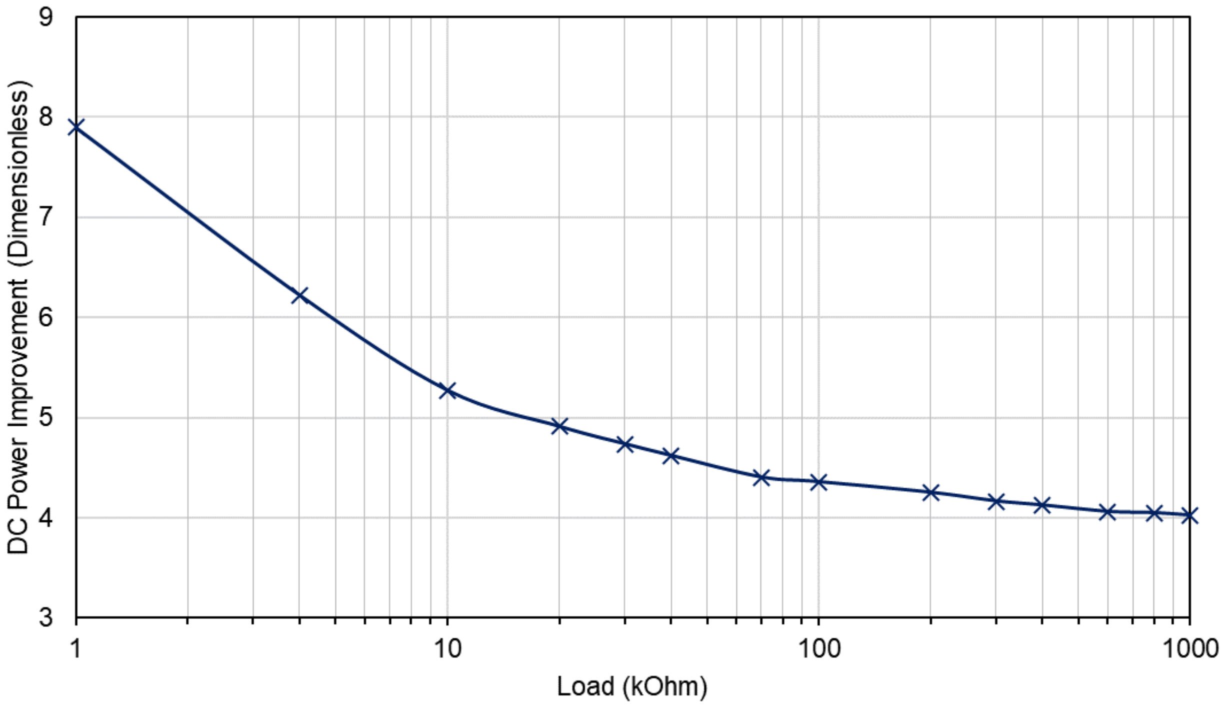

Supplementary Figure 23. The improvement in the DC power output through the addition of the lens to the 8-element array.

Supplementary Note 9. Numerical Electromagnetic Modelling, Power Combining and Channel Variations

A MATLAB-implemented numerical framework characterizes the proposed joint wireless power transfer and edge smart sensing system by integrating analytical line of sight (LoS) propagation with a Method of Moments (MoM) electromagnetic solver. To ensure computational tractability, this framework employs the MoM solver for reflections from predefined environmental features while resolving direct LoS components analytically within a dynamic 3D domain. To replicate real-world confined spaces such as corridors, the model transcends first-order ray tracing to incorporate high-order multipath propagation, thereby capturing the waveguide-like energy trapping between parallel walls. This configuration explicitly positions the transmitter and a multi-element receiver array at discrete coordinates, utilizing real antenna patterns to model spatial selectivity and energy harvesting potential. The framework replaces symmetric 1D pattern approximations by orthogonally decomposing measured data into distinct E-plane (elevation) and H-plane (azimuth) components. This physical reconstruction of a 3D elliptical beam preserves the broader lateral illumination essential for side-wall reflections.

Robustness is evaluated across five distinct simulation scenarios: 1. Radial displacement: Displacing the RX array in four orthogonal directions (upward, downward, leftward, and rightward) to emulate alignment jitter. 2. Reflector distance variation: Adjusting the lateral offset of symmetric reflectors to determine sensitivity to environment proximity. 3. Reflector setup variation: A parameter sweep across geometry, yaw angles, and material coefficients to quantify robustness under realistic perturbations. 4. Vertical variation: Sweeping the TX and RX baseline height to capture elevation effects. 5. Distance sweep for verification: Benchmarking simulation results against experimental measurements to validate framework fidelity.

To resolve RX signals, a simplified MoM formulation based on an impedance matrix Z accounts for mutual coupling among the six array elements. The total incident field is determined by coherently superposing complex contributions from direct and high-order reflected paths, weighted by the reconstructed 3D radiation patterns. Rather than utilizing static empirical constants, the ray-tracing engine applies polarization-dependent Fresnel reflection coefficients (TE/TM waves) to dynamically evaluate the complex permittivity and conductivity of building materials. Furthermore, a Rayleigh surface roughness factor mitigates overestimated coherent interference at extended ranges by modeling diffuse scattering loss. This phase-sensitive approach is critical for calculating the open-circuit voltages V_{oc} and solving the network equation $(Z+Z_L)I=V_{oc}$, ensuring precision in both sensing and power combining.

The framework subsequently transitions from the RF domain to the DC output domain by deriving the input power Pin from current amplitudes and load impedance. A compact rectifier model, implemented via lookup table interpolation with thresholding for dead-zone behaviors at ultra-low power levels, captures the nonlinear RF-to-DC conversion to determine the output voltage Vout. Finally, statistical analysis of individual and aggregated array performance yields cumulative distribution functions that quantify system reliability under spatial perturbations.

Simulation results for single-element and combined rectenna configurations across varying distances are characterized in Supplementary Figure 24. While individual elements show significant performance dispersion, the combined output exhibits a stable, consistently higher power level. This performance is characterized by a path loss exponent of 1.83 (R^2=0.9598), indicating that the simulation environment scales according to near-free-space and waveguide-enhanced propagation. Consequently, these data confirm that spatial combining provides robust harvesting gains and enhanced reliability compared to single-element systems.

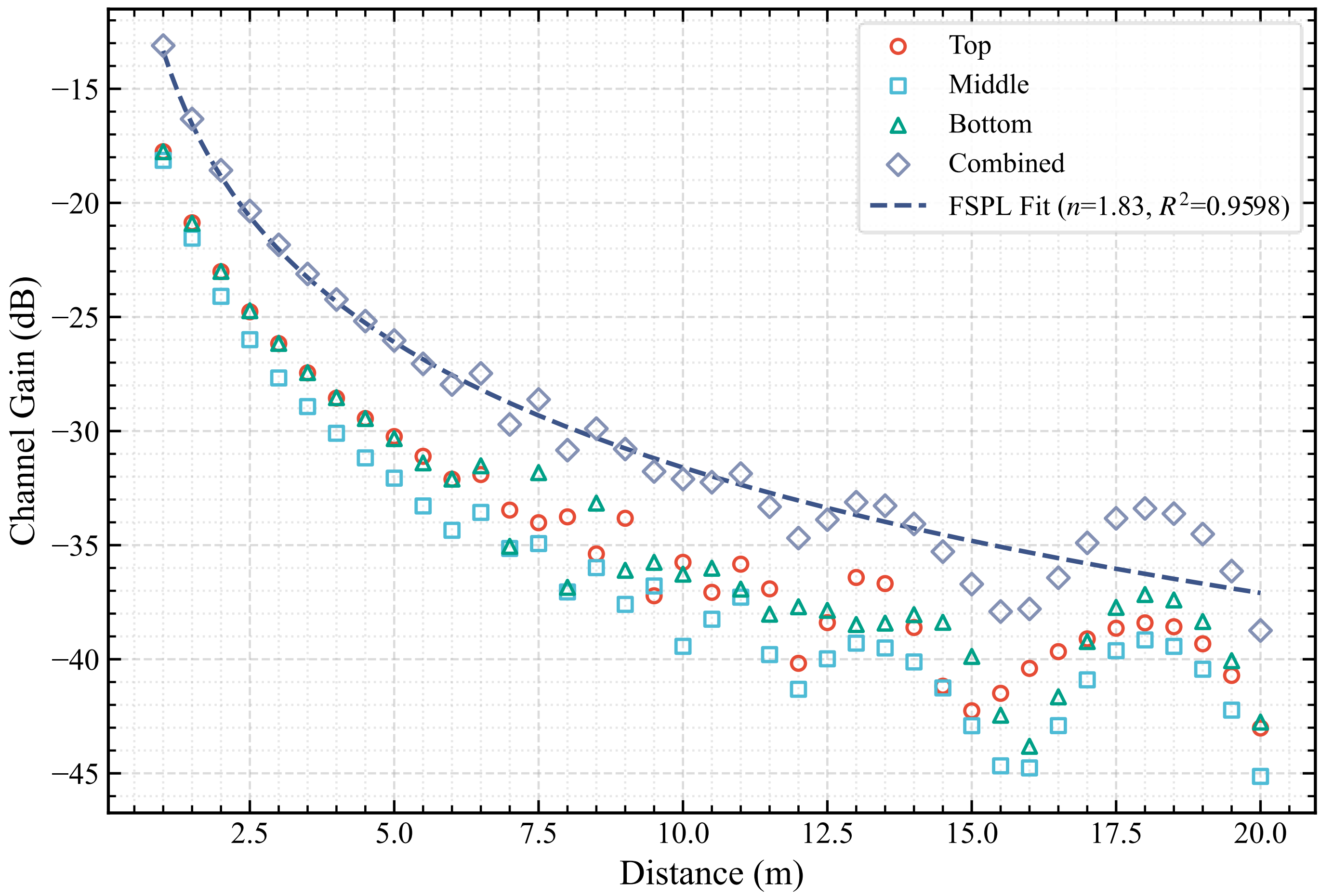

Supplementary Figure 24. the MoM EM-simulated relationship between the relative received DC power level and the distance. The outputs are shown for 3 antennas on three different layers. A similar trend can be seen later in Supplementary Figure 39.

To evaluate the influence of reflections on system performance, we performed a controlled simulation in which two long reflectors were placed symmetrically on both sides of the line-of-sight path between the transmitter and receiver. The two reflectors were moved outward together to quantify their impact on the single-element output voltage and the combined output voltage. Simulations were conducted at three representative link distances of 5 m, 10 m, and 15 m. The lateral offset of the reflectors from the line-of-sight centre “d_Reflector” was swept from 1 m to 10 m as shown in **Supplementary Figure** 25, and the results are reported in **Supplementary Figure** 26.

As the reflectors are displaced away from the centre, the output voltage converges and remains relatively stable beyond a certain offset distance. This behaviour indicates that the system performance does not depend on nearby reflectors or a highly reflective environment, and that reliable operation can be maintained under reflection-suppressed conditions.

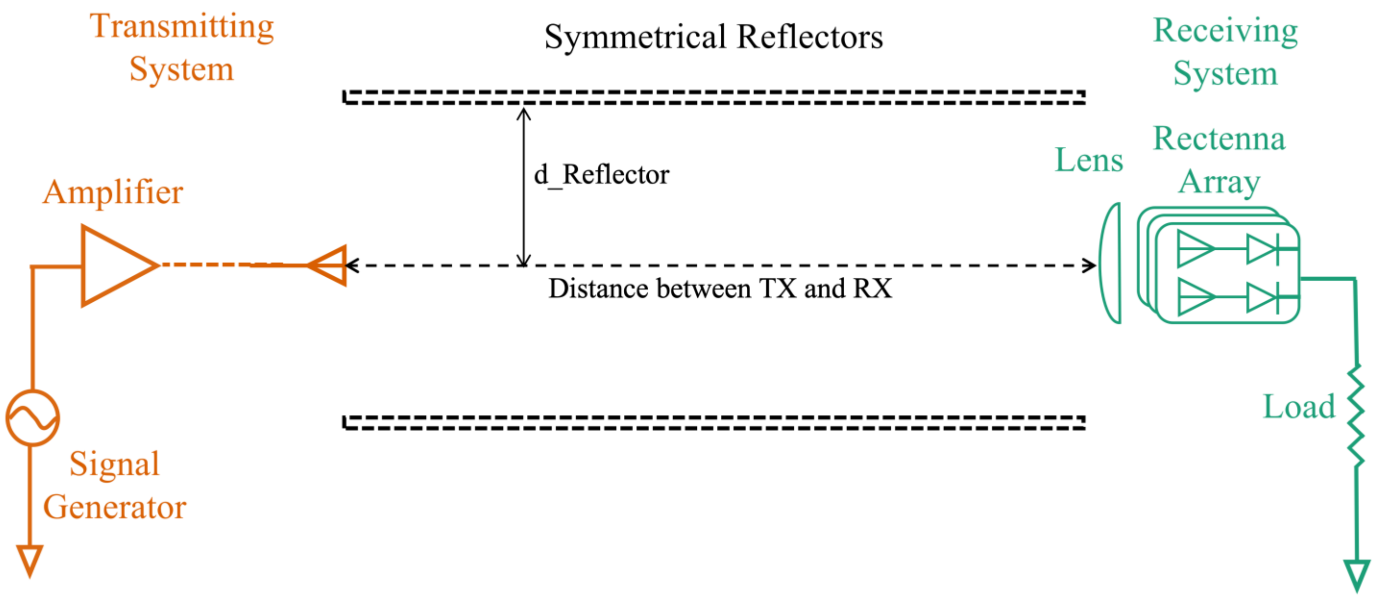

Supplementary Figure 25. The numerical simulation setup of the d_Reflector change.

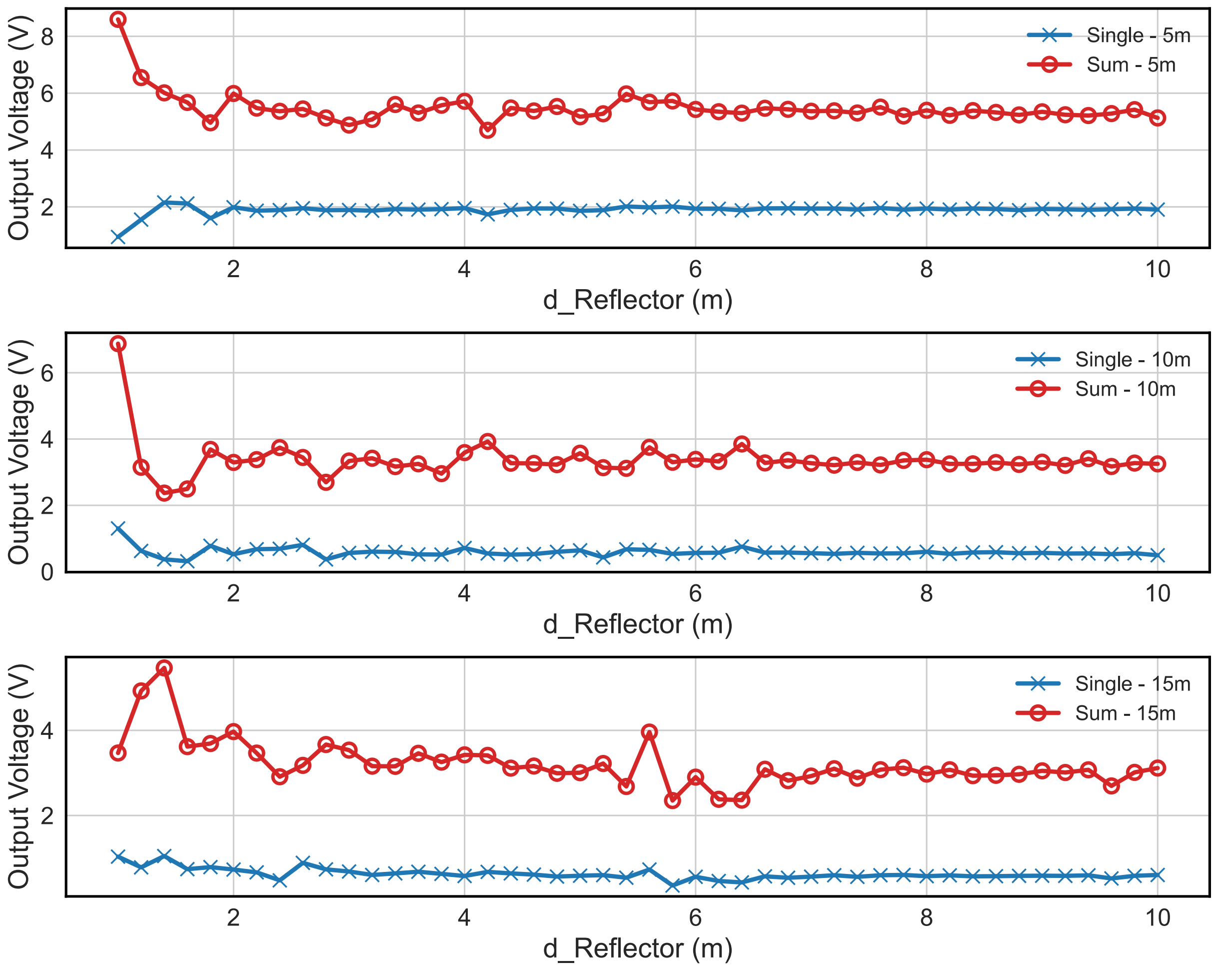

Supplementary Figure 26. The simulated output voltage with the reflector spacing "d_Reflector" change at three fixed different distances between the transmitter and the receiver.

Another simulation investigates reflector configuration variation, and the corresponding confidence index is computed accordingly. The reflector arrangement adopts a dual plate geometry, in which two identical plates are positioned symmetrically with respect to the central boresight axis connecting the transmitter and the receiver. To evaluate geometric scaling effects, the reflector length is swept from 0.5 m to 4.0 m, while the reflector height is varied from 0.5 m to 3.0 m. To quantify the sensitivity of energy enhancement to spatial placement, the lateral offset of each reflector from the boresight axis, defined as the half gap, is incremented from 0.5 m to 4.0 m. In addition, the reflector yaw angle about the vertical axis is swept from -75 degrees to +75 degrees to characterize reflector induced beam steering efficacy under different angular orientations.

To incorporate realistic material dependent behaviour, the simulation models representative building surfaces using reflection coefficients of 0.98, 0.80, 0.55, and 0.35, corresponding to metallic panels, reinforced concrete, masonry brickwork, and timber structures, respectively. The environment is further augmented with a variable number of random scatterers, ranging from 0 to 50, to emulate multipath components and clutter typically observed in dense indoor scenarios. A separate case with all similar variation setups, but only one side reflector placed, was also simulated to cover the situations where only asymmetrical reflectors were placed. All reflector variation experiments are conducted at three TX to RX separations, namely 5 m, 10 m, and 15 m. The confidence index is reported for both the single rectifier output and the aggregated output of the rectifier array, as shown in the results. As shown in **Supplementary Figure** 27 - 29, the confidence index with both original data and the data normalized by the mean value in three cases were presented to provide a clear outlook of the results with reflector setup changing.

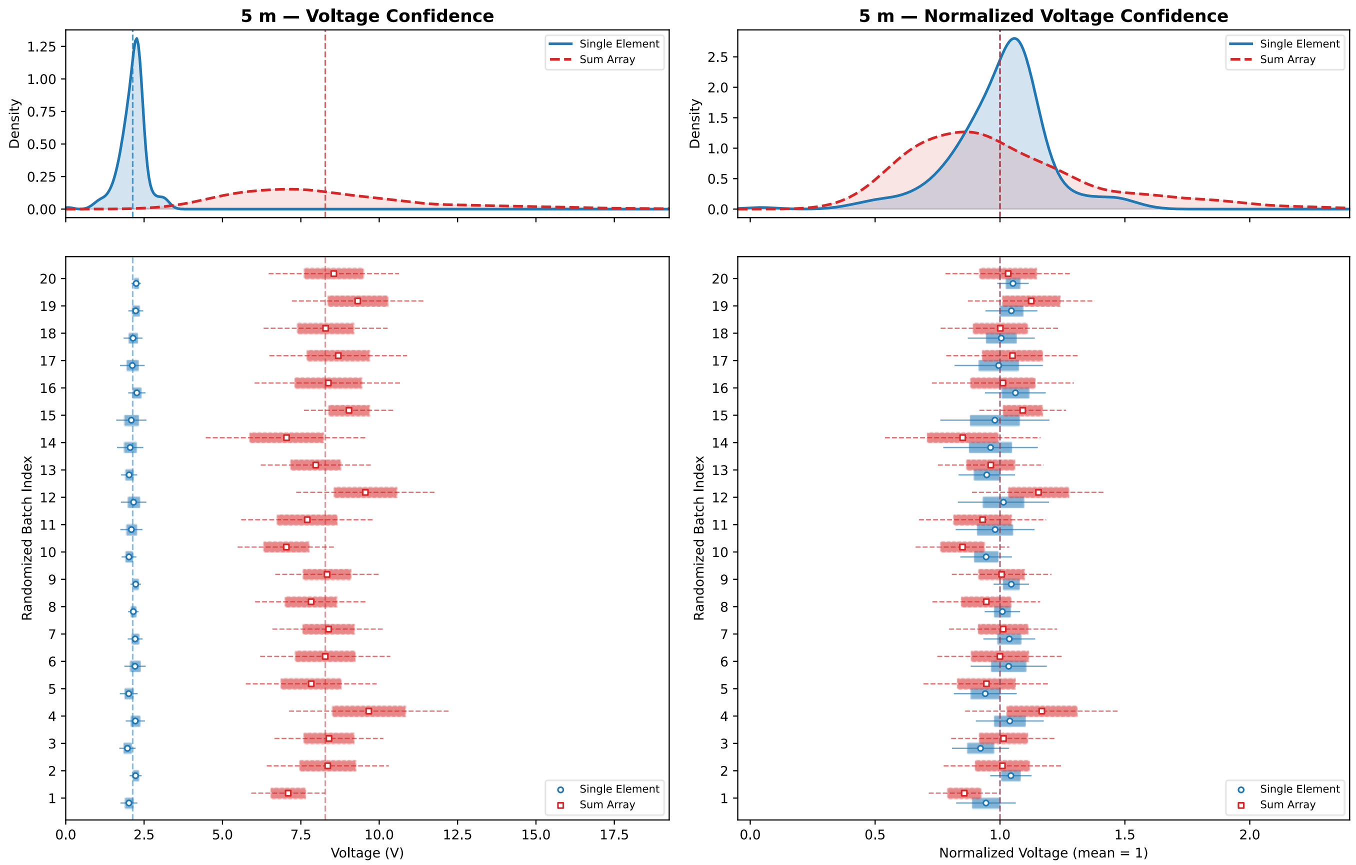

Supplementary Figure 27. Confidence index of the output voltage for the single rectifier element and the aggregated array output under reflector configuration variations at a TX to RX separation of 5 m.

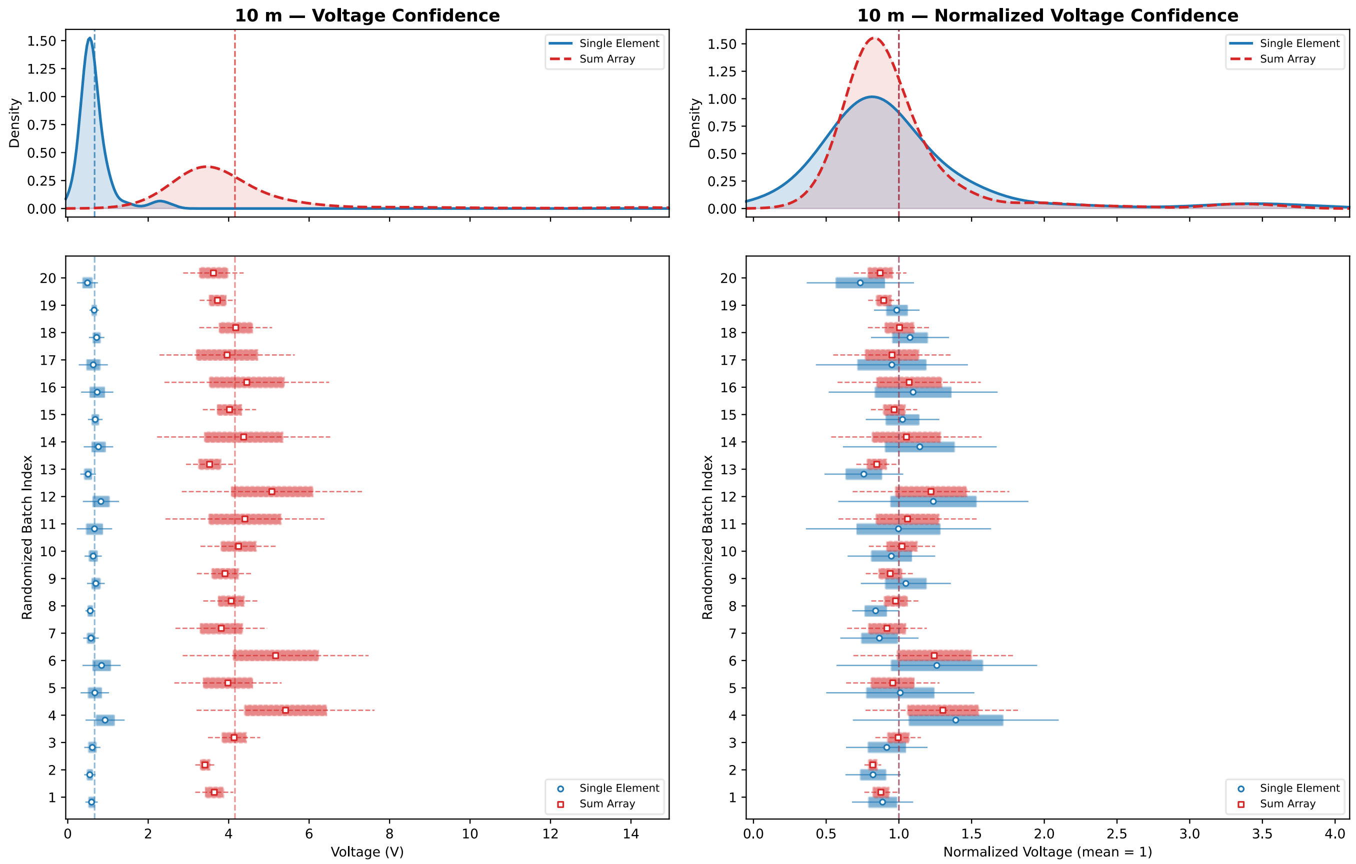

Supplementary Figure 28. Confidence index of the output voltage for the single rectifier element and the aggregated array output under reflector configuration variations at a TX to RX separation of 10 m.

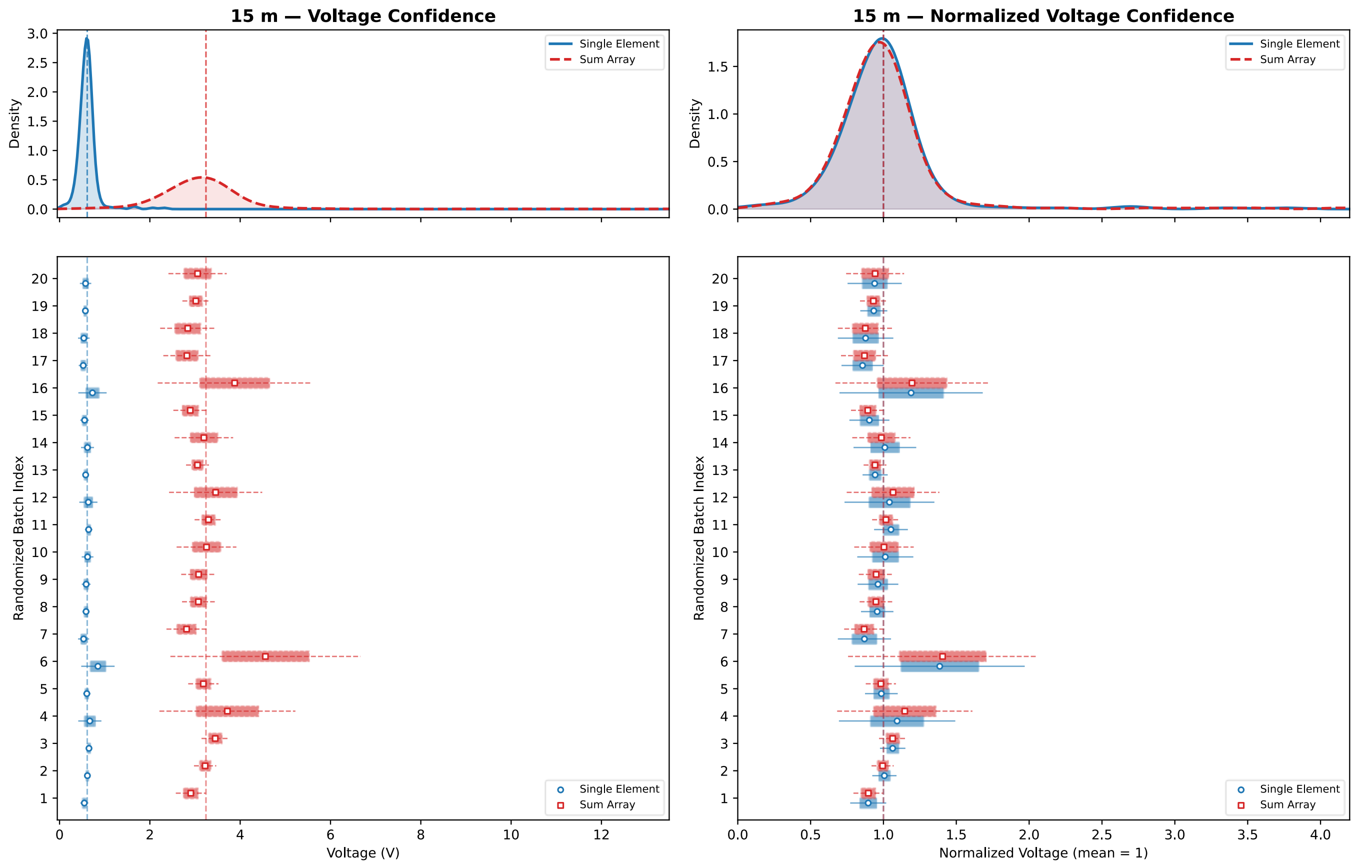

Supplementary Figure 29. Confidence index of the output voltage for the single rectifier element and the aggregated array output under reflector configuration variations at a TX to RX separation of 15 m.

To further evaluate performance without relying on reflections, we conducted simulations at three fixed transmitter–receiver distances of 4 m, 8 m, and 12 m under a reflection-free baseline condition. We then carried out two parametric studies to assess the robustness of the combining gain under geometric perturbations.

First, a height sweep was performed by varying the transmitter and receiver heights from 0 m to 2 m, as shown in **Supplementary Figure** 30. Second, we performed a combined receiver moving and height sweep study, in which the receivers were moved in horizontal and vertical axes for several steps with a 5 cm step length. For reference, the measured results at the corresponding distances are also included to enable a direct comparison between simulation and measurement as shown in **Supplementary Figure** 31.

Across both studies, the combined output consistently remains higher than the single-element output, indicating that the combining benefit persists under height changes and reflector parameter variations. Moreover, the simulated trends are in good agreement with the measurements (detailed in the next Supplementary Note). The measurements exhibit a higher standard deviation due to the more multipath-rich environment compared to a limited number of reflectors.

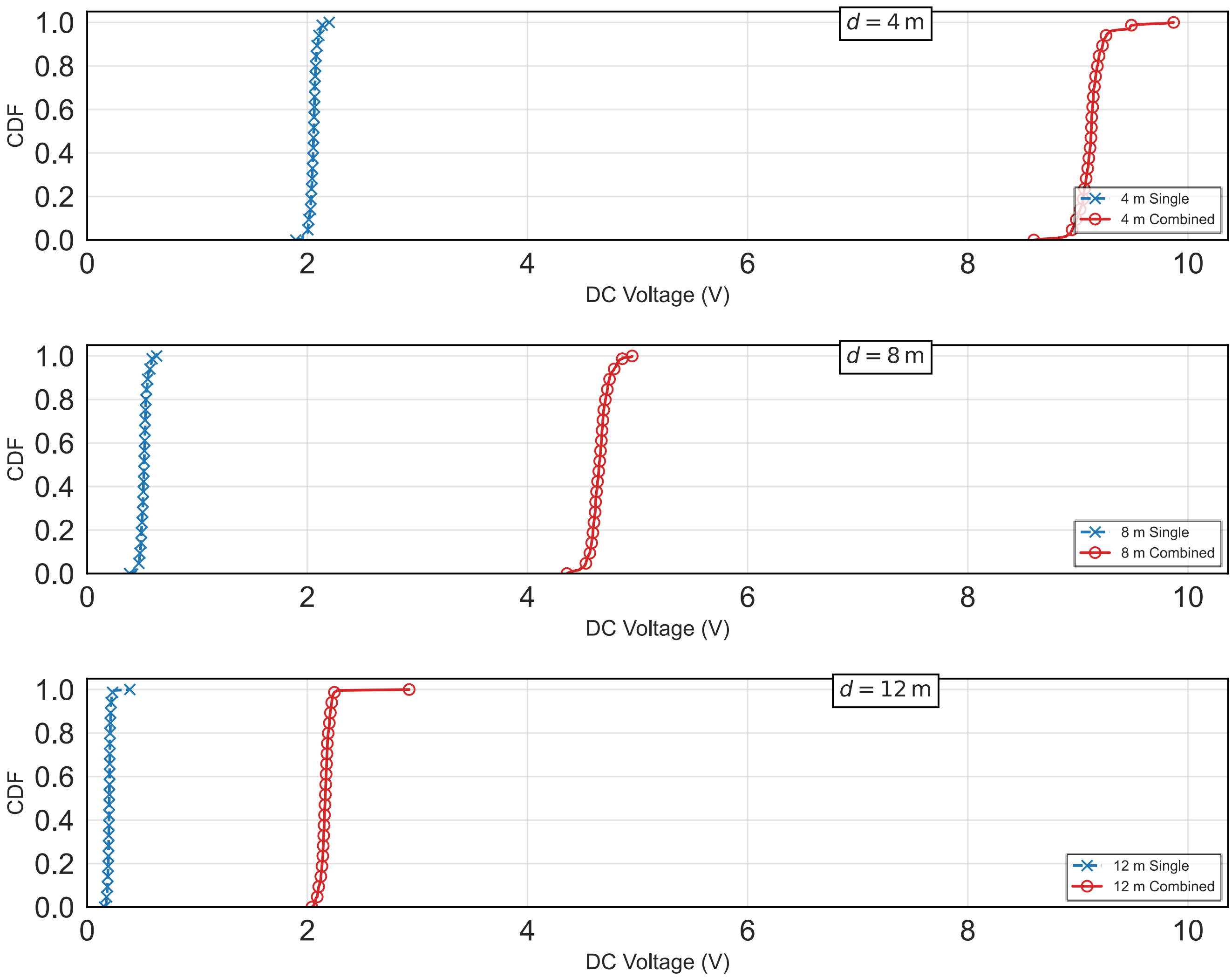

Supplementary Figure 30. CDF of the received output voltage, at three representative distances, with height changes.

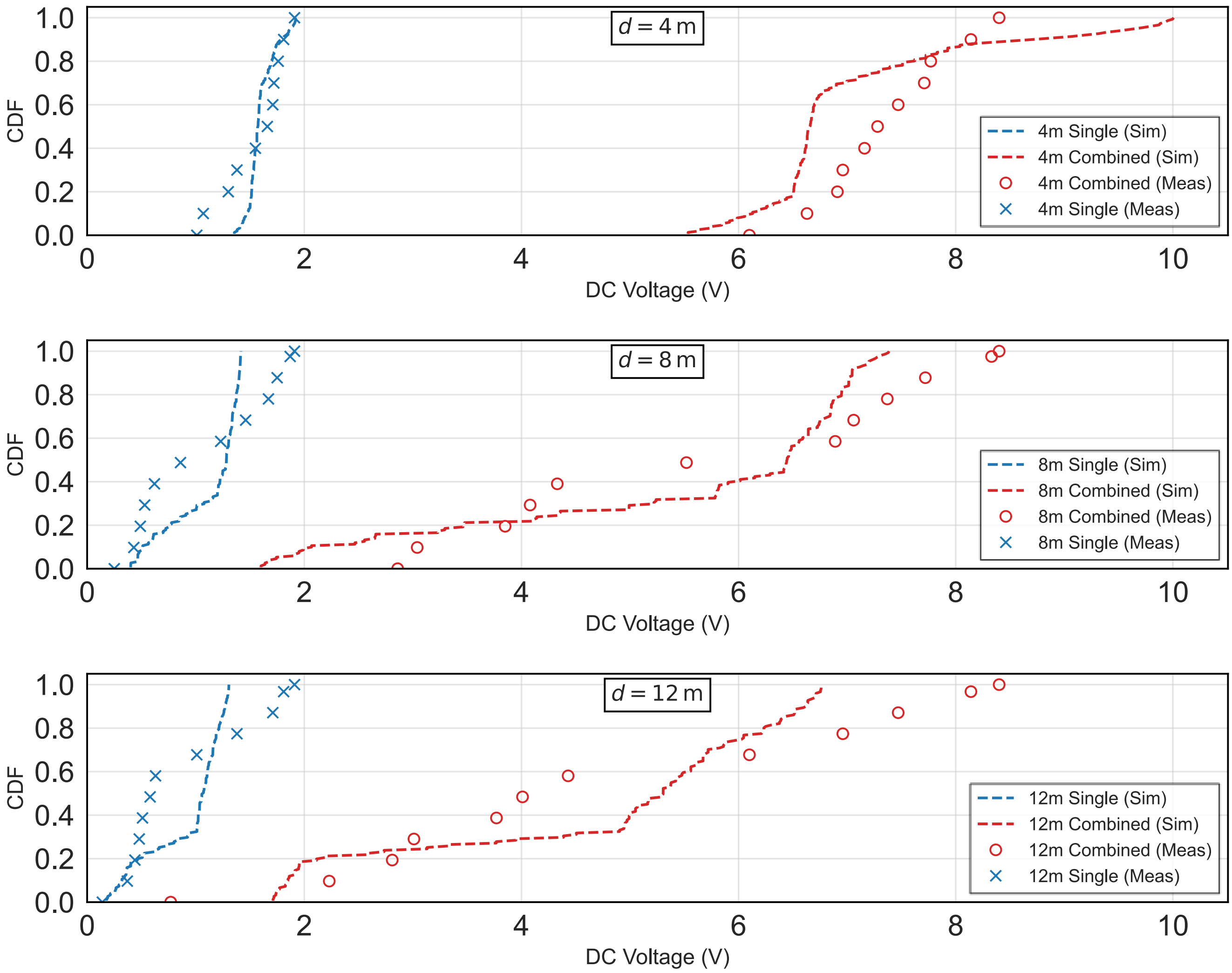

Supplementary Figure 31. CDF of the received output voltage, at three representative distances, with receiver moving and height changes (simulation and measurement).

To further validate the fidelity of the simulation framework, we present a direct comparison between the simulated and measured results. **Supplementary Figure** 32 shows the DC output voltage as a function of the transmitter–receiver distance. Over the range from 1 m to 12 m, the simulation agrees well with the measurements for both the single-element and the combined output voltages, indicating that the proposed model captures the dominant distance-dependent behaviour of the system.

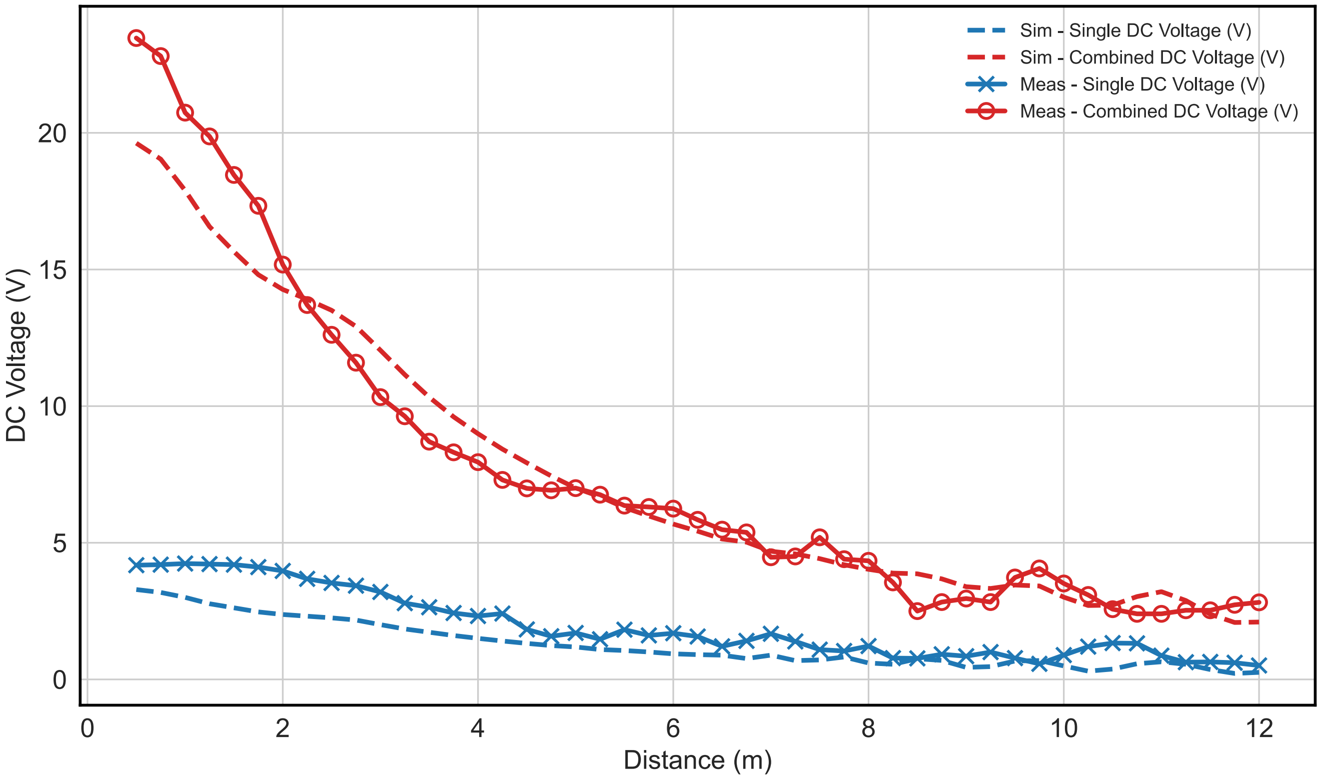

Supplementary Figure 32. Relationship between DC voltage and distance between TX and RX (simulation and measurement).

Supplementary Note 9. Statistical Propagation Measurements for Muli-Rectenna Combining

As discussed in the Methods section, a 4-port VNA measurement was used to investigate the effect of ideal power combining on the channel characteristics. 3 dipole antennas were connected behind the lens, emulating the 3 rectennas with the highest expected power level. The measurement setup is shown in Supplementary Figure 33. Curve fitting was performed using an optimiser in Matlab, to obtain the path-loss exponent *n* with the best fit for the data. In addition, the coefficient of determinism R^2 was also calculated for all three receiving antennas.

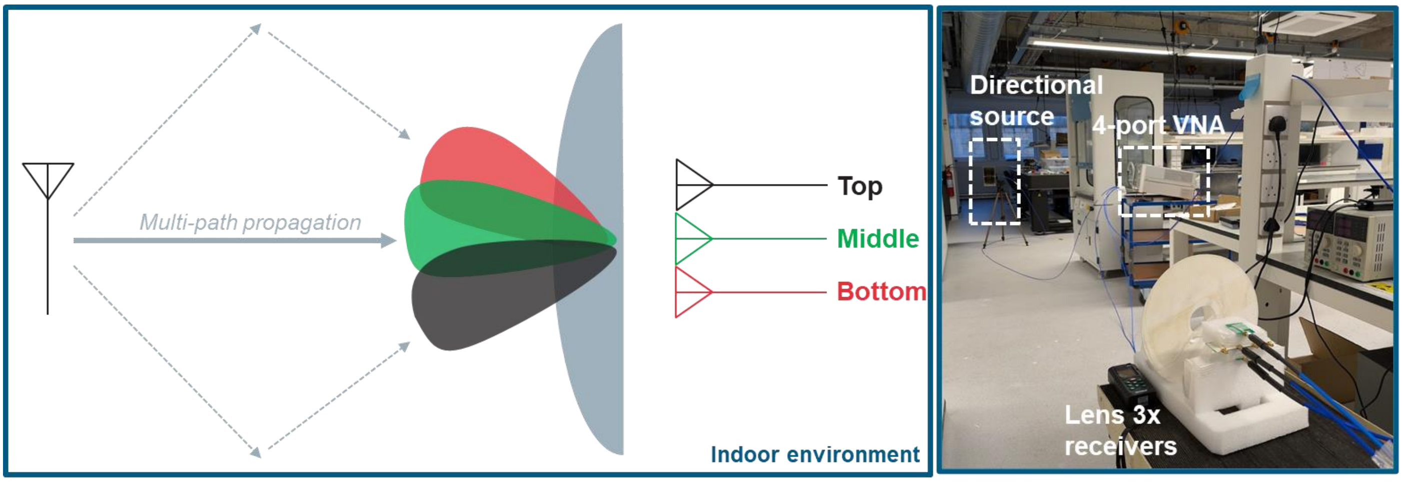

Supplementary Figure 33. Multi-antenna measurement setup using a 4-port VNA, in an indoor environment, for measuring the channel gain across multiple antennas (emulating the rectennas).

The measured channel gain data is shown in **Supplementary Figure 34**, as a function of distance. While the indoor environment does show a lower path loss exponent than 2, due to the reflections from the ceiling/floor, which could be approximated as a near-perfect reflecting boundary, the R2 indicates that the power level received on any individual antenna will not be highly deterministic, due to the destructive interference expected at certain distances, as observed in the measured data.

On the other hand, with ideal power summation, i.e. simulating ideal combining, it can be seen that the channel's determinism improves significantly, with over 5-10 dB improvement in the total received power compared to the individual antennas, in the deep-fading scenarios, e.g. around the 10 m distance point. The improved R^2 and reduced *n* show that the power combining approach, even with only 3 antennas, can introduce a predictable reduction in the path-loss, which enables the quasi-optic WPT system to be used in different environments and at different distances, without experiencing the variations typical in RF WPT systems.

Supplementary Figure 35 shows the measured improvement in the RF power level received through power combining, with a mean improvement around 3 dB (2x), when 3 antennas are feeding the lens. Using the extracted *n* values, the extrapolated received power levels are shown in **Supplementary Figure 35(b)**.

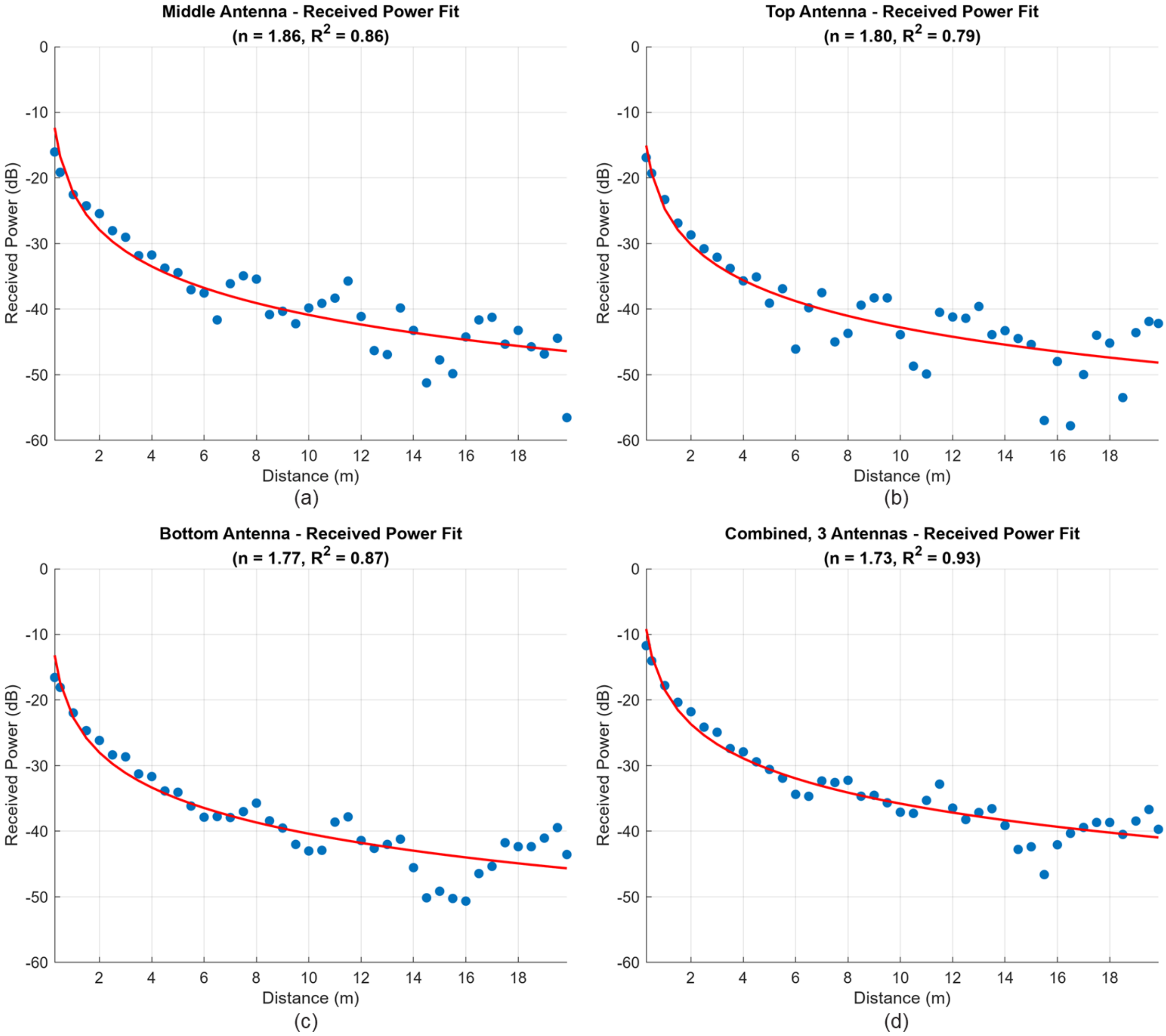

Supplementary Figure 34. The measured channel gain (received power), over distance for the middle (a), top (b), and (c) antennas behind the lens, and the ideal summation of the measured channel gain in (d).

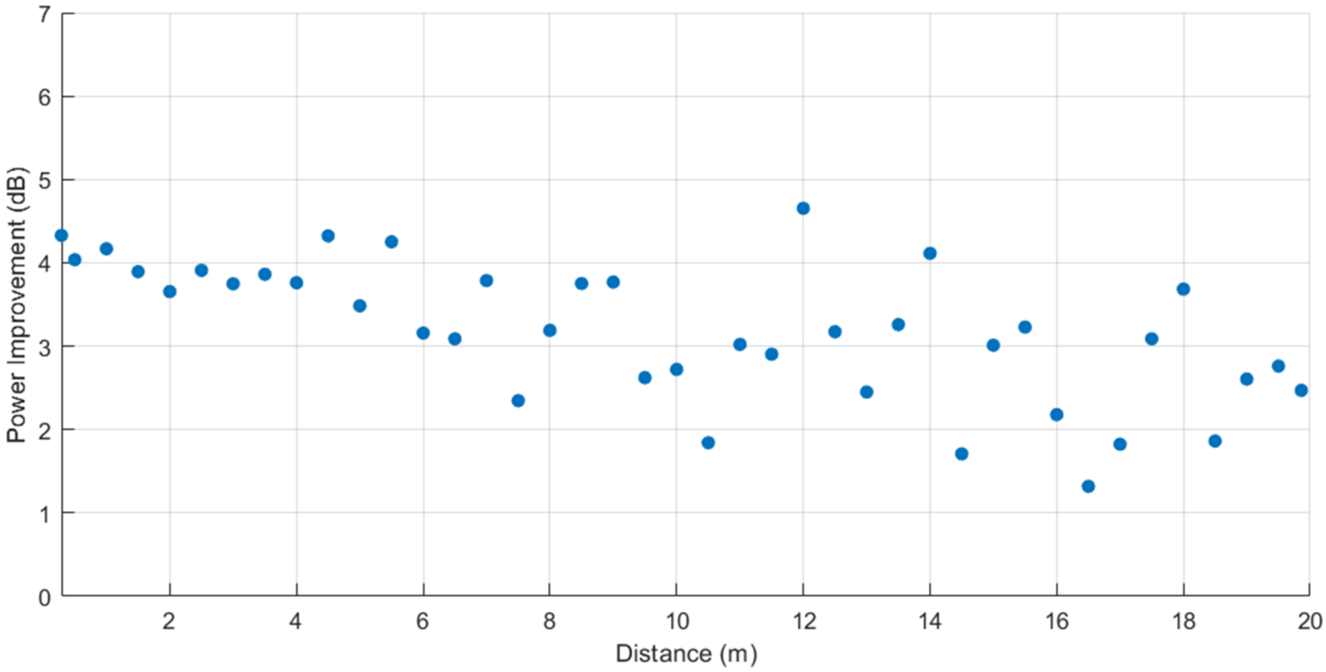

(a)

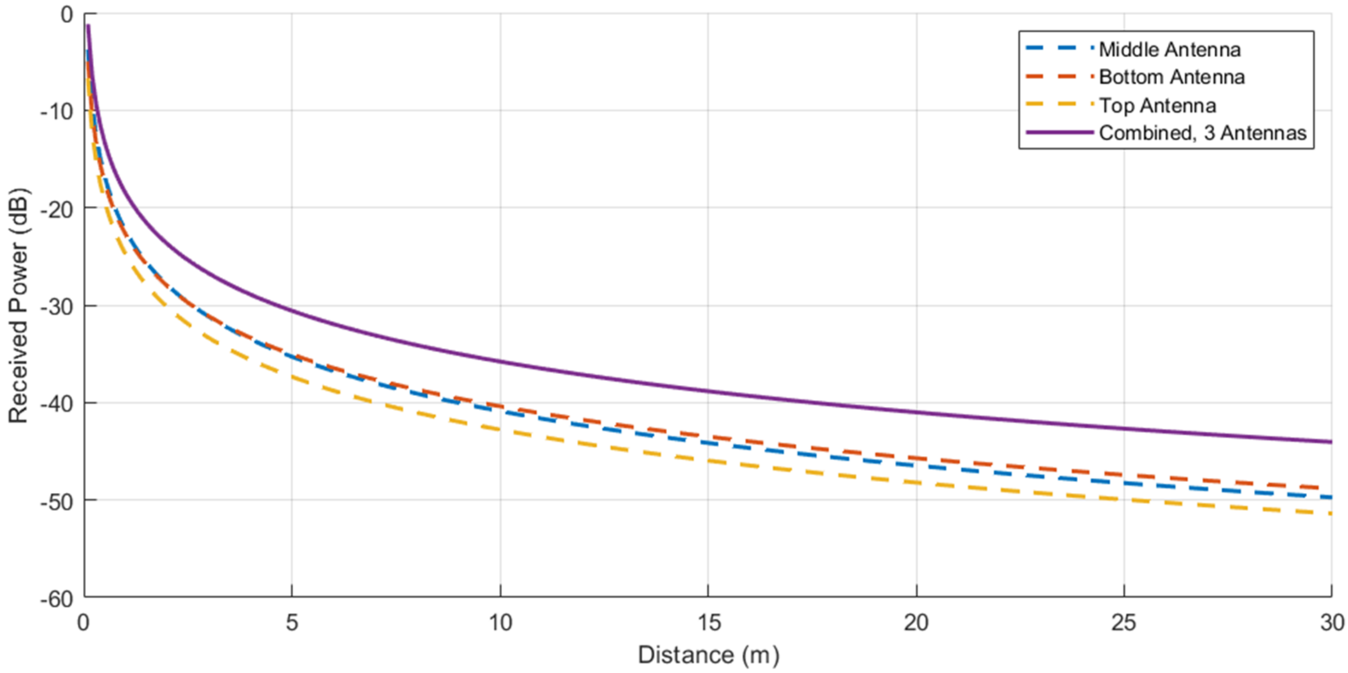

(b)

Supplementary Figure 35. The influence of power combining on the link: (a) measured power improvement; (b) extrapolated path-loss model up to d=30 m.

Note 9.1. CDF of RF Channel Gain:

To demonstrate the repeatability of the improvements with power combining, and also compare that in the presence and the absence of quasi-optic lens-based focusing, statistical measurements were performed at 3 representative distances of 4 m, 8 m, and 12 m. The positioning of the link and the antennas' height was varied randomly (with the height changing in 10 cm steps) to collect 25 data points at each distance.

Supplementary Figure 36 shows the CDF measured RF channel gain at all three distances, in the presence of the lens. Across all distances, the power combining yields at least 3 dB mean improvement in the received power level. It can also be seen that particularly for longer distance, the determinism of the response improves, with a lower standard deviation.

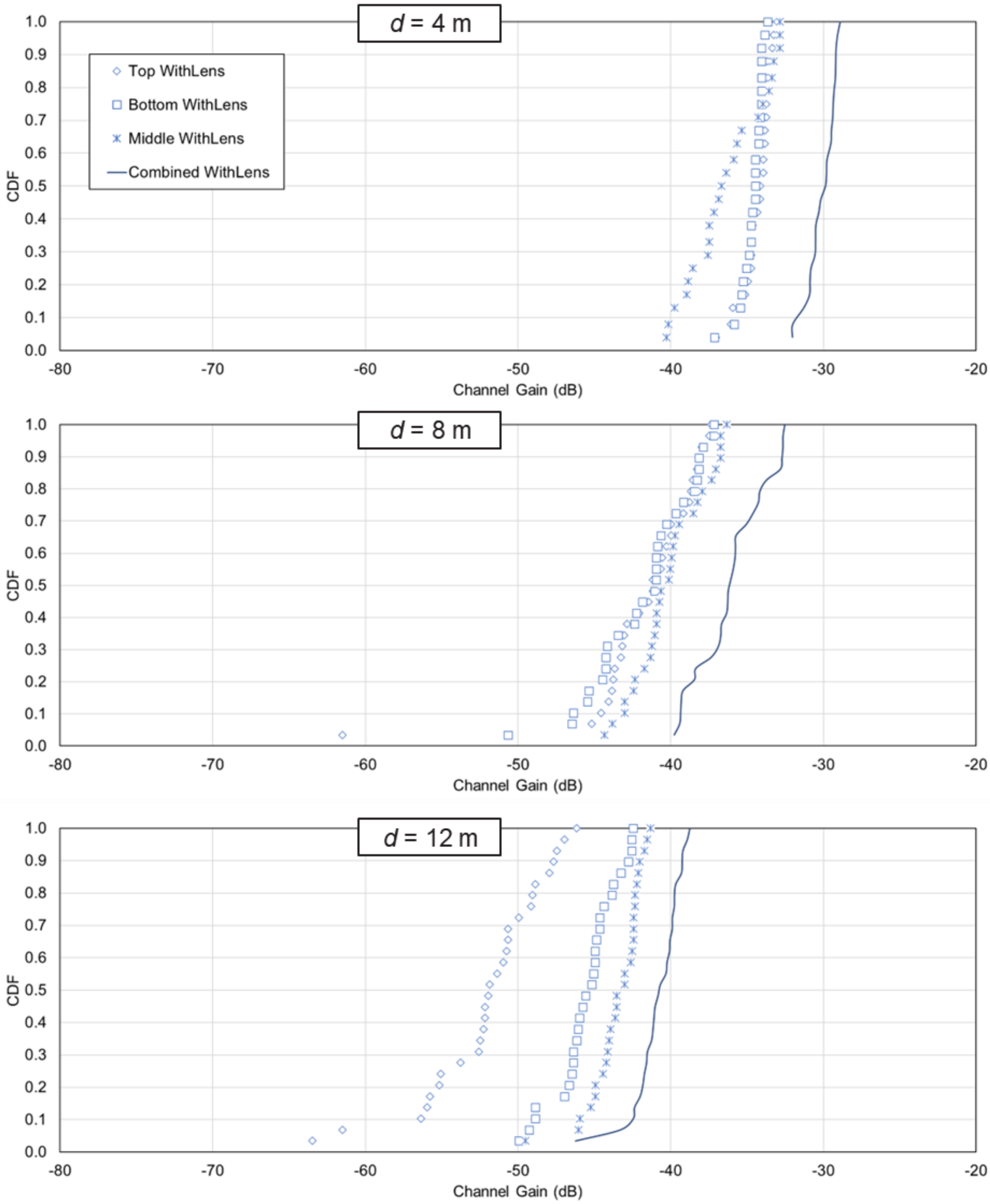

Supplementary Figure 36. CDF of the received power level, at three representative distances, in the presence of the lens.

Supplementary Figure 37 shows the CDF in the absence of the lens, where a similar trend can be observed. A noteworthy trend is seen at d = 8 m, where the antennas experience deep fading due to ground reflections, whose influence is not evident in the lens-based case, due to the higher gain of the antennas and the lower reflections off the ground. From these results, it can be concluded that power combining is highly beneficial in both the presence and absence of quasi-optic beamforming, and that these findings could be applied in other RF WPT scenarios and using other antennas.

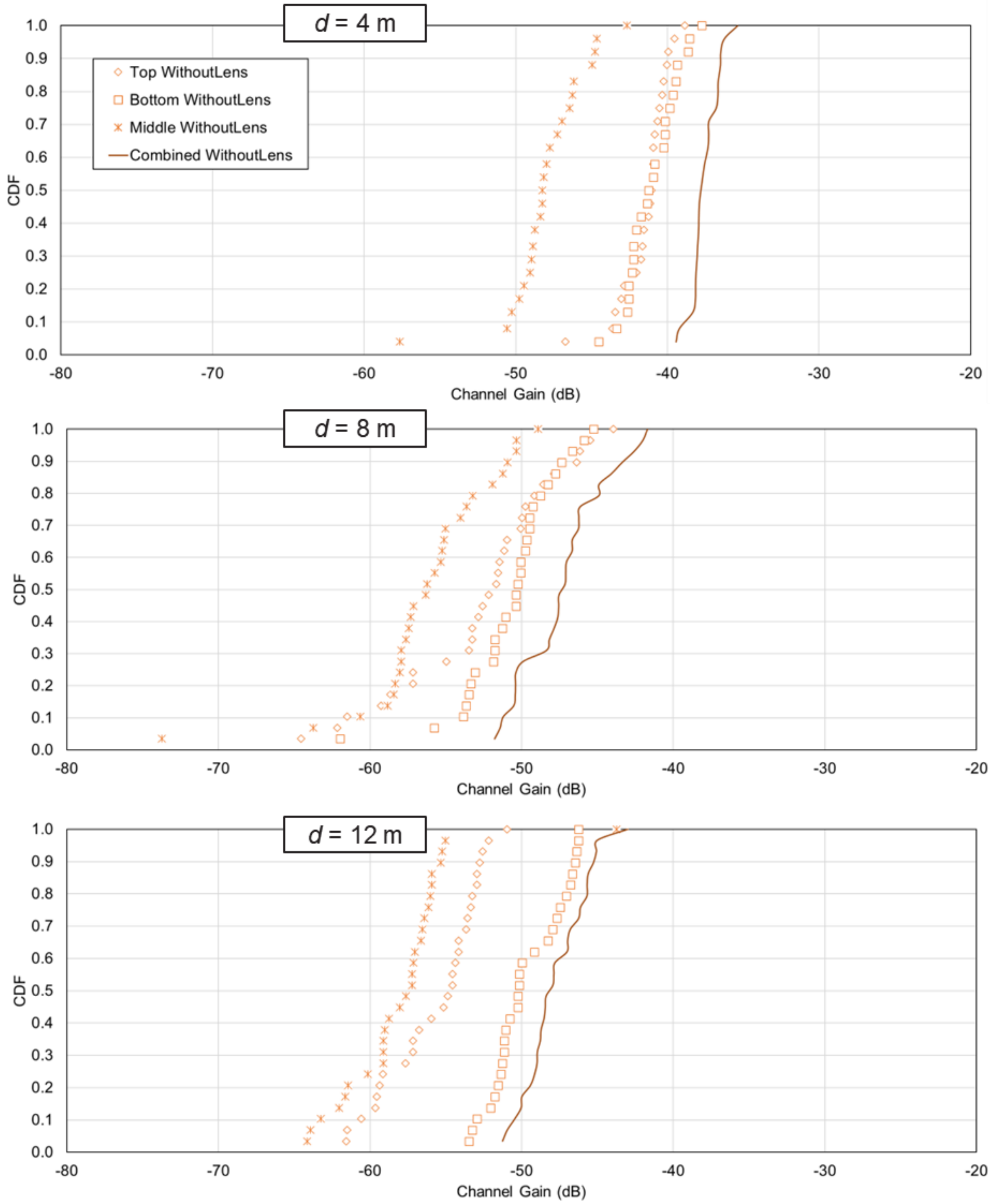

Supplementary Figure 37. CDF of the received power level, at three representative distances, in the absence of the lens (i.e. Yagi antennas only).

Note 9.2. DC Power Combining

A similar study was performed using 6 rectennas behind the lens, and using the RF-DC rectifiers and their DC output to evaluate the channel response. A spectrum analyser was also used, connected to a horn of approximately the same gain as the lens rectennas, to observe the channel's response in the absence of the rectifiers' non-linearity, and also the impact of power combining.

The measurement setup is illustrated in **Supplementary Figure 38(a)**; the rectennas at the centre of the lens were used, as they primarily receive the incident boresight fields, with the multi-path components only arising from ground reflections rather than aiming to capture signals from other transmitters.

The power combining was investigated twice:

1. **Ideal power combining/summation:** the measured DC power output on each rectenna was summed, numerically, to estimate the maximum achievable gain. This setup is similar to the RF approach described in the previous section, and assumes loss-less summation.
2. **Practical series voltage summation:** the output of the rectennas was connected directly in series, to measure the total DC voltage output, inclusive of the additional forward voltage drop over the diodes and also any power imbalances.

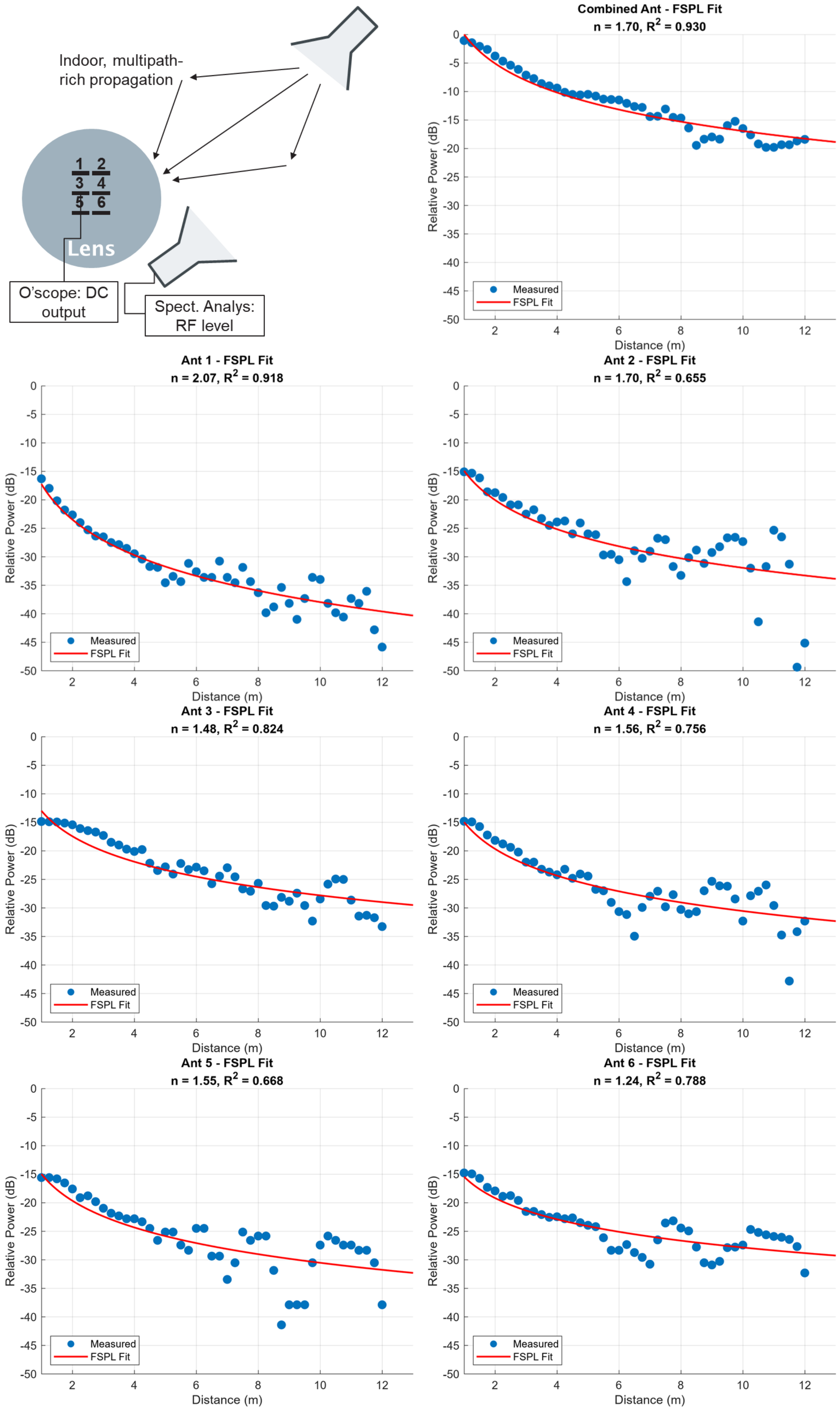

Supplementary Figure 38. DC-based measurements of the propagation, showing the effect of power combining, physically (through series connections), on the path-loss exponent *n* and the channel's determinism (R^2).

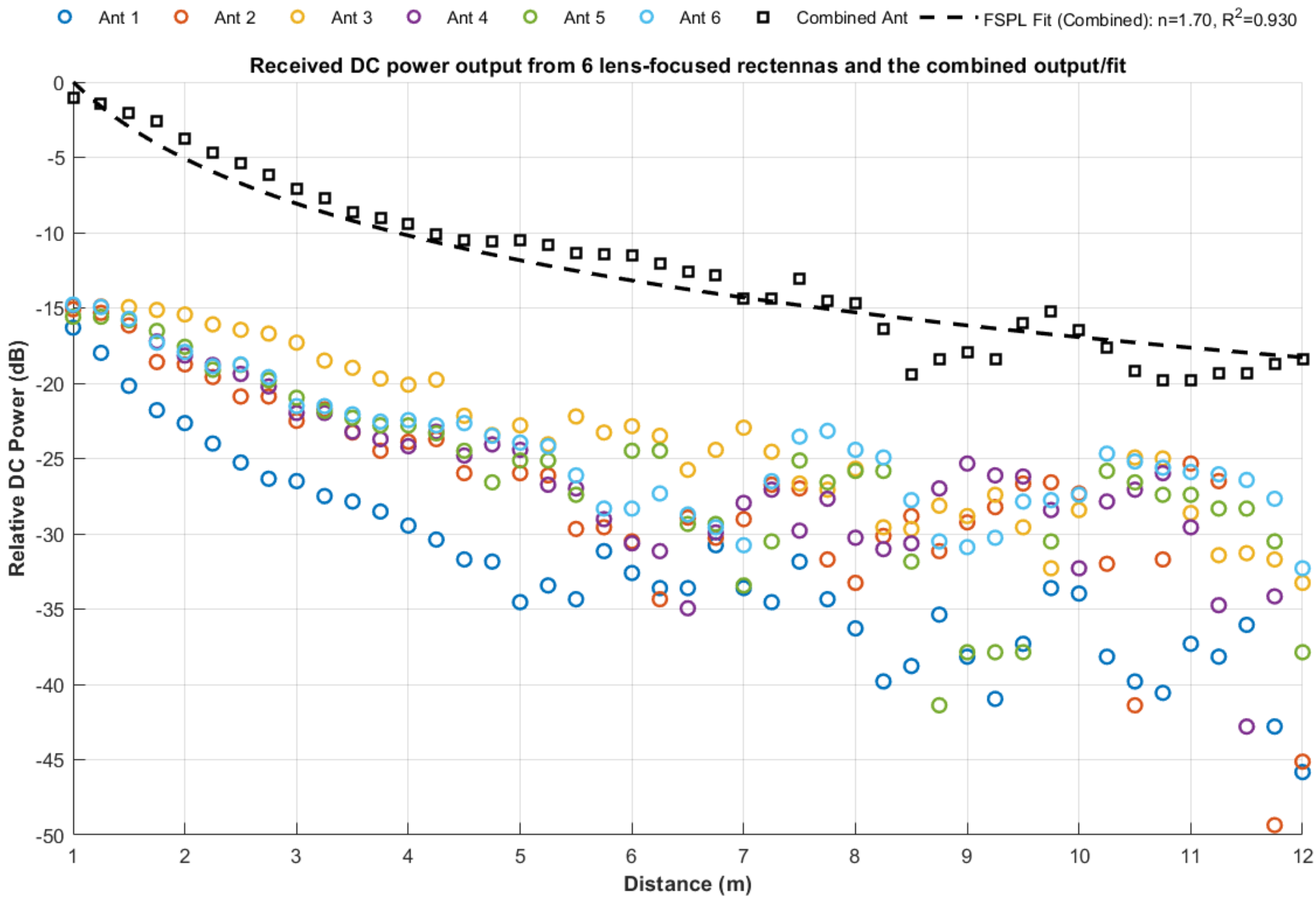

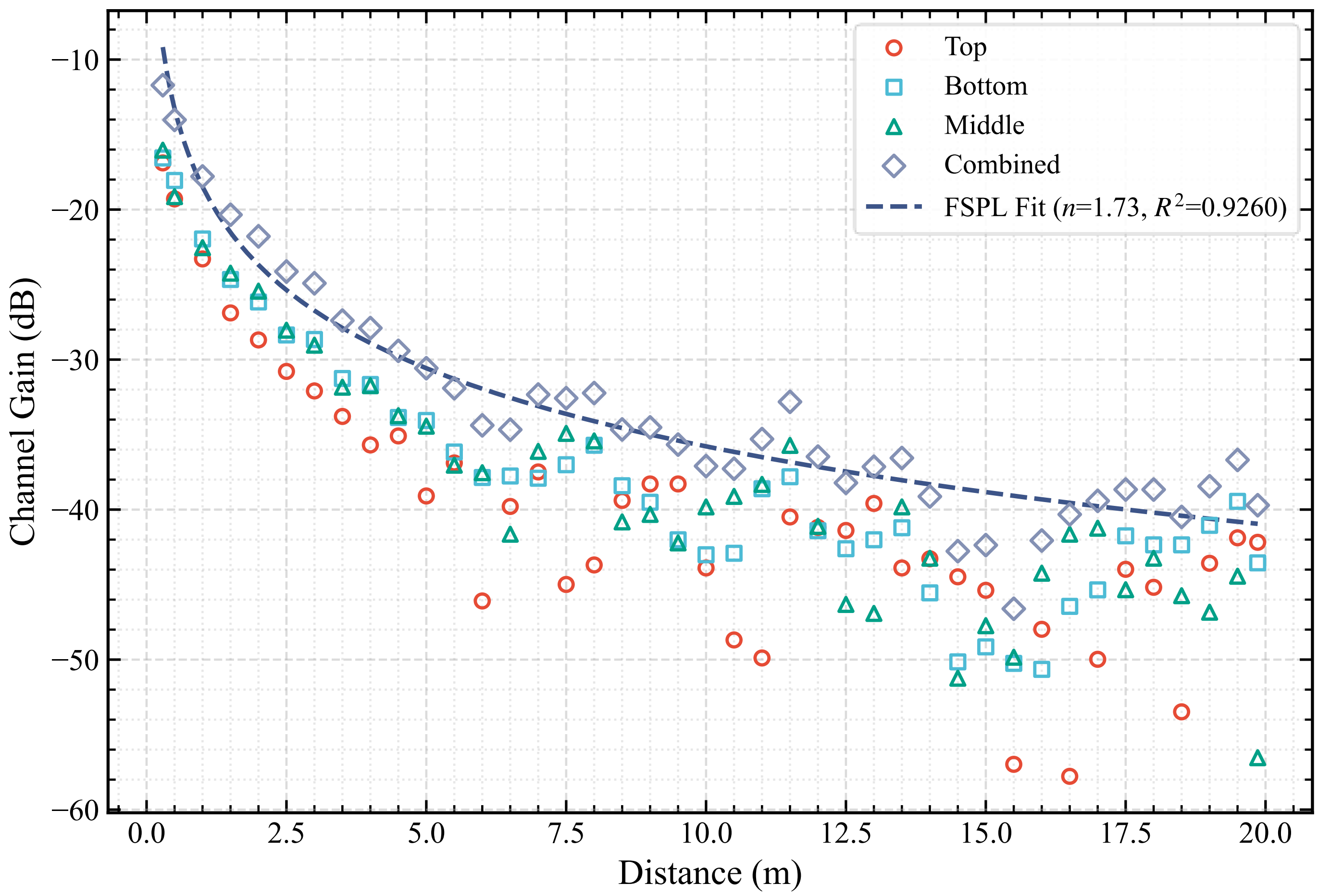

Supplementary Figure 39. Measured, combined DC power output over distance in the setup from Supp. Fig. 29.

To explore the statistical variations in the DC voltage levels, 20 measurements were taken at each distance point of 4 m, 8 m, and 12 m, from the transmitter. The height of the transmitter was changed in between measurements in approximately 5 cm increments (i.e. smaller than the wavelength). The CDF of the measured DC output are shown in Supplementary Figure 40.

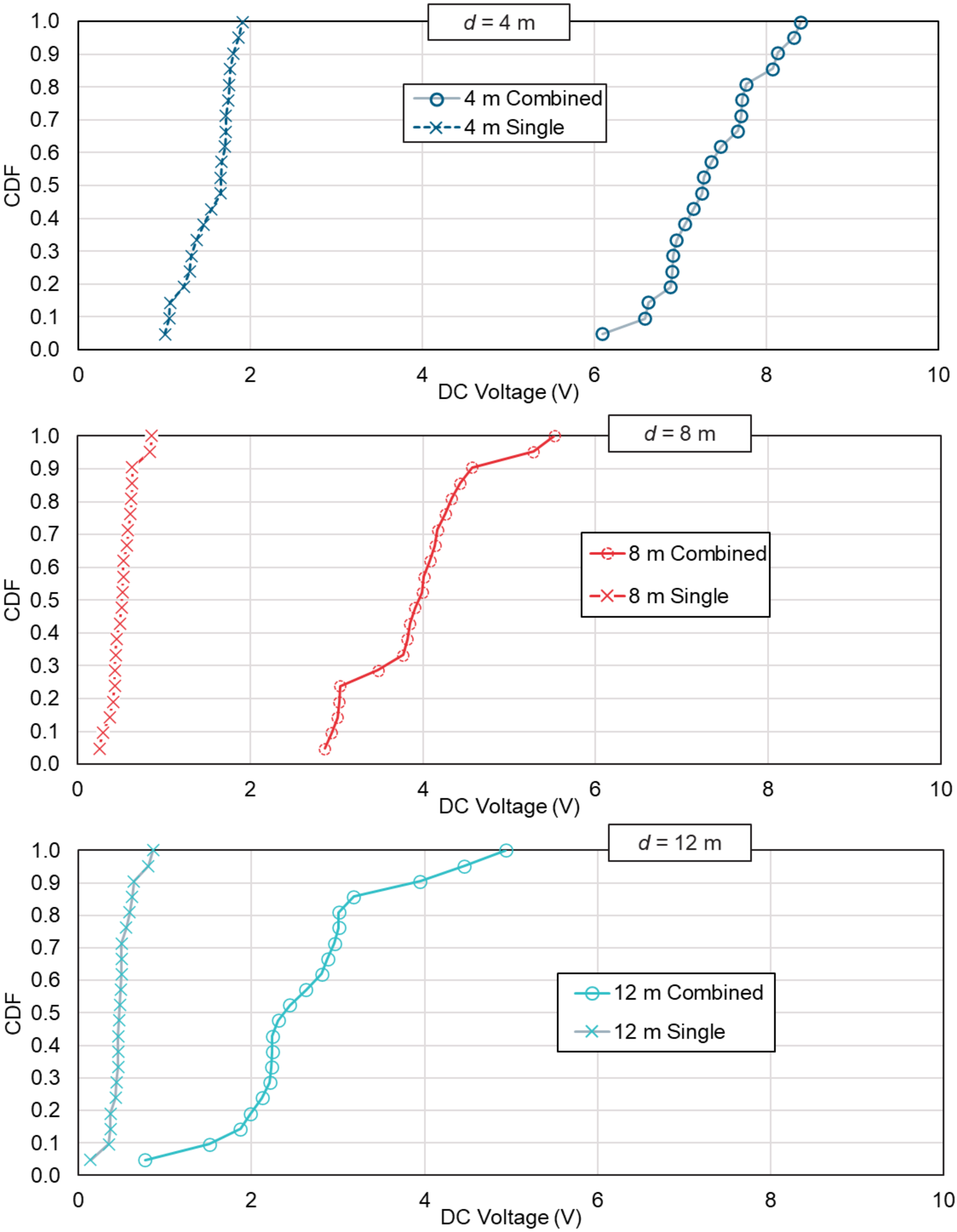

Supplementary Figure 40. Measured CDF of the DC voltage output. The mean figures are presented in the main paper in Figure 4(e),

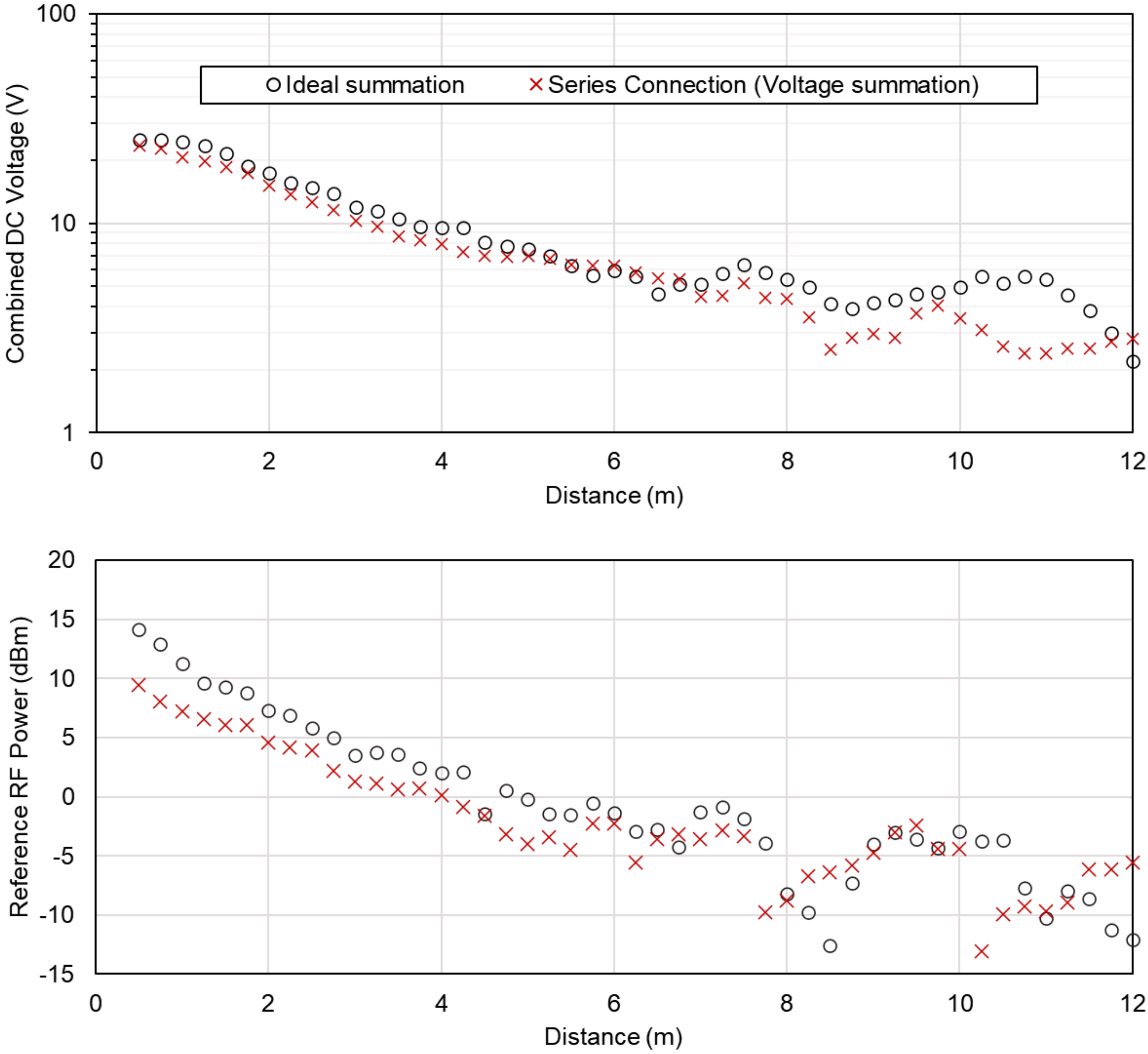

Supplementary Figure 41. The combined DC voltage output, assuming ideal summation of all individual rectenna channels, and actual data, measured after connecting all six rectennas in series. The RF power level on the spectrum analyser is shown as a reference, to demonstrate that the experimental setup remains unchanged.

Path-Loss Exponent Statistical Analysis Against Misalignment in Different Test Environments

To verify the system performance in a spacious environment and to reduce the influence of strong indoor reflections, we conducted additional experiments in two representative settings: (i) a full anechoic chamber and (ii) a large classroom. The system performance was evaluated using the rectified DC output voltage as the primary metric. Due to space restrictions, the 4 m and 8 m distance experiments were conducted in the spacious classroom, while the 3.2 m and 5.77 m experiments were performed in the anechoic chamber. The experiment setups and environments are shown in the following figures: **Supplementary Figure 42- 44**.

During the experiment, the transmitter was moved in horizontal and vertical directions with a 5 cm step, capturing 19 points at every specific distance. The moving method of the transmitter is shown in **Supplementary Figure 45**.

The rectified output voltages were captured using an oscilloscope. To ensure a consistent comparison with our previous results, we further constructed CDF plots for both a single rectifier output and the combined output across rectifiers. The combined rectifier output voltage was calculated based on the sum of the individual rectifiers. This CDF based presentation characterizes run to run variability and enables a direct comparison of performance distributions across the two environments.

As shown in **Supplementary Figure 46** and **Supplementary Figure 47**, the results show a clear and consistent gain from rectifier combining relative to a single rectifier no matter in the anechoic chamber or the classroom. This improvement is observed at both 4 m and 8 m, and it remains consistent across the anechoic chamber and classroom measurements, indicating that the demonstrated benefit is primarily attributable to the proposed receiver architecture rather than being an artifact of a particular indoor multipath condition.

As the receiver moves in horizontal and vertical directions, it definitely causes a change in the angle of the electromagnetic transmitting path, which affects the output due to the different gain at different directions of the lens system. To verify this, we built a simulation based on the MATLAB platform. We set the receiver to move in the same manner as in our experiment and designed the simulation environment to mimic an anechoic chamber. It can be seen that the simulation result is consistent with the experimental result, proving that the voltage variation comes from the angle change.

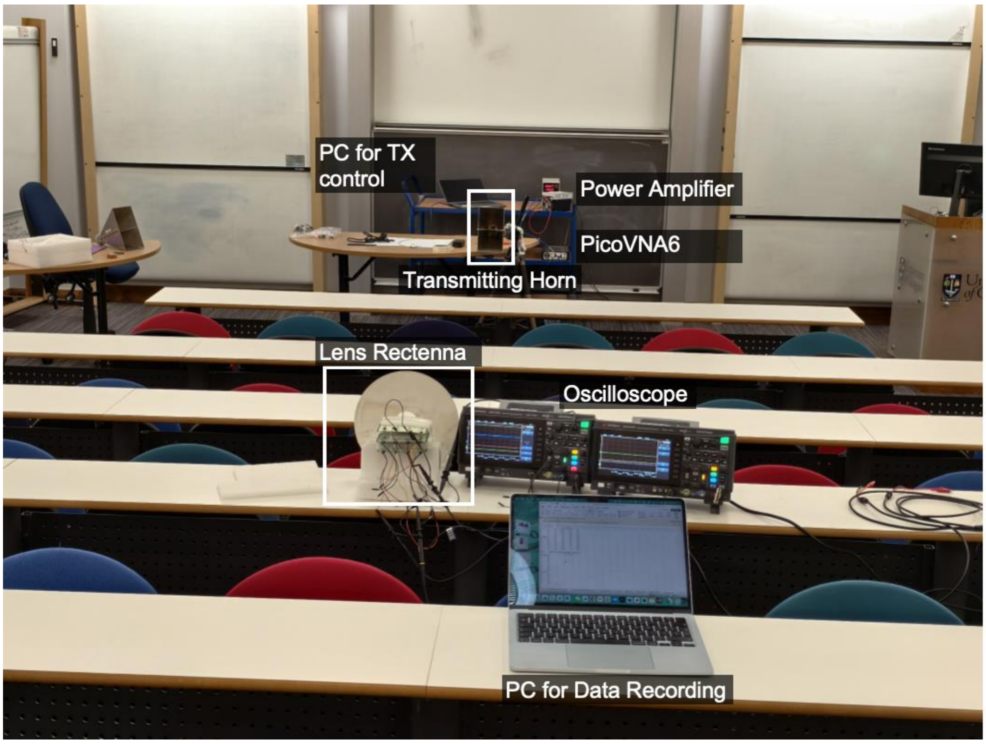

Supplementary Figure 42. Details of the measurement setup in a spacious room.

Supplementary Figure 43. Photograph of the measurement setup in a spacious room.

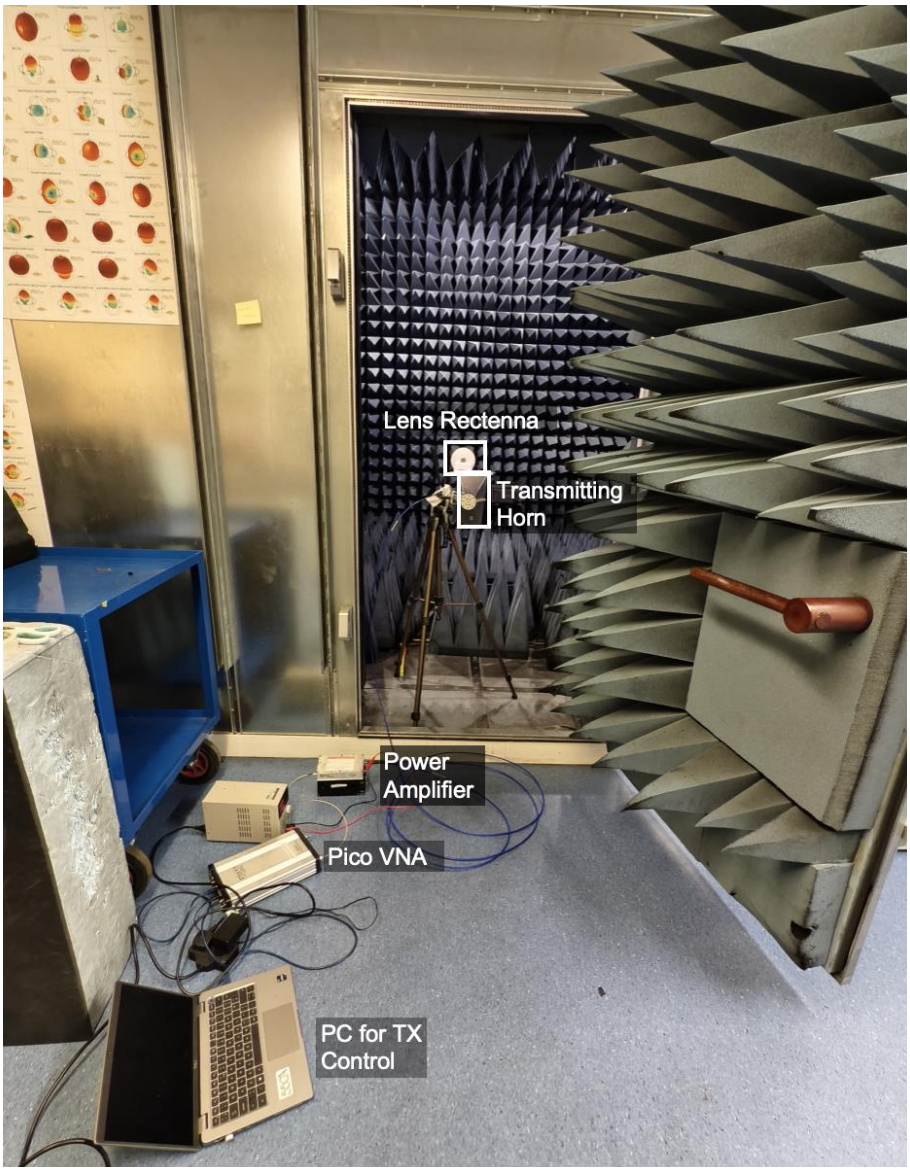

Supplementary Figure 44. Measurement setup of the antenna in an anechoic chamber

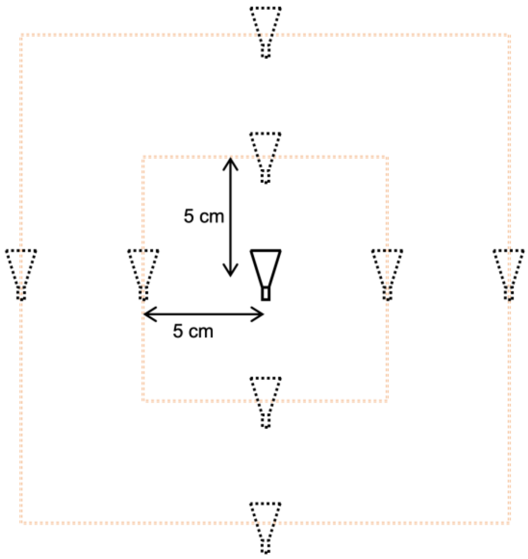

Supplementary Figure 45. The moving method of the transmitting horn antenna in the experiment.

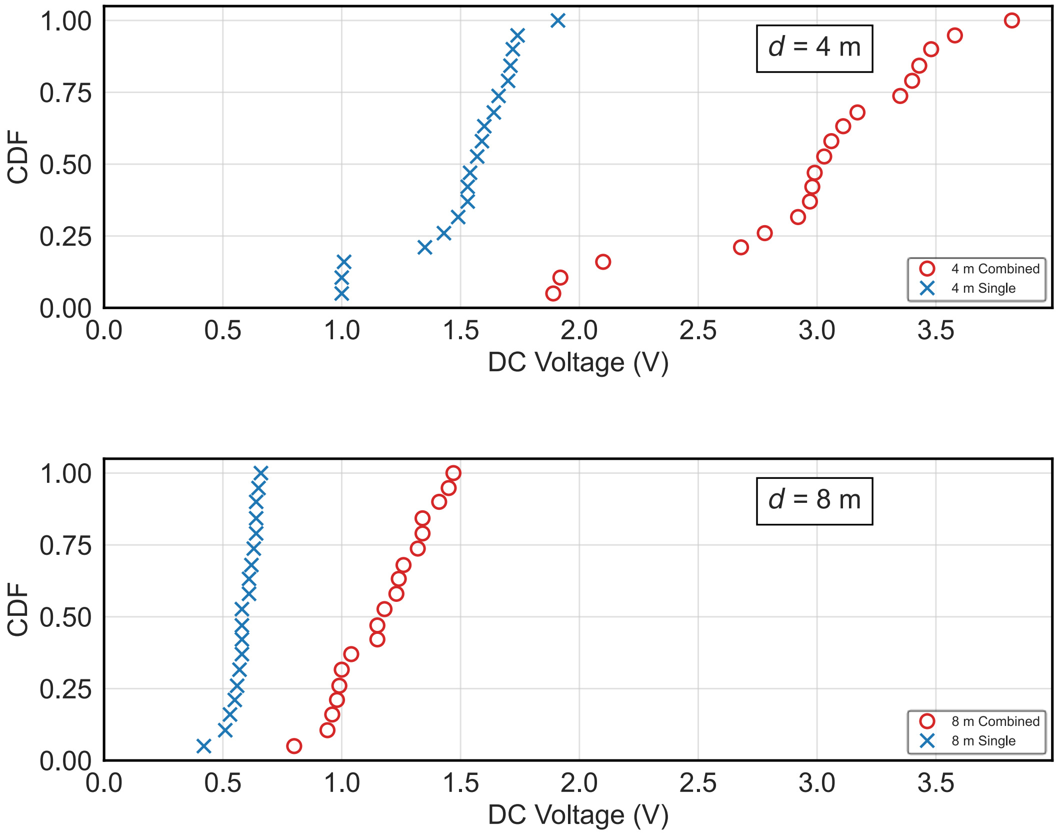

Supplementary Figure 46. Measured CDF of the DC voltage output in the spacious room.

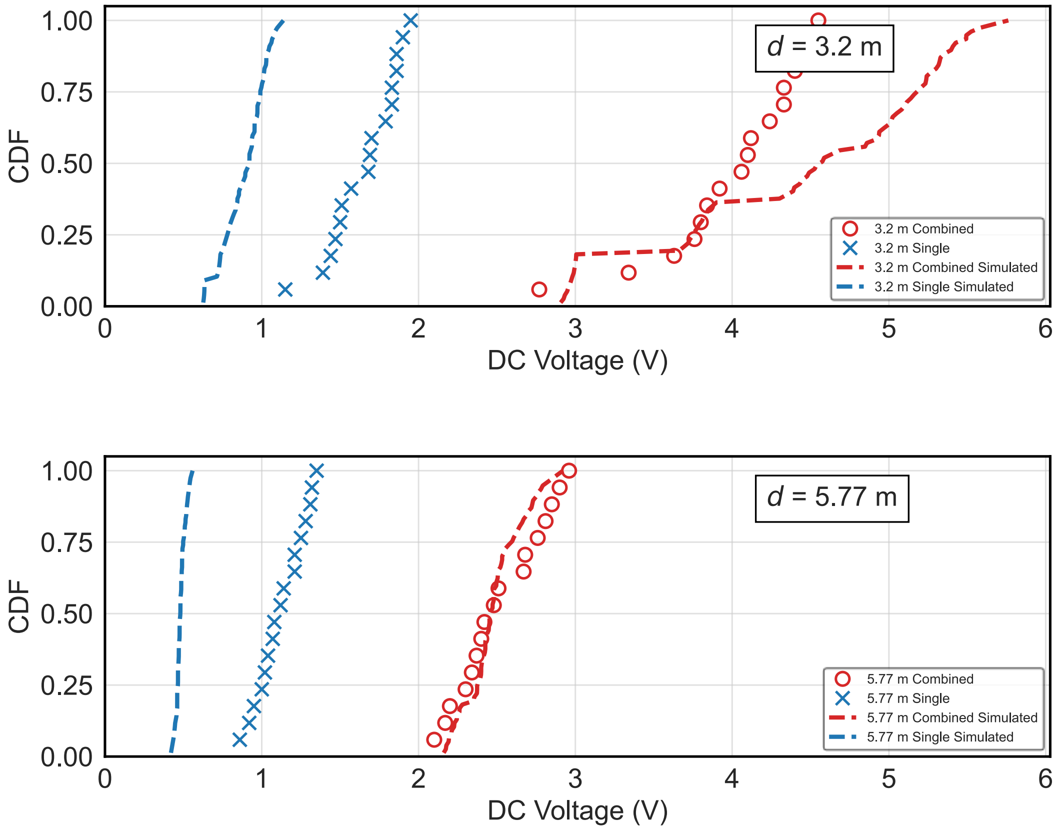

Supplementary Figure 47. CDF of the measured and simulated DC voltage output in the anechoic chamber.

Supplementary Note 10. SAR Analysis and User Safety

The Specific absorption rate (SAR) was evaluated in CST Microwave studio using a full-size muscle phantom (see the Methods section). Supplementary Figure 48 shows the electric *E*-field distribution between the transmitting lens and the person, illustrating the plane wave incident at the person, and the reflections leveraged in the sensing demonstration.

The reflected *E*-field from the person could also be observed in Supplementary Figure 48, this creates further wireless power paths which are harvested by the multi-directional rectenna, and is later exploited for the multi-directional RF sensing. The multi-directional harvesting can be observed in Figure 4(e) of the main text, where the voltage of the off-LoS channel increases, as a result of a person crossing the WPT path.

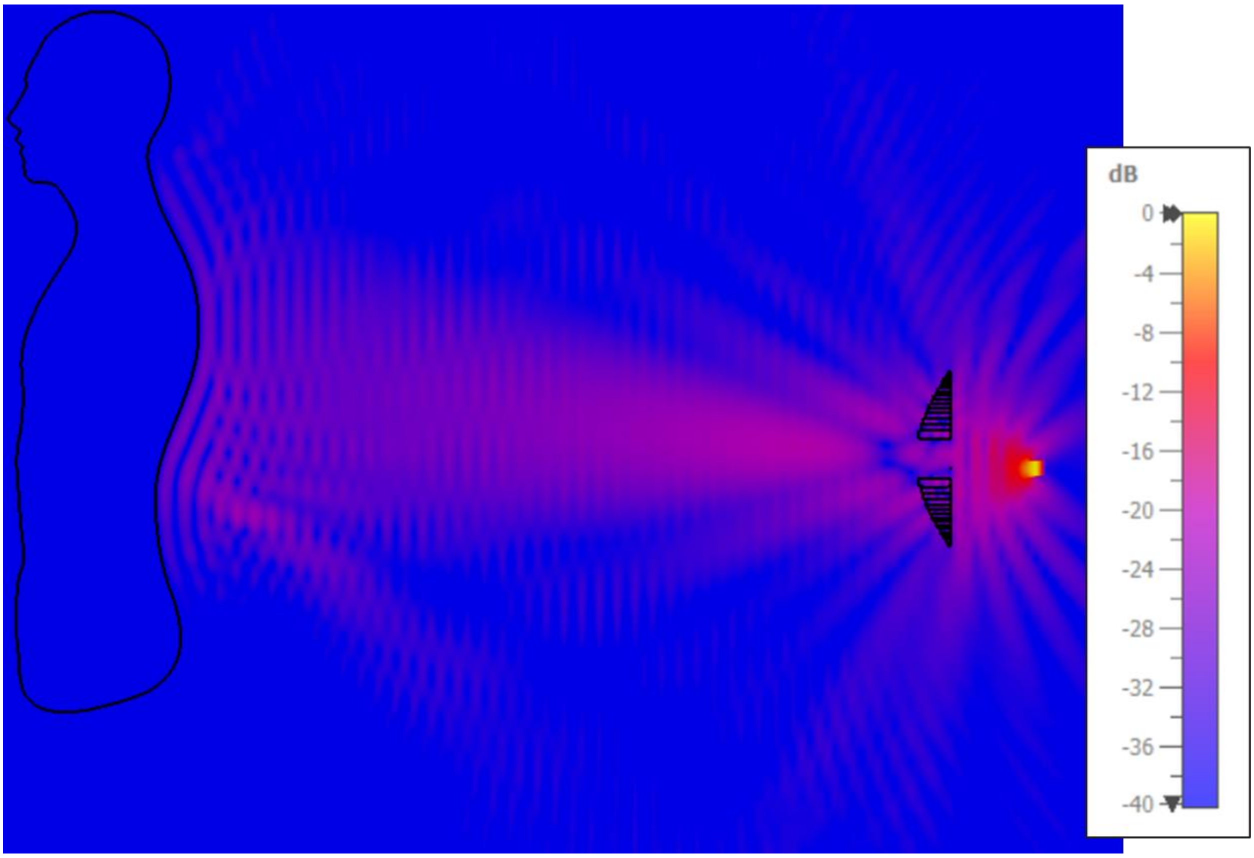

Supplementary Figure 48. Simulated E-field distributed for a lens-based wireless power transmitter, with a full-size muscle phantom at 1 m from the lens transmitter; only the torso is visible due to the field visualisation plane.

In terms of EIRP compliance, as the amplifier's power output is under 33 dB in the long-range powering experiments, with the transmitting horn antenna providing the gain for an EIRP approaching 55 dBm. All equivalent distance calculations for the varying RF power densities assume a 55 dBm EIRP.

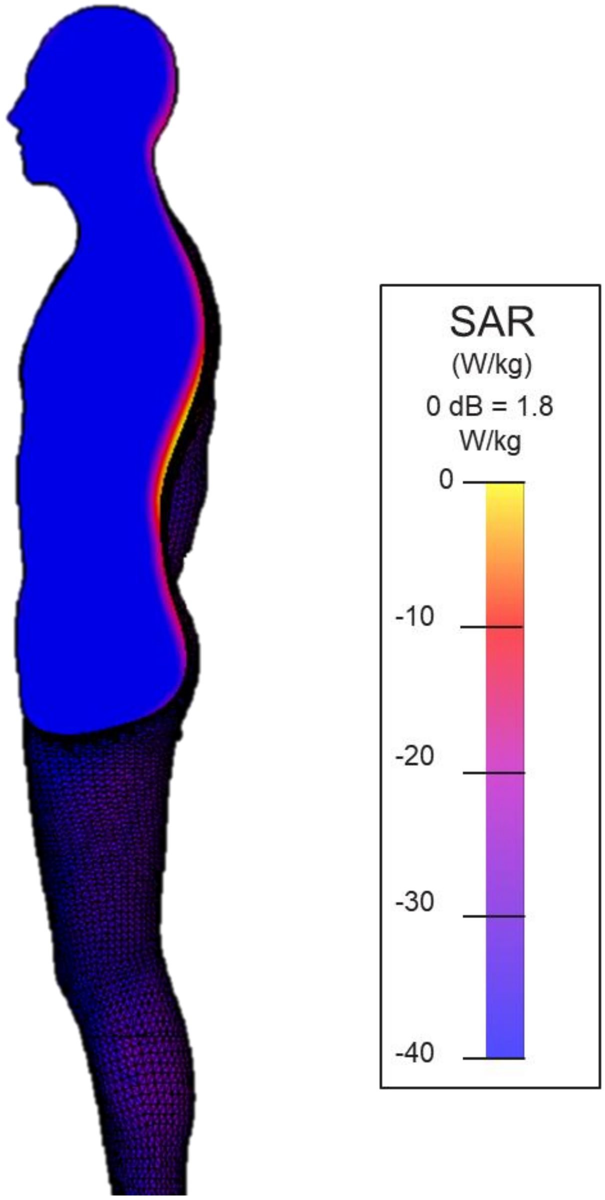

Supplementary Figure 49. Simulated SAR distribution in a full muscle phantom, showing compliance with the IEEE C95.1 standard for EMF exposure.

Supplementary Note 10. End-to-End System Efficiency

The end-to-end system efficiency in a far-field is given by:

$$\eta_{end\ to\ end} = \eta_{DC\ to\ RF} \times \eta_{channel} \times \eta_{RF\ to\ DC},$$

where $\eta_{channel}$ is generally dependent on the antennas' gain, distance between the transmitter and receiver, and the propagation environment. $\eta_{channel}$ dominates the "losses" in most far-field systems, and is typically under 1% (<-20 dB).

For our system, this was directly calculated using the DC output relative to the transmitter's power output/input power (including/excluding the amplifier's efficiency $\eta_{DC\ to\ RF}$, respectively), using:

$$\eta_{system} = \frac{P_{DC,RX}}{P_{TX}}.$$

Assuming an ideal 5 W source is used ($P_{TX} = 5$ W), as the DC to RF efficiency falls outside the scope of our work, the system efficiency is shown below, as a function of the power density. The power density corresponds to the equivalent distance between the transmitter and the receiver:

$$S = \frac{P_{TX} G_{TX}}{4\pi d^2}$$

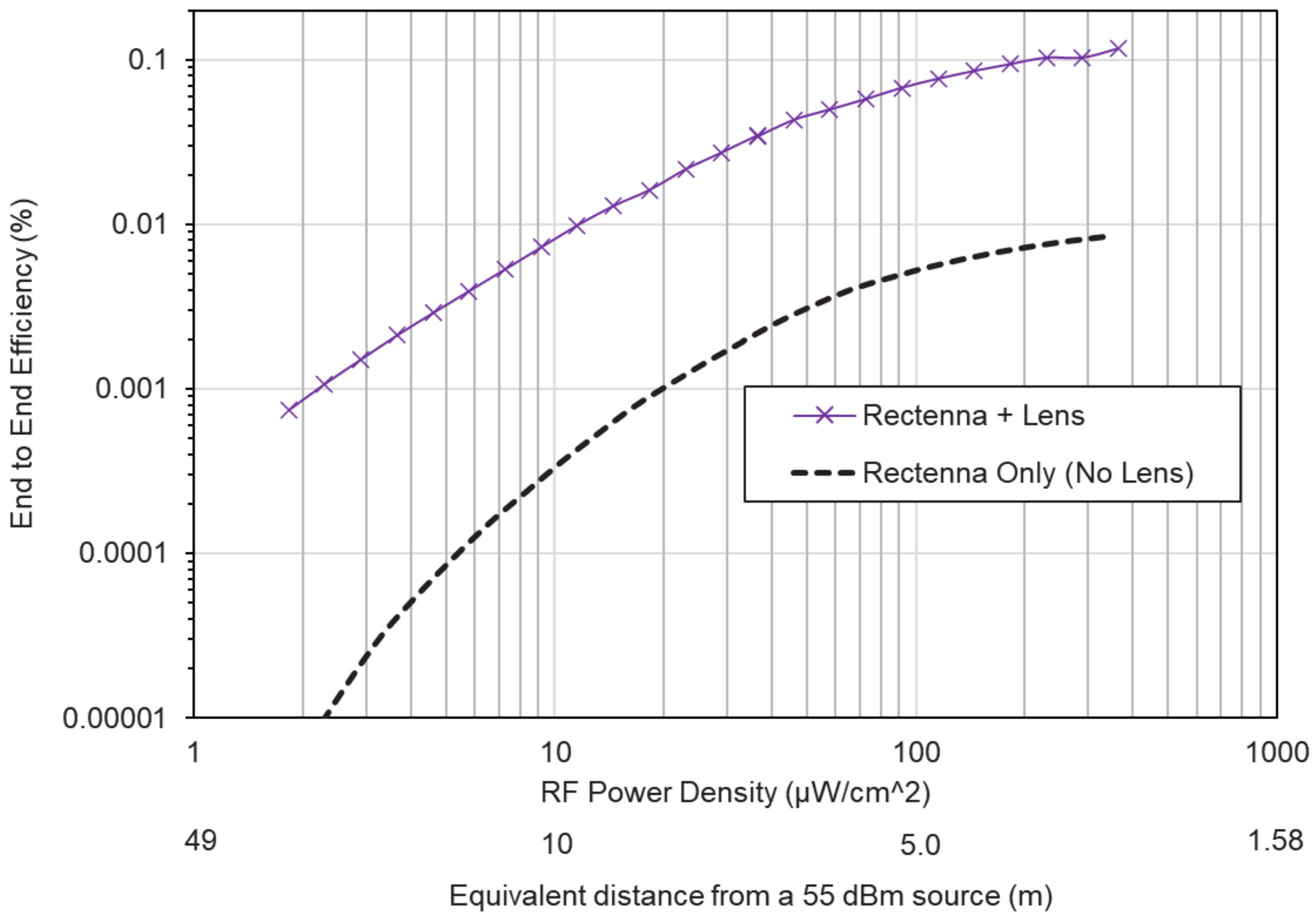

Supplementary Figure 50. End-to-end efficiency of the proposed system, assuming a 5 W input is required to operate the 55 dBm transmitter.

It is however key to note that this efficiency calculation, inclusive of the path loss component due to spherical spreading only applies to a single receiver, and the inclusion of additional receivers would increase the efficiency, as the collection area is increased for the same incident power density and required source DC power. Most far-field RF power transfer studies do not present end-to-end efficiency figures; thus, a direct comparison is not possible. To illustrate, for a 2° beamwidth transmitter, the antenna spot size at 30 m away is approximately 1 m^2, which could accommodate up to 9 lenses focusing power on the rectennas.

Supplementary Note 11. Multi-Frequency Operation and Frequency Hopping.

The FCC 15.247(c)(1)(ii) directives permit an EIRP up to 55 dBm for point-to-point, digitally-modulated and frequency-hopping systems. While WPT is demonstrated in this work using a continuous wave (CW) signal, performance and efficiency improvements can be obtained using multi-sine OFDM-like waveforms [S41]. In addition, the rectifier, given its wide bandwidth, can operate efficiently under a range of frequencies with a relatively unchanged DC voltage output.

To investigate the feasibility of frequency hopping, a PicoVNA6 was used as the signal source with a 40 MHz sweep, where the output RF signal (around 0 dBm) is swept between 5.5925 GHz and 5.6324 GHz. Supplementary Figure 51(a) shows the measurement setup, where the rectifier's input is monitored using a directional coupler (-20 dB) on a real-time spectrum analyzer (RTSA). The rectifier's DC voltage output was monitored simultaneously using an oscilloscope.

The measured RF power level, in Figure 51(b), and the DC power output, in Figure 51(c) show that the net variation in the DC output is under 5% of the peak voltage, for a frequency-hopping input across the 40 MHz measurement bandwidth. This shows that the proposed system could potentially fit under the FCC directives for 5.8 GHz systems, with the frequency-hopping capability used to mitigate interference. The occupied bandwidth of the CW signals used in the experiments is under 1 kHz, and only limited by the phase noise/spectral purity of the signal sources used.

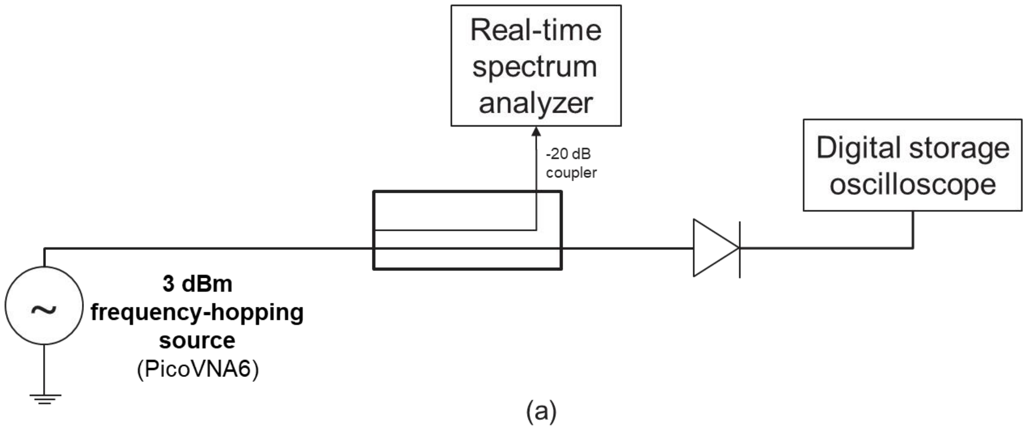

(a)

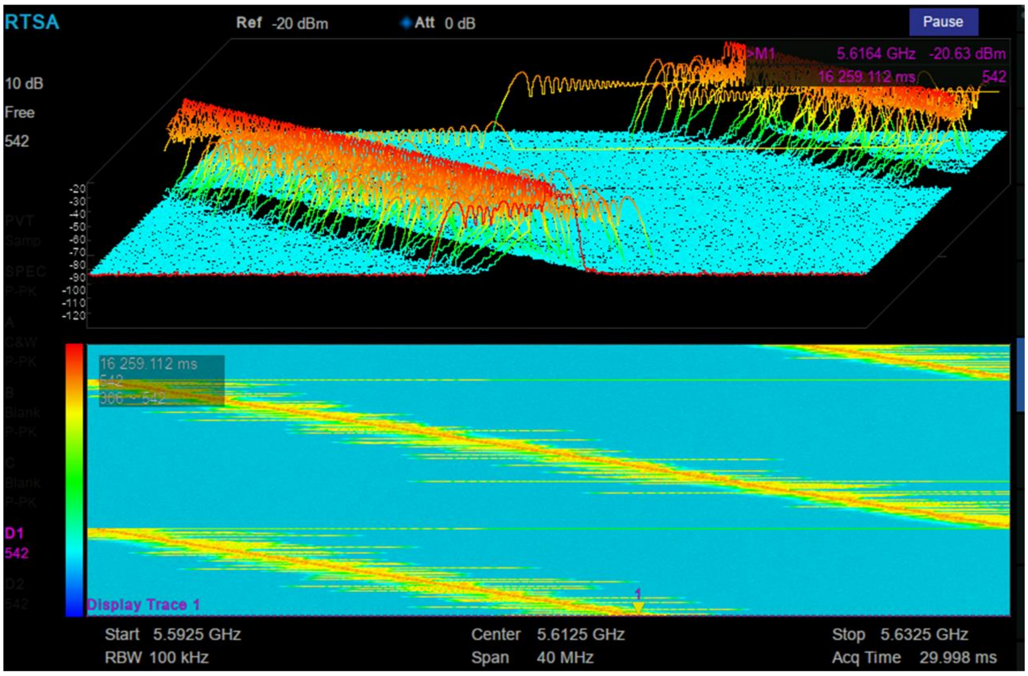

(b)

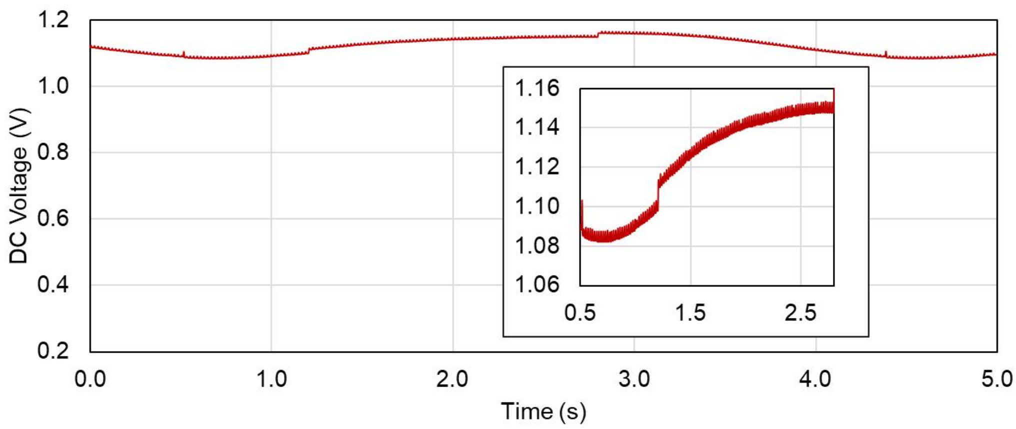

(c)

Supplementary Figure 51. Measured output of the rectifier in frequency-hopping conditions: (a) measurement setup using a frequency-sweeping VNA, with a <10 kHz bandwidth; (b) measured time-varying spectrum of the input to the rectifier over multiple cycles, hopping over a 40 MHz bandwidth; (c) DC voltage output showing under 10% variation over the 40 MHz hopping bandwidth.

Supplementary Note 12. Bluetooth Sensor Powering and Associated DC Power Levels.

A Bluetooth Low Energy (BLE) Arm Cortex-M4 SoC was powered without a battery at various distances from 14 m to 32 m. As seen in the power sweeps, a range of around 31.5 m in an open environment for a load with a 1.1 V requirement.

The SoC is based on Texas Instruments CC2640R2F, and is programmed to transmit modulated data in BLE beacon packets at 1 s intervals. This load represents a typical computational sensor node. A simple BLE sensory beacon based on the Inplay IN100 beacon, which requires a minimum of 1.1 V to operate. Supplementary Figure 52 shows the measurement environment in a long corridor, where the voltage traces were recorded. As the tests are conducted in an enclosed environment with concrete floor / ceiling with steel reinforcements, it will be expected that the multi-path reflections could add to the received power, through the detailed power combining mechanism.

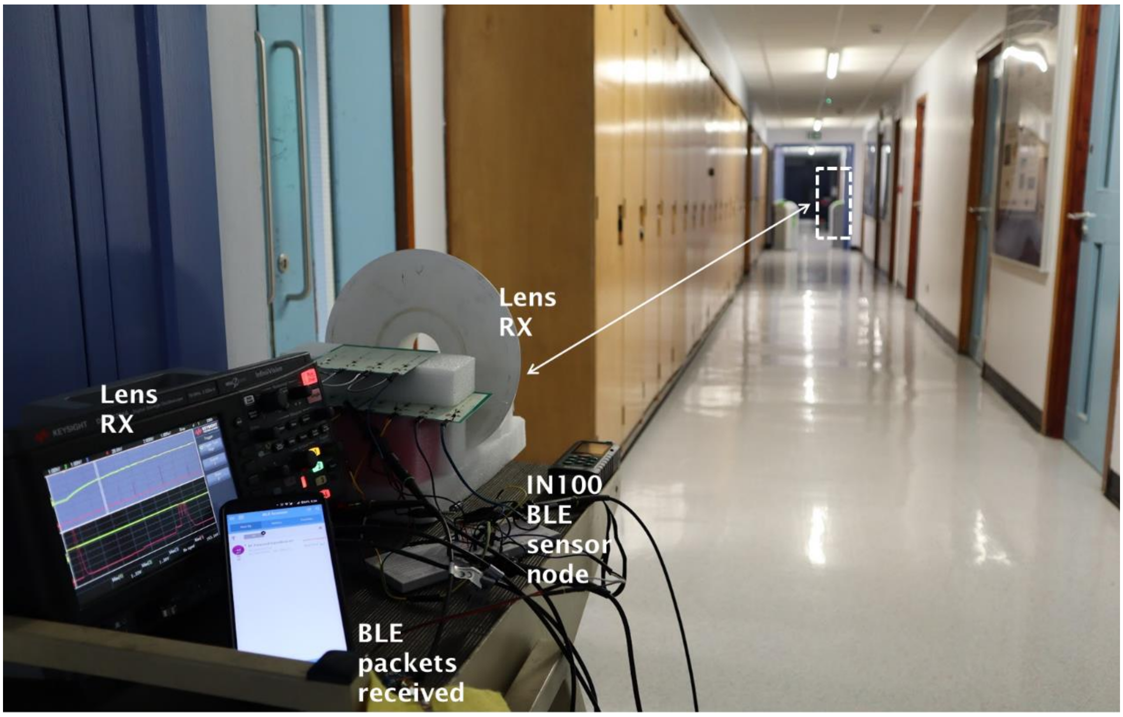

(a)

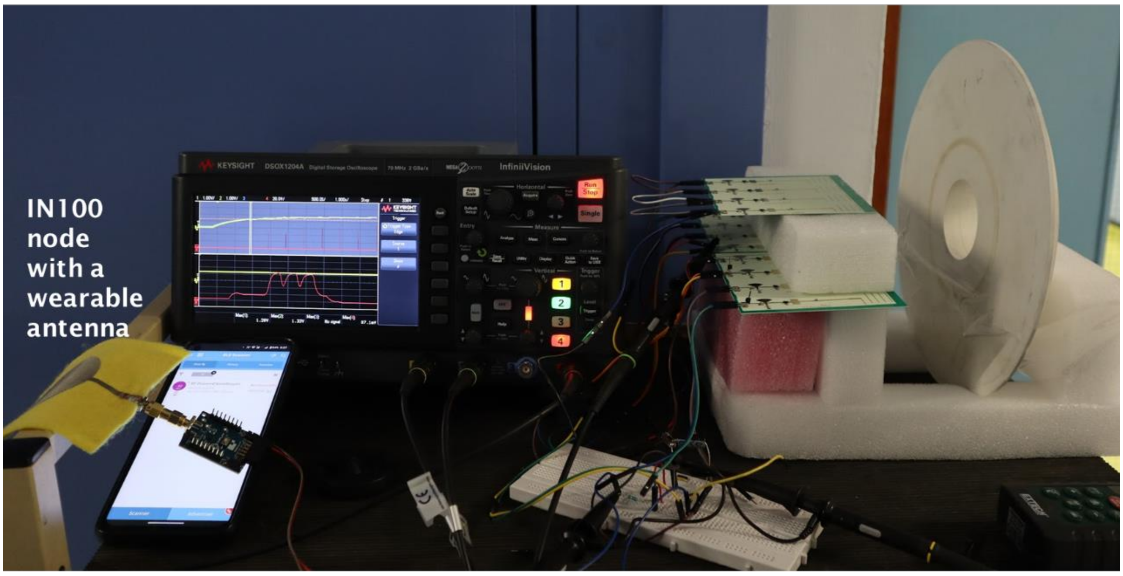

(b)

Supplementary Figure 52. The wireless-powering setup of the battery-free BLE sensor beacon, at a distance of 32 metres from the transmitter: (a) photograph showing the wireless power transfer range; (b) the wireless-powered BLE sensing beacon.

The average charging power used to power the BLE sensors (both the Arm MCU-based and the static IN100 sensing beacon) was calculated based on the energy stored in the capacitor. The received DC power output is calculated as:

$$P_{\mathrm{avg}} = \frac{CV^2}{2} \times \frac{1}{t_{\mathrm{charge}}}$$

where C and V are the capacitance (660 μF) and instantaneous voltage level, respectively, and t_charge is the time instance at which the average charging power is calculated. The measured average DC power input is shown in Supplementary Figure 53.

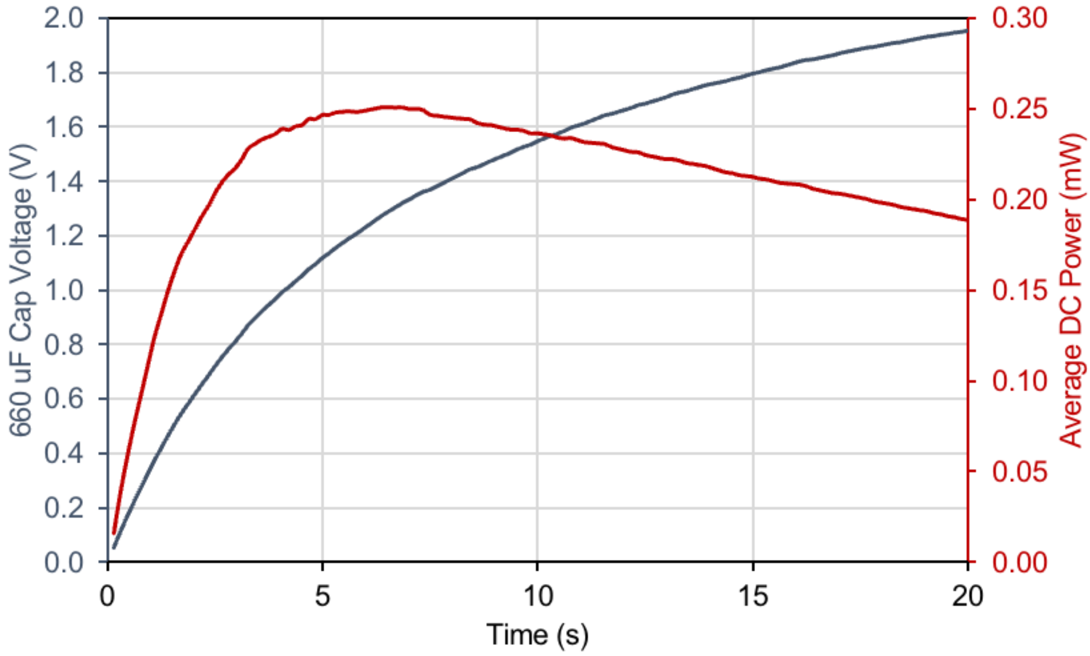

Supplementary Figure 53. Average capacitor charging power, at 32 m, for the 660 μF capacitor in the setup shown in Figure 4(d)-(f).

The relation between the capacitor size and the charging time is inversely proportional, where a larger capacitor C would require a longer charging period t_{charge}. However, for the same series of capacitors with similar parasitic resistance, the net average power level (P_{avg}) will remain constant.

12.1 Open Environment Testing:

To explore the path-loss variations, in DC, in an open environment, measurements were conducted in the setup shown in Supplementary Figure 54. While the test is carried out in an indoor space, it features a significantly higher ceiling and wider space, leading to the main reflected component coming from the ground reflections, as opposed to from the ceiling/ground multiple reflections, which can create a more multipath-rich environment. The DC power output was measured at 3 distances, in order to (a) observe the trend against distance, and (b) demonstrate that the system can still produce >1.1 V needed to operate the BLE beacon.

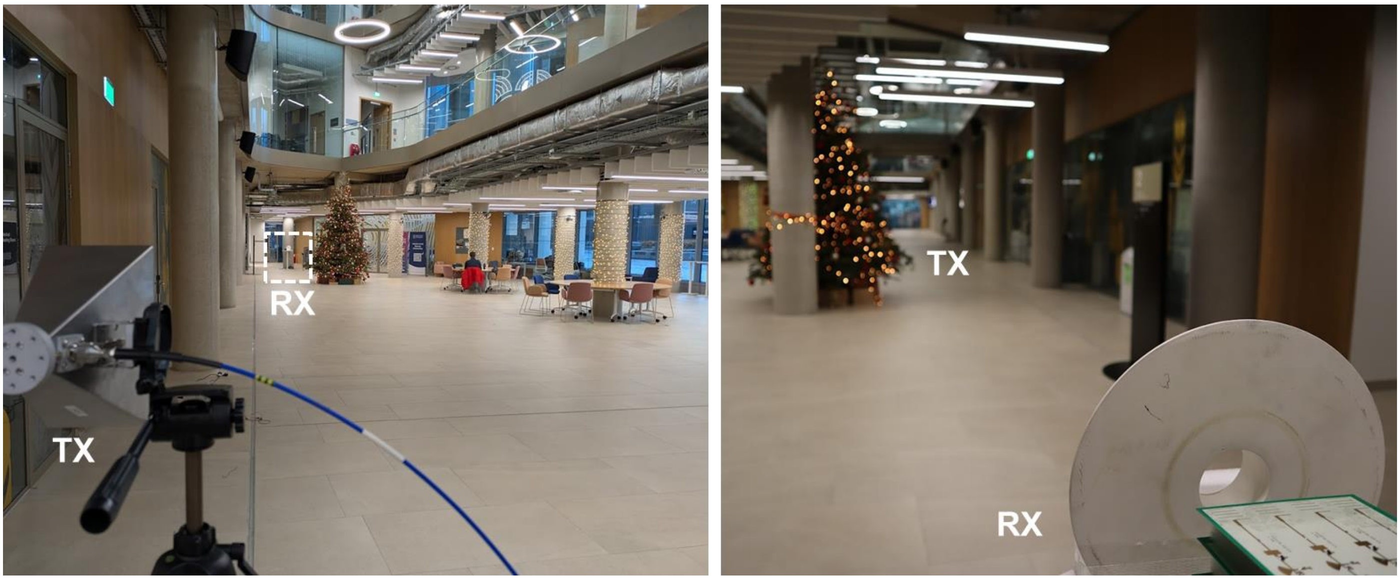

Supplementary Figure 54. Photographs of the 2nd, open, measurement setup for additional validation showing the transmitting horn (left) and the wireless power receiver (right).

The measured DC power output, from the 12 combining rectennas, is shown in Supplementary Figure 55. As in Supplementary Figure 55(a), the trend in the received voltage and consequently power is similar to that observed in the more confined indoor space. The curve for the received power level indicates a path-loss exponent n = 1.73, close to that observed in the 1-12 m distance sweep with 6 rectennas (in Supplementary Figure 39).

The power levels are, however, lower than the confined environment, leading to a peak output voltage level of 1.4 V, at 30 m, as opposed to the previously obtained 2 V at 32 m, in the closed corridor environment. This shows that the power combining approach operates more optimally in multipath-rich environments. Nevertheless, the net output >1.1 V would still enable the BLE beacon to be powered, and the improvement in the path-loss exponent, n, is still observed.

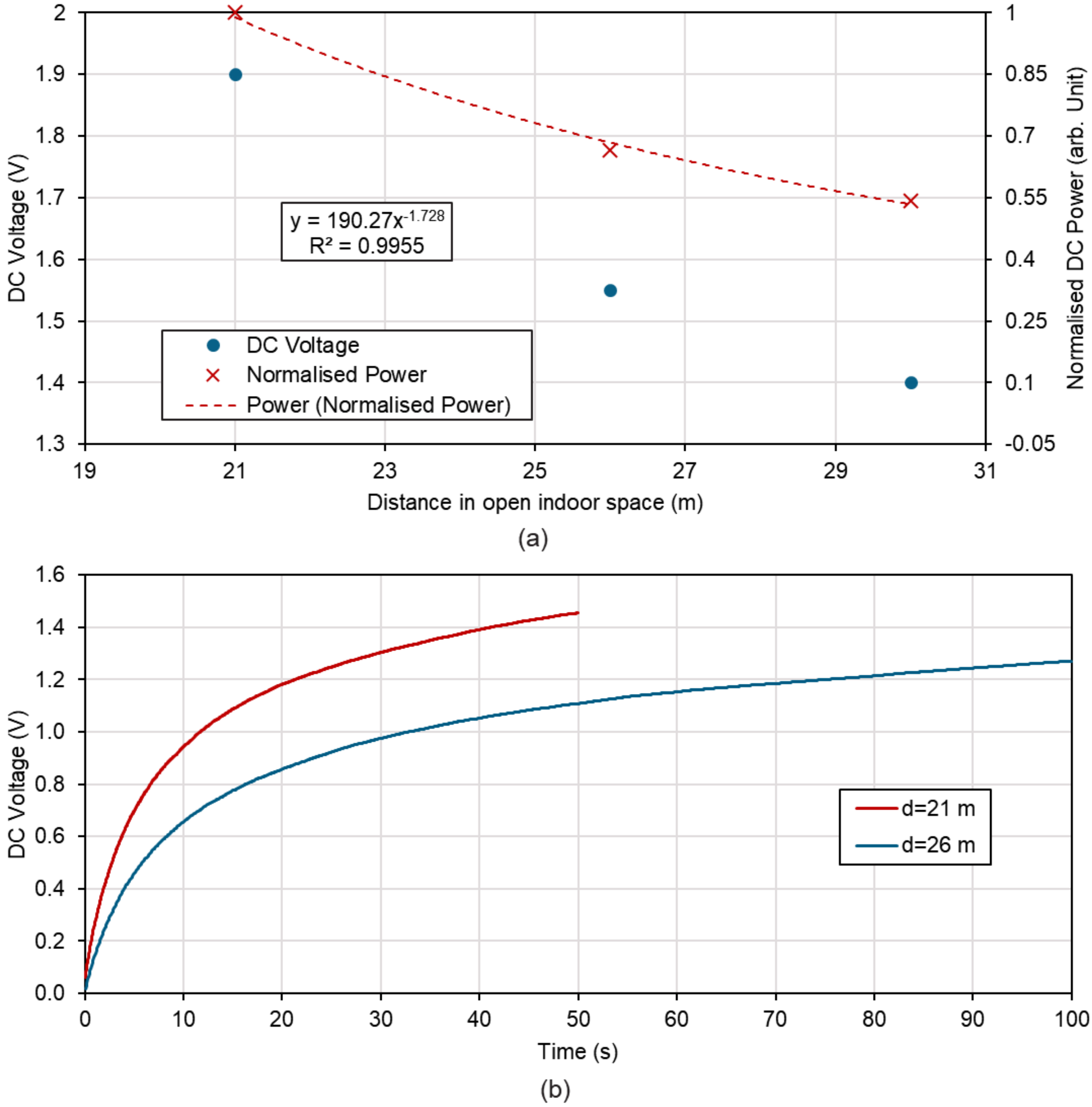

Supplementary Figure 55. Measured DC power output in the open environment: (a) peak DC power output, showing a consistent path-loss exponent and R^2; (b) stored voltage in a capacitor at different distances.

Supplementary Note 13. Joint Power and Sensing Setup with Antenna-Based Sensitivity Enhancement

Unlike conventional RSSI-based active RF sensing systems (e.g., Wi-Fi routers, RFID readers etc), the proposed system uses passive components to enhance the sensitivity. Thus, the lens antenna's gain can increase the wireless range of the sensor. This is particularly useful for sensing changes outside the boresight LoS WPT path, as in the breathing demonstration in Figure 56(a) to (c) of the main text.

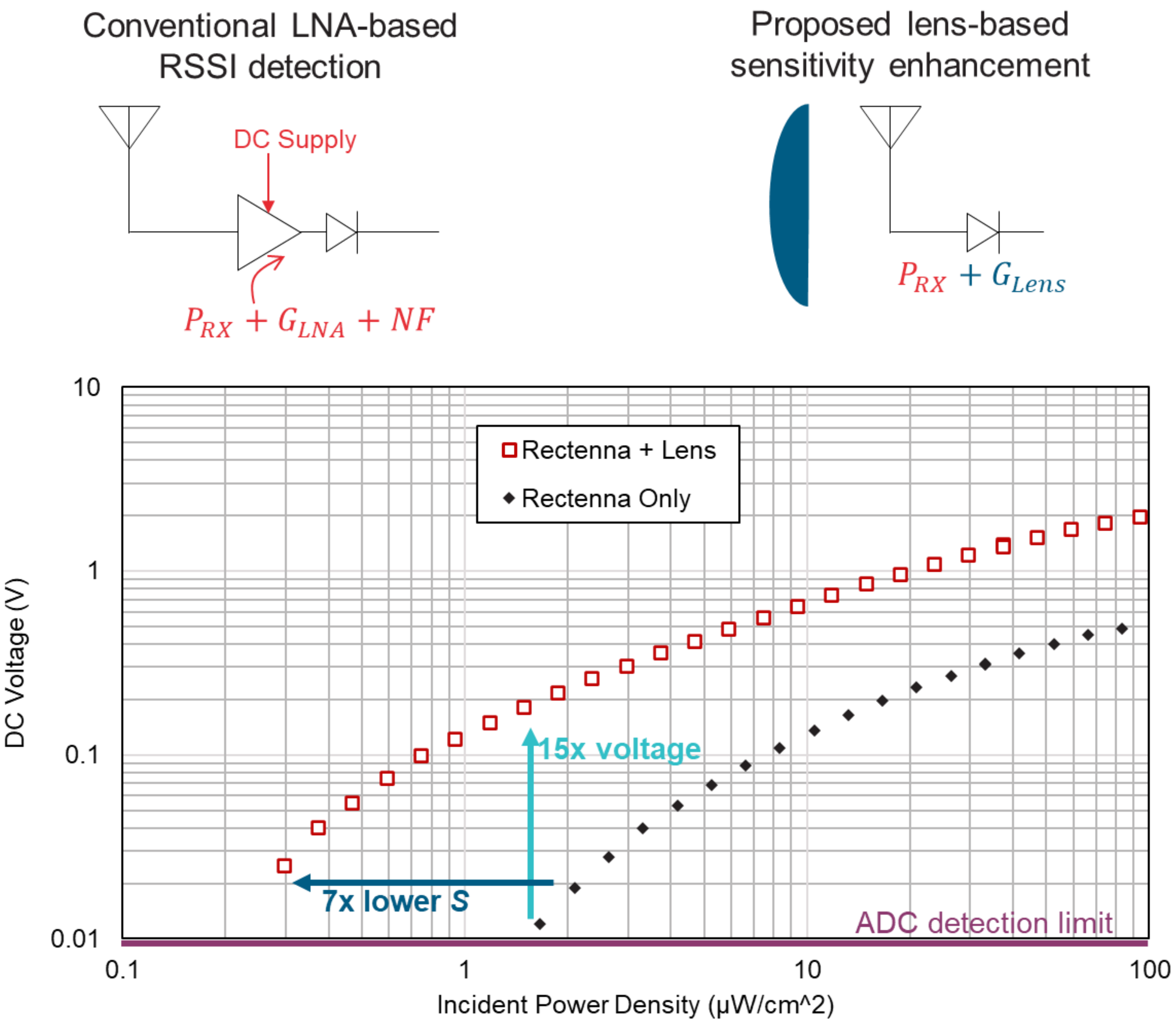

Supplementary Figure 56. Illustration of the sensitivity and range improvement in our passive receiver, offered by the high-gain rectennas.

Supplementary Note 13. Breathing Sensing Details and Signal Processing

Illustrating the feasibility of sensing while not interrupting the WPT link, a demonstration where the test subject is sitting outside the main LOS WPT beam was setup, as shown in Supplementary Figure 57.

Four rectennas were placed behind the lens, with the 4th rectenna focused on the maximum azimuth angle which the lens can cover, approximately where the test subject is located. Thus, illustrating how a lens-based receiver could provide wide angular coverage for passive joint RF sensing and powering.

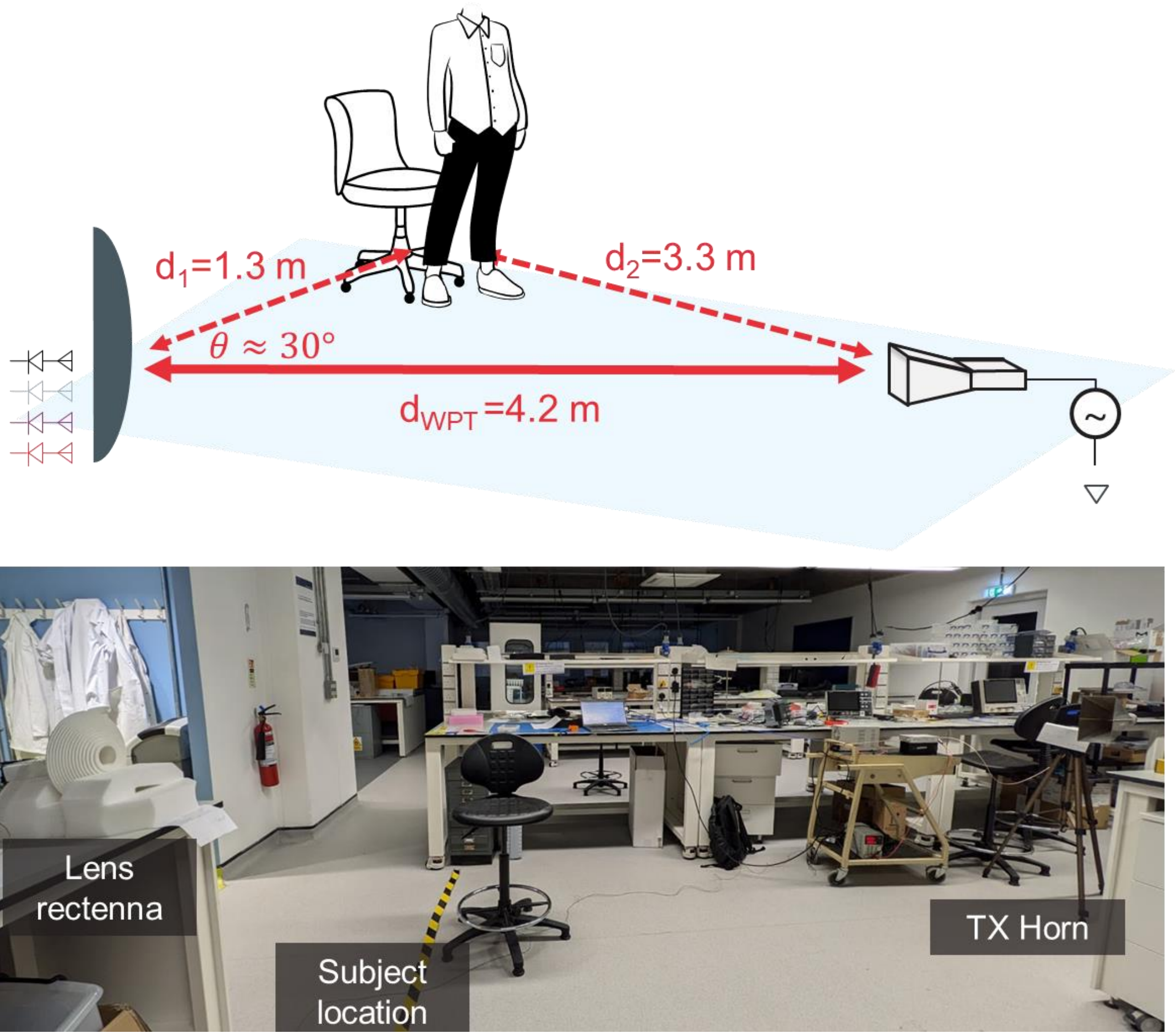

Supplementary Figure 57. Setup for the RF JSAP for breathing monitoring experiments.

The measured DC voltage traces, sampled at 10 Hz, are shown in Supplementary Figure 58, across the 4 channels. In line with the previous power combining observations (Supplementary Note 9), the two central receivers capture the most RF power, and would therefore be the two major contributors to charging a device. Both Channels 1 and 2 exhibit periodic changes, particularly after the subject stands, around t=35 s. This is attributed to the increased LoS blockage by the subject, in Channel 1, causing additional reflections and consequently increasing the received power on Channel 2.

In Channel 4, the breathing pattern is most clearly observed without any filtering/data processing. This is due to rectenna 4 being focused on the test subject's position, and its reception is primarily reliant on the varying reflections from the subject's inflating/deflating chest. It is key to note that the received voltage amplitude falls under 0.2 V for both the standing/seated cases, which indicates an incident power density, in this direction, of S<1 μW/cm^2. As such, such waveform would not be measurable using a standard receiver, without the antenna-based sensitivity/gain enhancement, illustrated in Supplementary Figure 56.

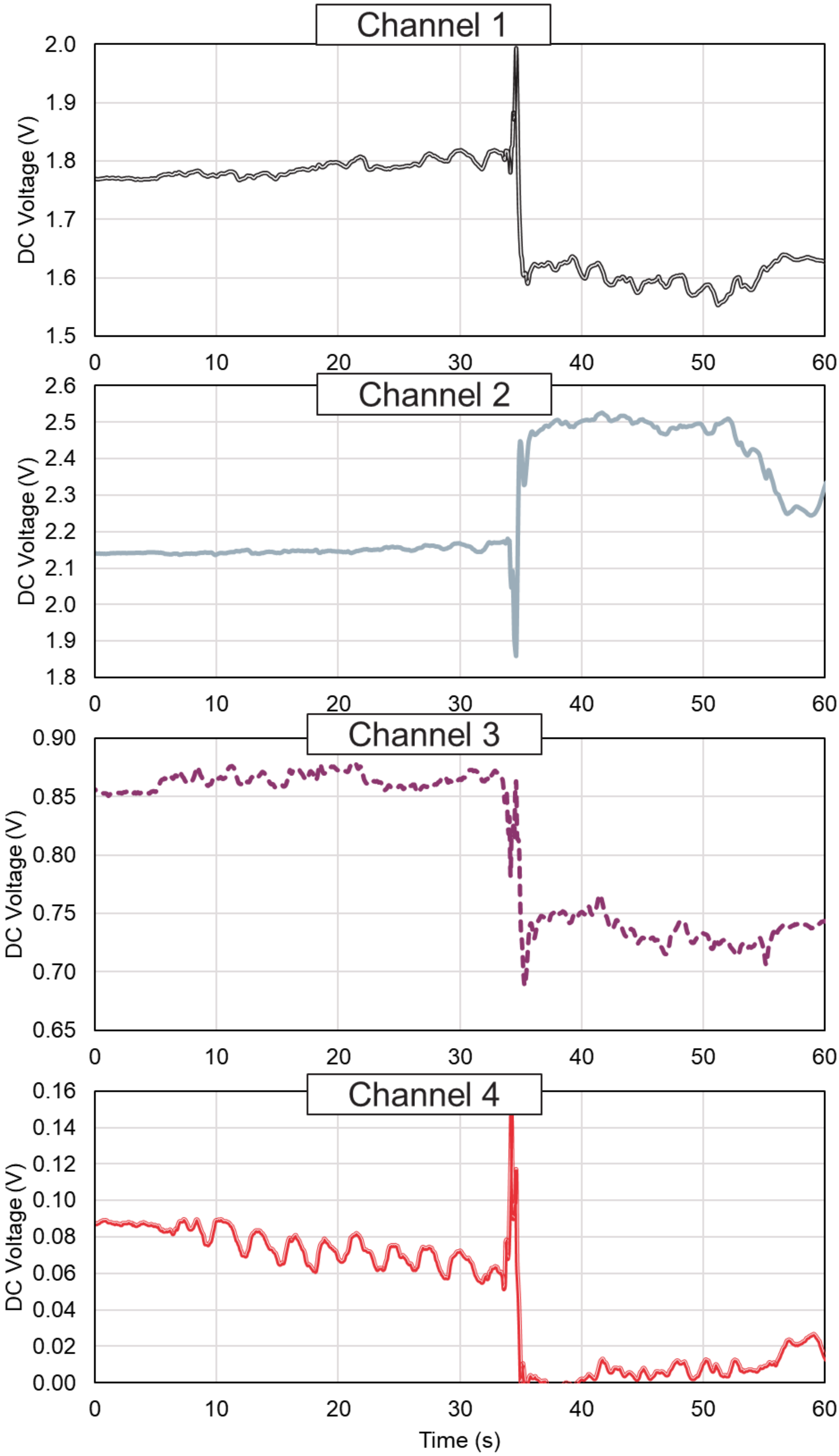

Supplementary Figure 58. Measured DC voltage waveforms on the individual rectenna channels.

To extract the breathing rate of the subject from the data, the voltage waveforms were normalized over 30 s time windows, using

$$V_{normalised} = \frac{V_t - \min(V)}{\max(V) - \min(V)}.$$

The data was then Fast Fourier Transformed (FFT), giving the response shown in Supplementary Figure 59.

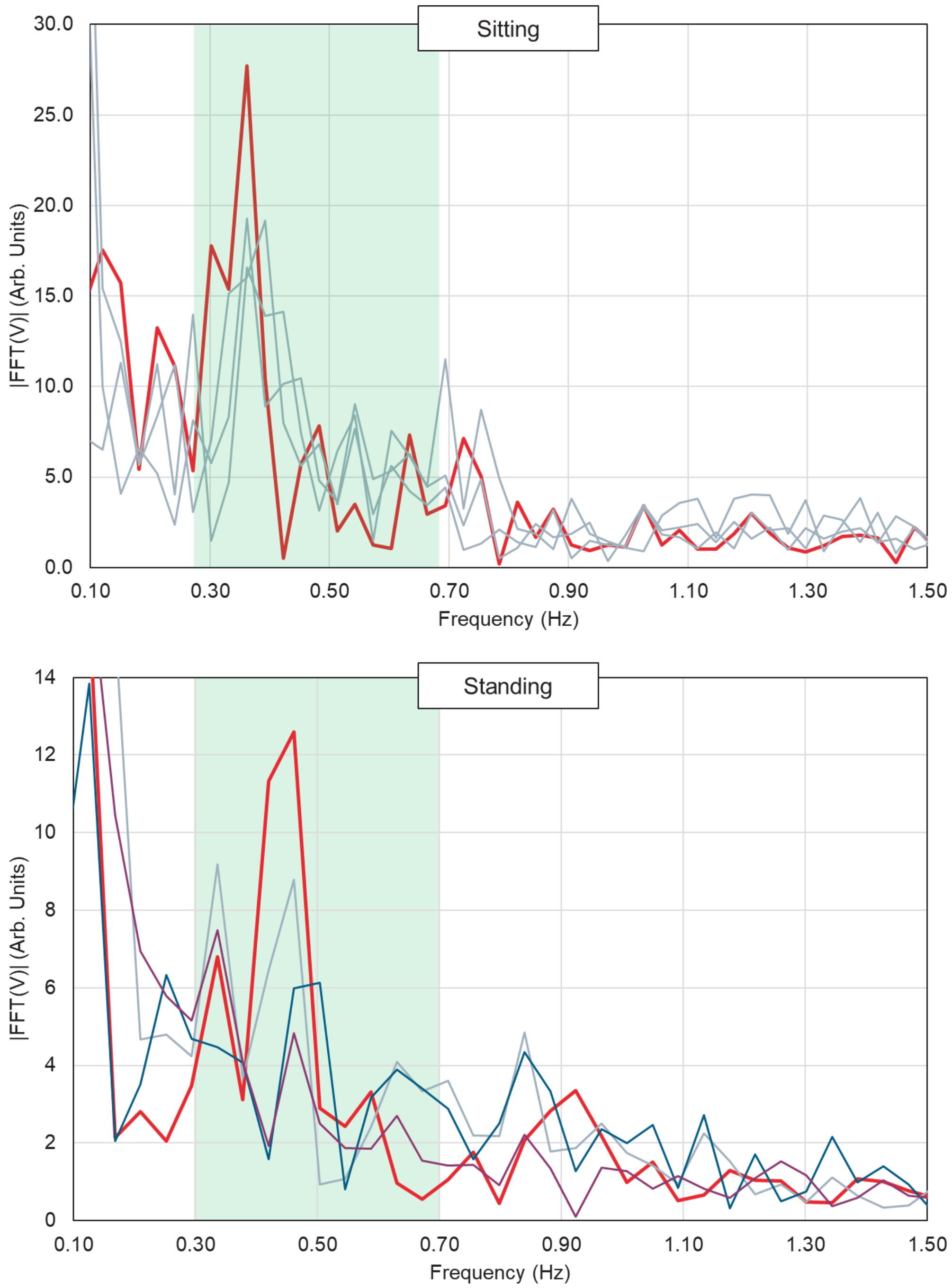

Supplementary Figure 59. Frequency domain response of the DC voltage variations, showing the breathing frequency across the four rectenna channels; the shaded part indicates the observation band for the breath sensor.

Supplementary Note 14. Machine Learning-Assisted Sensing Setup and Comparison

Supplementary Note 14.1. Receiver System Topology

The schematic and photograph of the receiver system used in the wireless power-based localization experiments are shown in Supplementary Figure 60. The output voltage of each rectifier is measured separately with the help of Arduino board to increase the prediction accuracy. With the wide angle range the rectifies can watch out, subjects can be localized in the detection area. The measured data will be transmitted to the computer to deal with and make predictions. The microcontroller of the Arduino board records the data points at a rate of 20 Hz. The code used to drive the Arduino board for sampling the DC voltage waveform was programmed in C using the Arduino IDE.

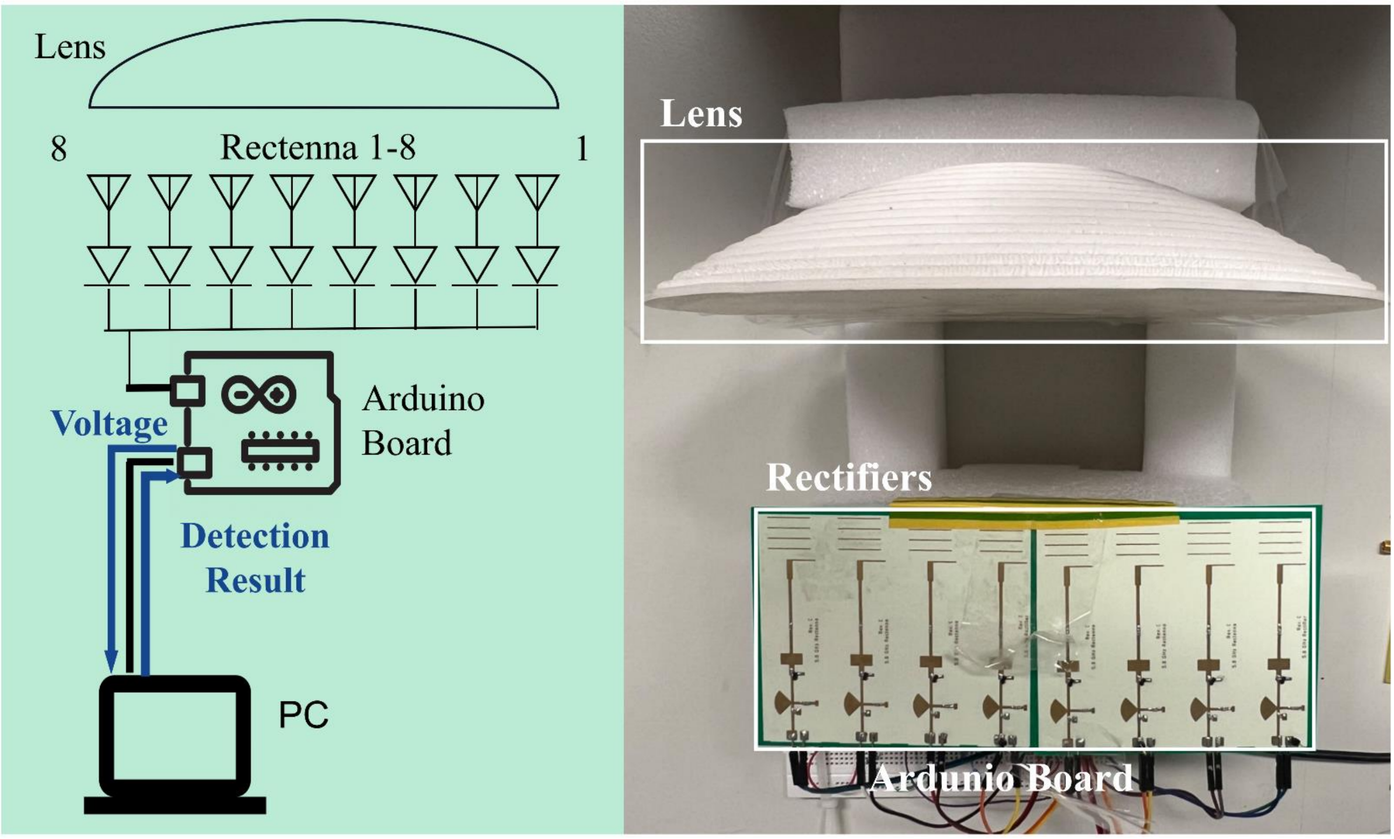

Supplementary Figure 60. The topology and top view of the receiver system.

Supplementary Note 14.2. Three Different Prediction Methods and Comparison

Three distinct methods were utilized to predict the system's state: a table lookup method, K-nearest neighbours (KNN) classification algorithm, and deep neural network (DNN) classification, implemented on the TensorFlow platform. The performance of each method was evaluated using both unnormalized and normalized datasets.

The detection system employed eight rectennas, producing output voltages designated as V1 through V8. As shown in Supplementary Figure 61, the voltage ranges across different channels exhibited significant overlap, complicating the task of accurately associating input data with the predefined training data ranges.

We prepare the data by loading and organizing it for the model. The training and testing datasets were separately collected through the same procedure with 1,800 and 1,200 samples, respectively, each being 90 and 60 seconds-long. The training dataset was set as 5,000 points with 1000 per situation. The test dataset was 2500 points with 500 per situation. The prediction results of horizontal location experiment in Space 3 Long is shown in this section for comparison. The comprehensive performance of the deep learning method and KNN method could be checked in Supplementary Note 15.

The codes for prediction was programmed in Visual Studio Code IDE with Python language (Python Version 3.10.11 64-bit). A Dell Latitude 5440 PC was used to run the train & test process and perform the real-time classification.

ML-Free Bencmark, A Look-Up Table Comparison-Based Approach:

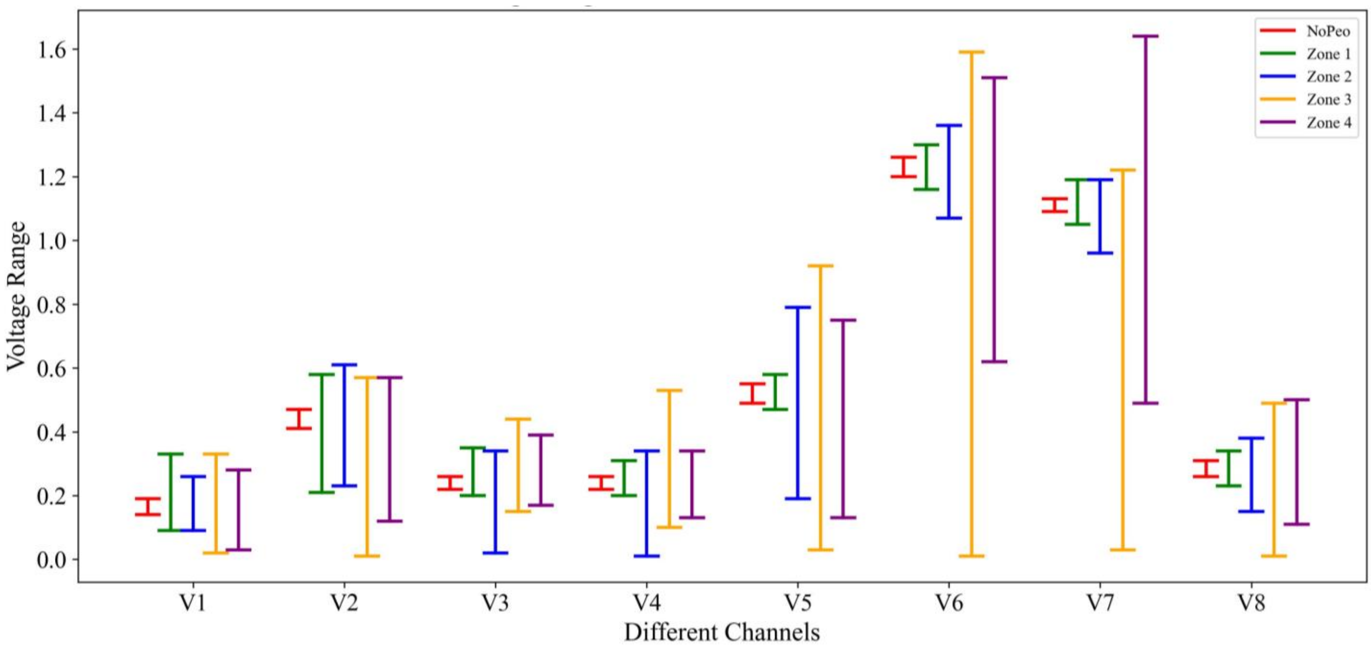

Supplementary Figure 61. The output voltage range of different channels corresponding to different situations.

The table lookup method determines predictions by comparing input data with the voltage ranges of the training dataset for each scenario. Predictions across the eight channels are aggregated, with the scenario receiving the highest vote being selected as the final result. The confusion matrix representing the prediction result based on unnormalized data is shown in Supplementary Figure 62. The method yielded suboptimal results, as evidenced by its low accuracy. The overlapping voltage ranges severely impacted its efficacy, particularly for unnormalized data where the accuracy was 32.96%.

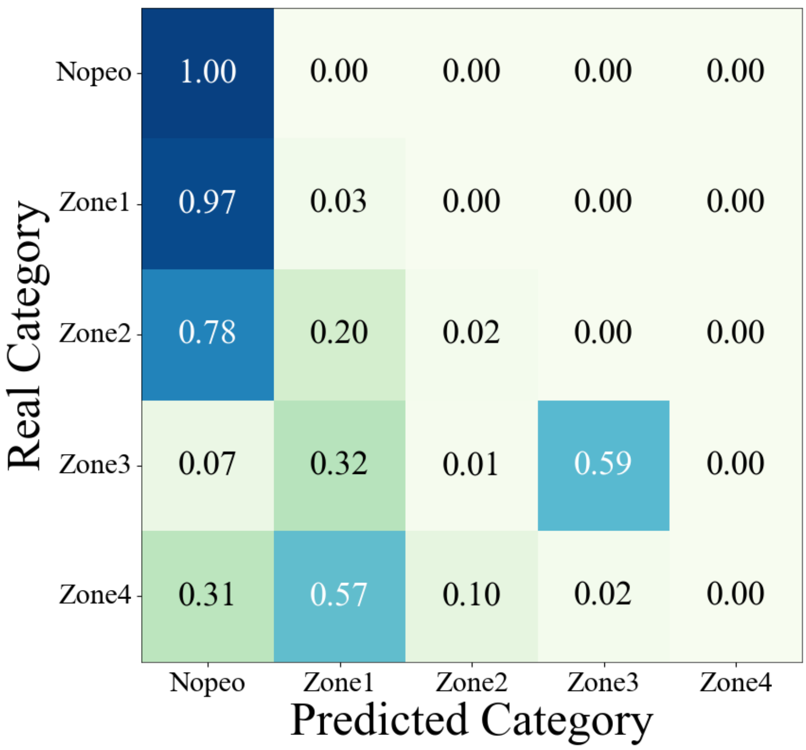

Supplementary Figure 62. The confusion matrix illustrating the horizontal localization accuracy in Space 3 (Long case) with the lens, using unnormalized data and table lookup method.

KNN and DNN Classification:

The KNN method aggregates the rectenna voltage outputs (V1 to V8) into a single vector and identifies the KKK nearest vectors in the training dataset based on distance metrics. The final prediction corresponds to the scenario most frequently represented among these neighbours. This method does not require repeated training processes and benefits from its simple computational procedure and low hardware requirements, demonstrating significant advantages. The confusion matrix representing the prediction result based on unnormalized data is shown in Supplementary Figure 63. It could be seen that the KNN method achieves the highest accuracy among all situations, with an overall mean accuracy of 95.52%

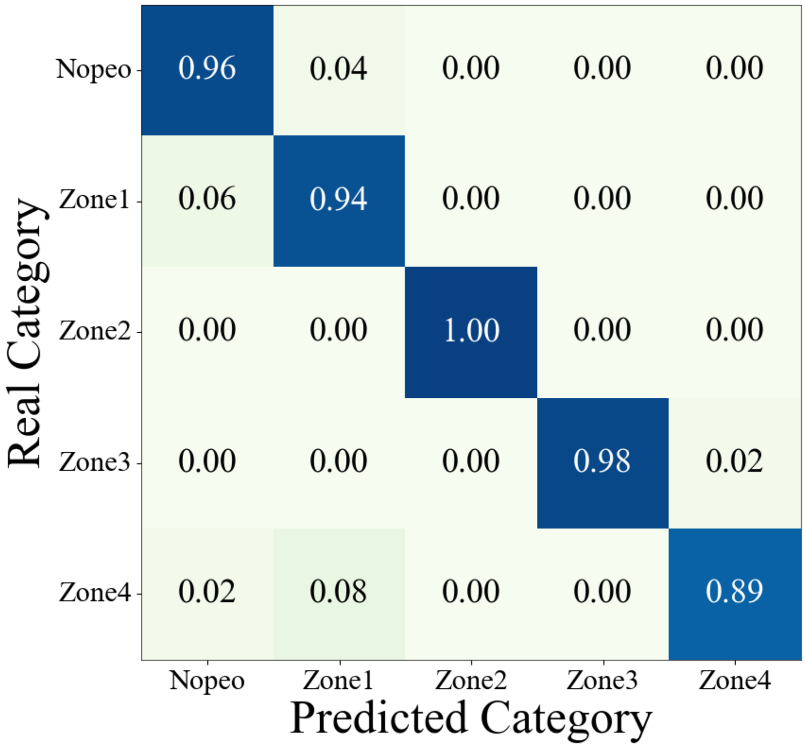

Supplementary Figure 63. The confusion matrix illustrating the horizontal localization accuracy in Space 3 (Long case) with the lens, using unnormalized data and KNN method.

The neural network is designed to learn and extract the features of the data. After setting up, the model undergoes compilation, where suitable methods are chosen to improve and assess during training. Then we will train and test the model to see how well it works. The deep-learning model was built based on the TensorFlow machine learning platform. The function of optimizer, loss and metric are separately 'Adam', 'Categorical cross-entropy' and 'Accuracy'. Eight neurons were selected as input layer, followed by two hidden layers with 64 and 32 neurons. 'ReLU' was employed as the activation function of hidden layers. 'Softmax' activation function was used in the output layer. It could be observed in Supplementary Figure 64 that the deep learning method also performs well in prediction; however, its results are not as effective as those achieved by the KNN method.

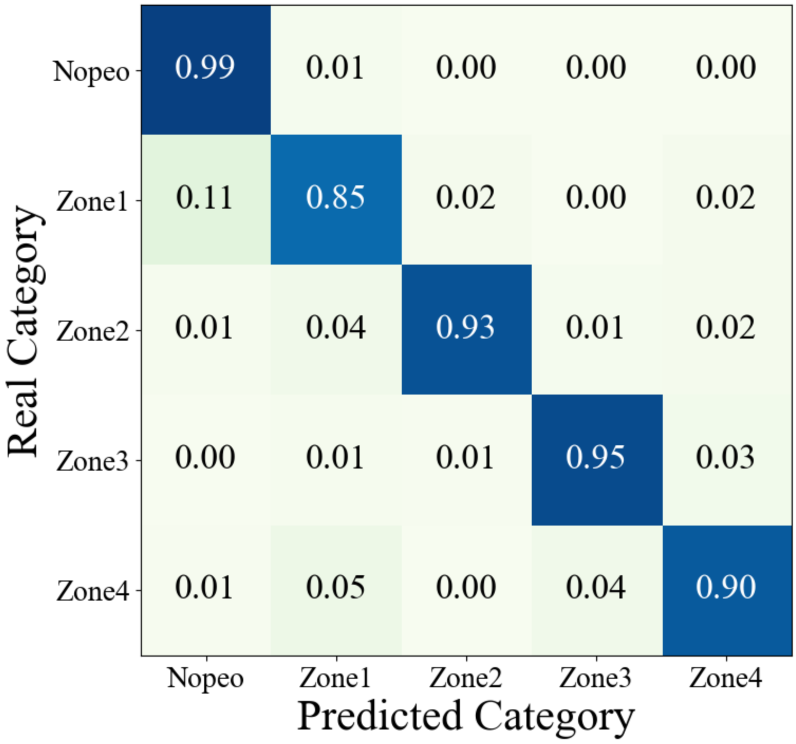

Supplementary Figure 64. The confusion matrix illustrating the horizontal localization accuracy in Space 3 (Long case) with the lens, using unnormalized data and DNN method.

As shown in Supplementary Table 6, the table lookup method demonstrates very poor performance, and the two normalization techniques provide only minimal improvement in accuracy. In contrast, the KNN method achieves the best performance across all normalization methods, with max-min normalization significantly enhancing its overall accuracy. A more comprehensive comparison table containing all horizontal localization experiments is shown in Supplementary Note 15. It could be seen that sometimes the total accuracy of KNN model is worse than DNN model. The prediction accuracy of 'Nopeo' situation is worse in most cases, which could be checked in the confusion matrices proposed in Supplementary Note 15 as well.

Supplementary Table 6. Total Accuracy Comparison of All Three Prediction Methods with Different Normalized Data.

Normalization Method	Lookup Table	KNN	DNN
Unnormalized	32.96%	95.52%	88.92%
Normalized by Steady State	33.68%	96.72%	91.60%
Max-Min Normalization	30.76%	99.2%	91.56%

Supplementary Note 15. Impact of the Lens on Accuracy and Results Summary

To verify the necessity of the lens and the machine learning model, a series of experiments and training processes were conducted to evaluate the system's performance without the lens, over varying training durations, and with smaller datasets. The detailed results of the horizontal and vertical experiments, performed without the lens, will be presented in the first subsection. The second subsection will discuss the localization results, obtained by adjusting the model parameters. The findings clearly demonstrate that both the lens and the machine learning model are crucial for achieving high accuracy in the localization system.

Supplementary Note 15.1. Comprehensive Results of Localization Experiments

To verify the importance of the lens, localization experiments were repeated without the lens in three scenarios: horizontal localization in Space 3, both for short and long cases, and vertical localization under the same conditions as the previous experiment. Additionally, various normalization methods were applied to both the training and test datasets to assess any differences in performance.

Supplementary Note 15.1.1. Horizontal Localization Results

The horizontal localization experiment was conducted across multiple spaces, using various combinations of transmitters, test subjects, receiver setups, and data processing methods. These experiments aim to demonstrate the system's robustness, and also evidencing the wide angular coverage offered by the multi-antenna lens feed.

The experiments were performed in three spaces, each featuring different linear separations between the transmitter and receiver. Three transmitter configurations were tested: single-centred transmitter, single-side transmitter, and dual-transmitter setups. The data were trained and tested using three distinct data processing methods for comparison. The first method used raw data without any normalization. The second method applied normalization based on the average values of the steady state. The third method employed max-min normalization, adjusting the data according to the maximum and minimum values. Data from eight different channels were normalized using the corresponding channel data. The specific normalization equations are shown below.

The equation of the normalization process by steady state:

$$x' = \frac{x}{x_{steady\ state}}$$

x is the original value of the data, $x_{steady-state}$ is the average value of the steady-state of training dataset.

The equation of the max-min normalization process:

$$x' = \frac{x - x_{min}}{x_{max} - x_{min}}$$

x is the original value of the data, x_{min} and x_{max} are the maximum and minimum value of the full training dataset.

Supplementary Table 7 presents the results of the horizontal localization experiments across various conditions and two prediction methods is shown below. From the table, it can be observed that the KNN model generally demonstrates superior performance in most scenarios. However, when the test subject differs, the results may decline, as illustrated in the Space 3 short case with Subject 2 as the test subject.

Supplementary Table 7. The combined accuracy of all horizontal localization experiments.

Space	**Linear Separation between TXs and RX**	**Combination of TX**	**Test Subject**	**RX Setup**	**Data Processing**	**DNN Accuracy**	**KNN Accuracy**
Space 1	8.7 m	Single Centred TX	Subject 1	With Lens	Normalized by Steady State	64.71%	66.13%
		Dual-TX				78.65%	86.12%
Space 2	4.3 m	Single Centred TX	Subject 1			94.92%	84.85%
		Single Side TX				89.56%	71.25%
		Dual-TX				94.05%	94.60%
Space 3 Short	6.9 m	Single Centred TX	Subject 1			90.31%	92.76%
		Dual-TX				89.91%	96.12%
		Single Side TX				91.70%	90.76%
				Without Lens		53.47%	64.00%
		Single Centred TX	Subject 2	With Lens		74.09%	80.80%
		Single Side TX				83.32%	75.11%
		Dual-TX				85.24%	82.98%
Space 3 Long	9.7 m	Dual-TX	Subject 1	With Lens	Normalized by Steady State	91.60%	96.72%
					Max-Min Normalization	91.56%	99.20%
					Unnormalized	88.92%	95.52%
				Without Lens	Normalized by Steady State	67.56%	72.32%
					Max-Min Normalization	80.82%	74.4%
					Unnormalized	66.20%	73.8%
			Subject 2	With Lens	Normalized by Steady State	89.03%	92.15%
			Subject 3			94.20%	94.82%

The three specific confusion matrices for horizontal localization results in Space 3 (long case) without the lens, using different data processing methods and prediction models, are shown below. The y-axis represents the true categories of the object, indicating the actual zone where the object is located. The x-axis represents the predicted categories, indicating the zone the system predicts the object to be in.

It can be observed that the worst localization results occur in the 'NoPeo' state and the 'Zone 3' state. While the max-min normalization method provides some improvement, the overall accuracy remains 10% lower compared to the results obtained with the lens.

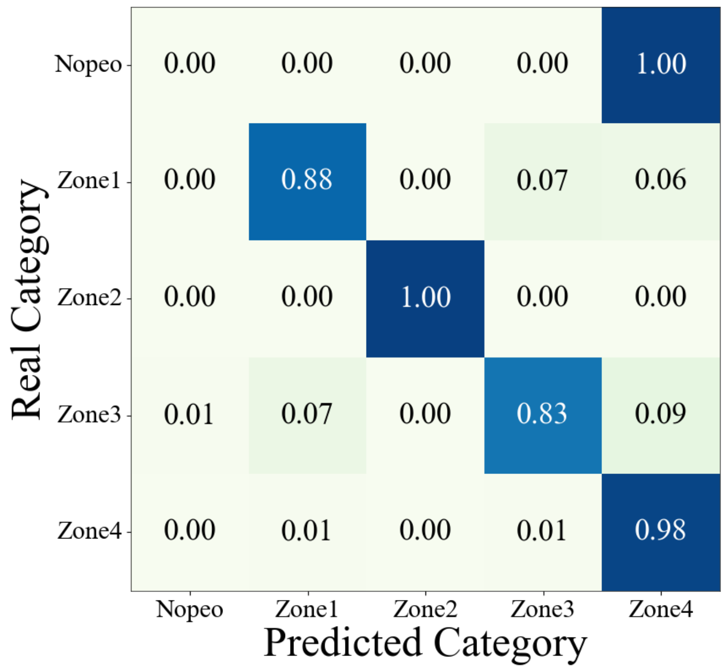

Supplementary Figure 65. The confusion matrix illustrating the horizontal localization accuracy in Space 3 (long case) without the lens, using unnormalized data.

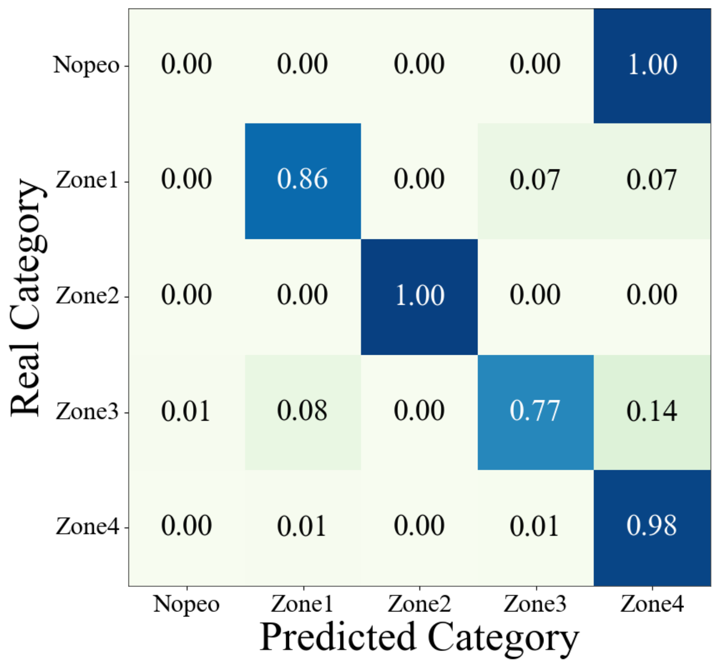

Supplementary Figure 66. The confusion matrix showing the horizontal localization accuracy in Space3 long without lens employed. (Normalized by Steady State Data)

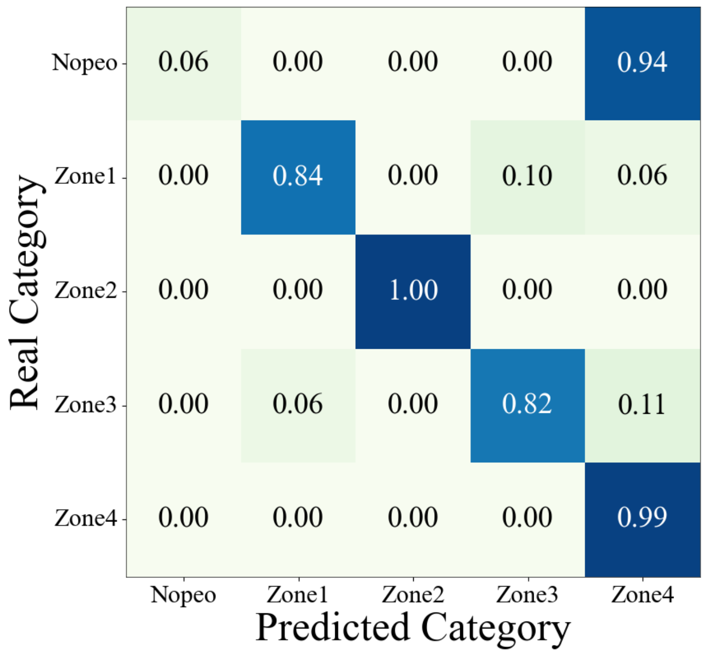

Supplementary Figure 67. The confusion matrix illustrating the horizontal localization accuracy in Space 3 (long case) without the lens, with data processed using max-min normalization

The relationship between localization accuracy and the number of rectifiers employed was also explored, as shown in Supplementary Figure 68 for both cases with and without the lens. The accuracy was obtained using unnormalized data. A clear improvement in accuracy can be observed as the number of rectifiers increases. Additionally, the difference in accuracy between the with-lens and without-lens cases becomes more pronounced as the number of rectifiers increases.

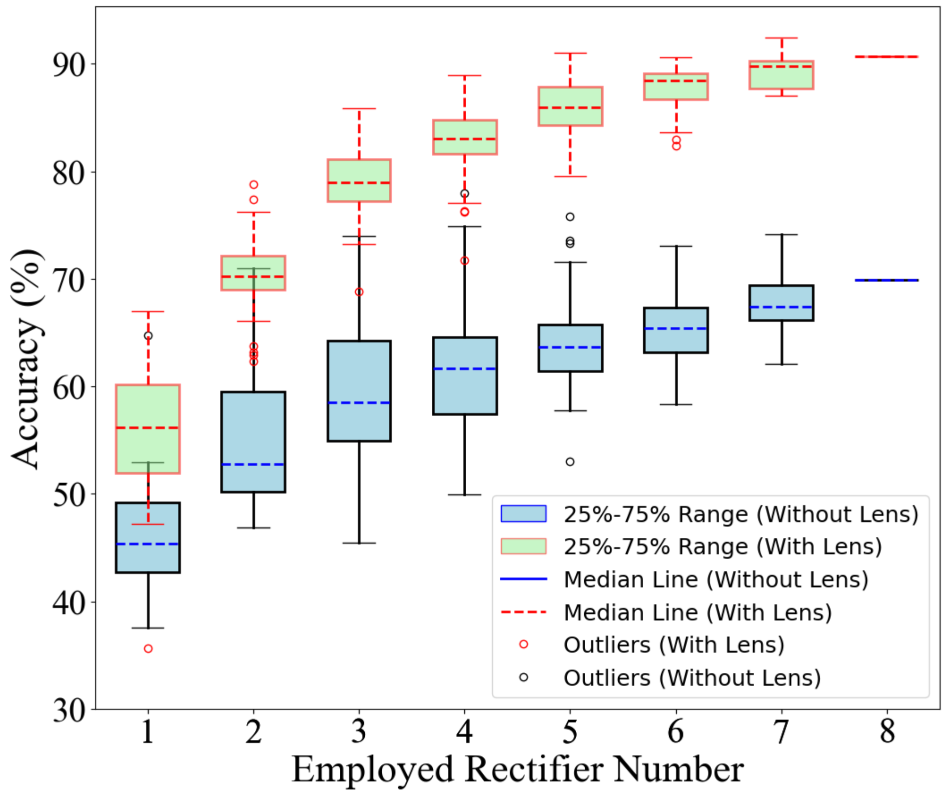

Supplementary Figure 68. The relationship between the horizontal localization accuracy predicted by DNN model in Space 3 (long case) and the number of rectennas/beams employed for both with and without lens case, using unnormalized data.

The vertical localization results with and without the lens are shown in Supplementary Table 8. It can be observed that the overall accuracy drops by approximately 10%. For vertical localization, the lens's orientation function does not apply, so the difference is likely due to the reduction in the received power level. The specific confusion matrix is shown in Supplementary Figure 69.

Supplementary Table 8. The accuracy results of the vertical localization experiments.

Localization Direction	Combination of TX	Test Subject	RX Setup	Data Processing	Accuracy
Vertical	Single TX	Subject 1	With Lens	Normalized by Steady State	95.52%
			Without Lens		85.95%

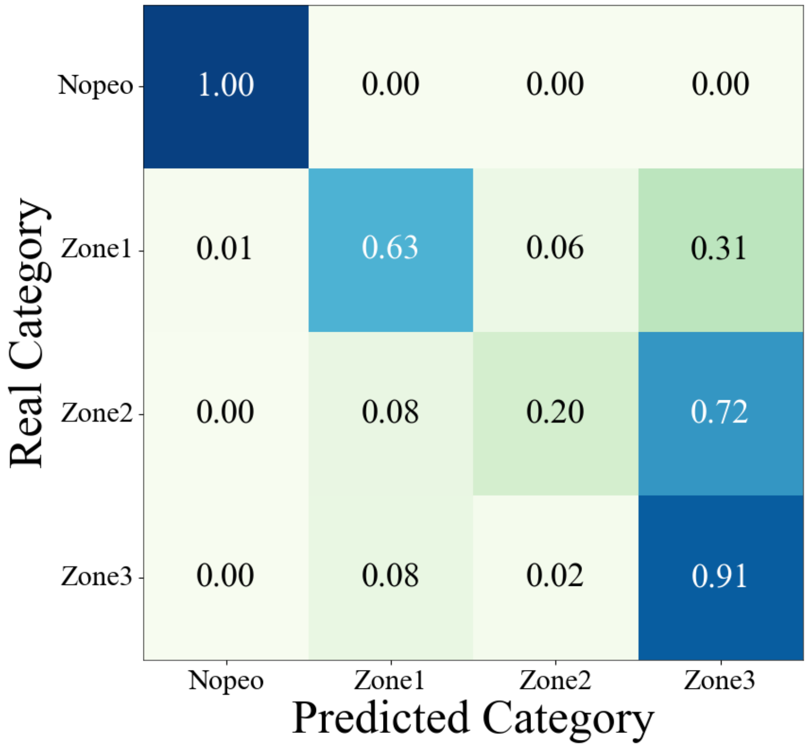

Supplementary Figure 69. The confusion matrix illustrating the vertical localization accuracy without the lens, with data normalized by steady state, predicted by KNN model.

Supplementary Note 15.2. Machine Learning Model Parameter Sweep

To verify the importance of the machine learning model, the training data size and number of epochs were varied to observe changes in accuracy and loss. The loss serves as an indicator during the training process for parameter adjustment, and when it begins to oscillate, it suggests the system may be overfitting. The tests were conducted using horizontal experiment data from Space 3 (long case) with the lens and steady-state normalization. It was observed that localization accuracy improves with both increased training data size and the number of epochs. Insufficient training time or inadequate data size results in poor system performance.

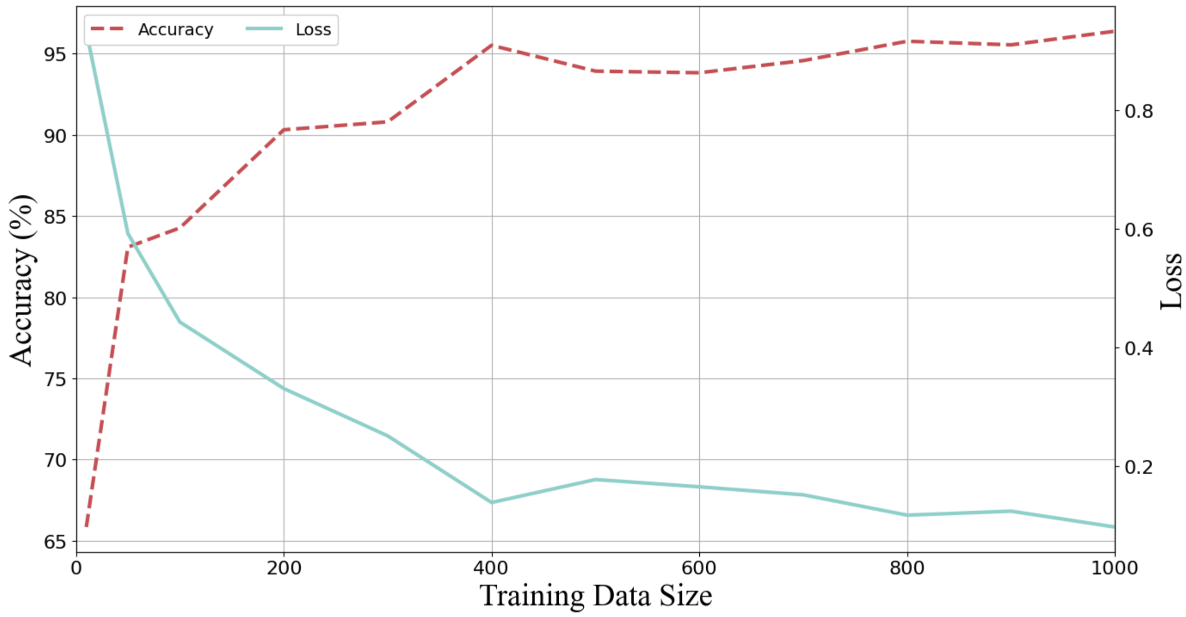

(a)

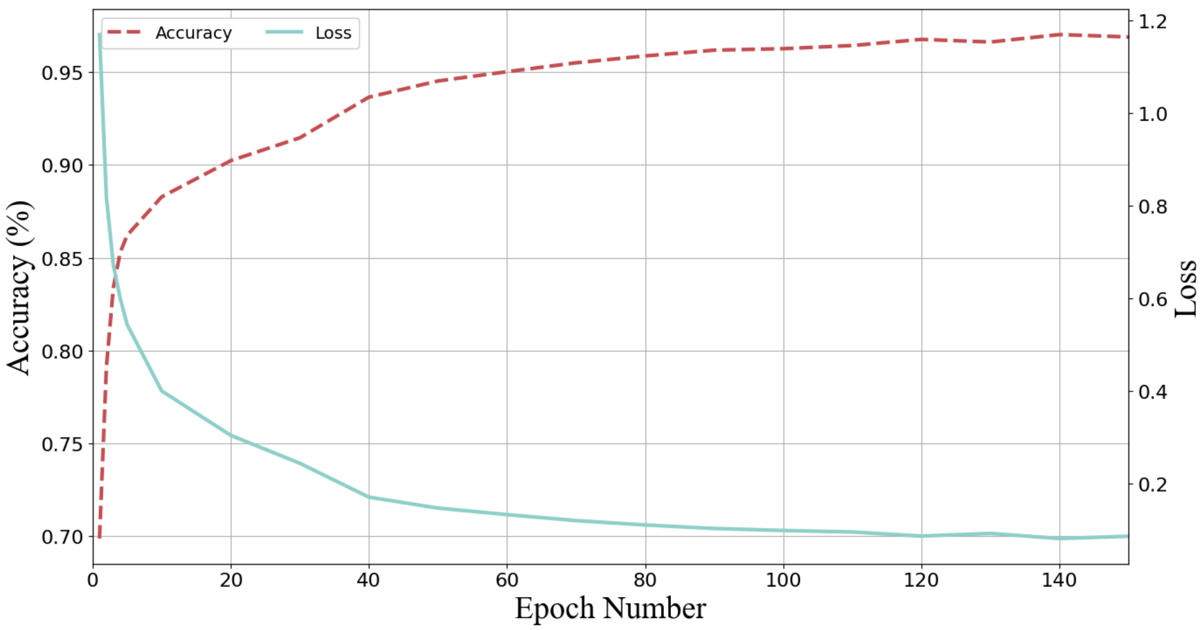

(b)

Supplementary Figure 70. The relationship between the localization accuracy and the (a) training dataset size, and the (b) epoch number.

Supplementary Note 16. Localization Results Along a Vertical Path

The vertical localization experiment was done to test the system's prediction ability of subject moving zone. The setup of the experiment is shown in Supplementary Figure 71. The area was divided into three 4×0.6 m zones, between the transmitter and the receiver. Supplementary Figure 72 shows the confusion matrix showing the accuracy with all rectifiers employed, which indicates the localization system works well with the same subject moving in the vertical space.

To find the relationship between the localization accuracy and the number of rectifiers employed, another research was done to check the essentiality of multiple rectifiers working together. With the same training and test dataset, the output voltage data with different combinations will be inputted into a same structure deep learning model. The same dataset was then used to investigate the accuracy of different rectenna beam combinations. The relationship between the number of employed rectennas/beams and classification accuracy is shown in Supplementary Figure 73. It is clearly evident that the proposed quasi-optical multi-beam system improves the localization accuracy, where an accuracy of 50% or less would be the maximum achievable limit, for single-beam system.

The specific accuracy of every separate rectifier combination can be checked in Supplementary Table 8.

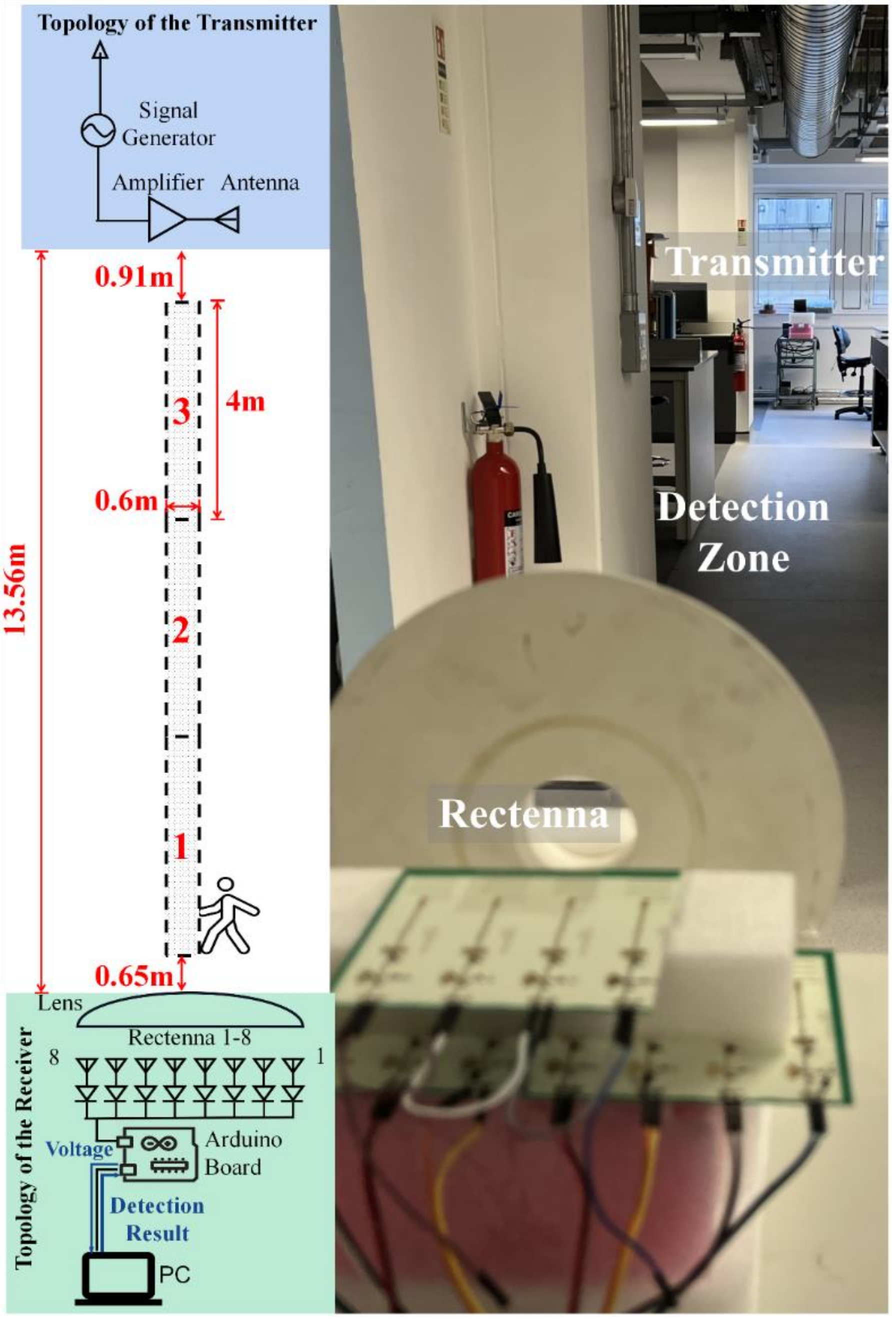

Supplementary Figure 71. The vertical localization experimental setup.

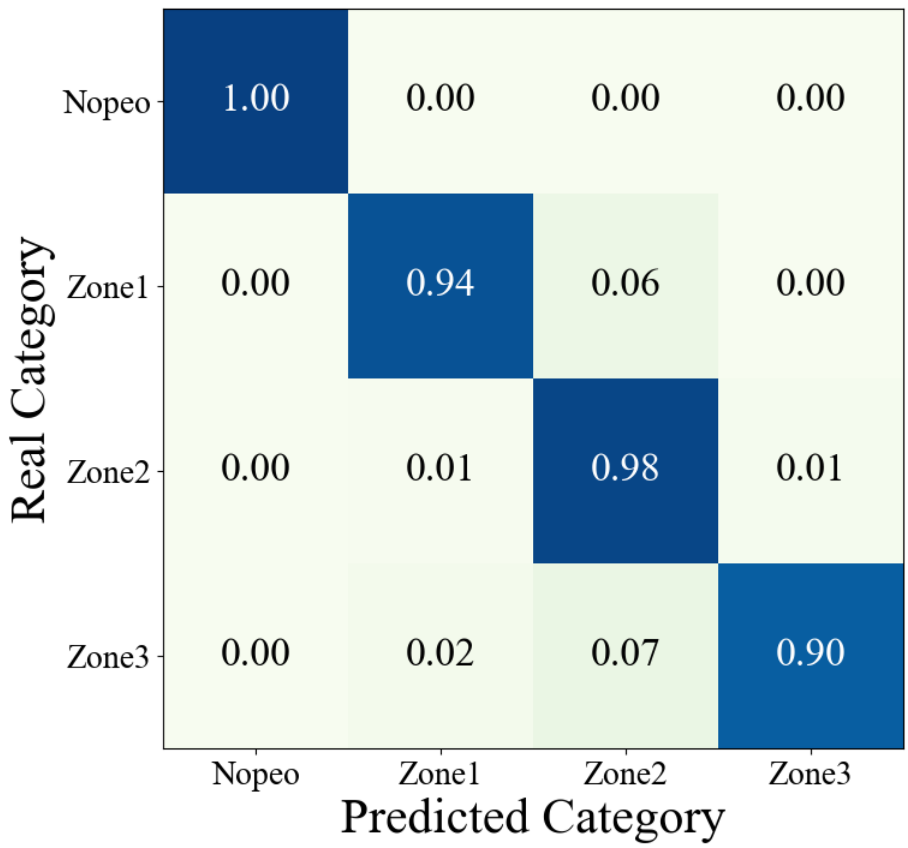

Supplementary Figure 72. The confusion matrix showing the vertical localization accuracy over 3 zones, predicted by DNN model.

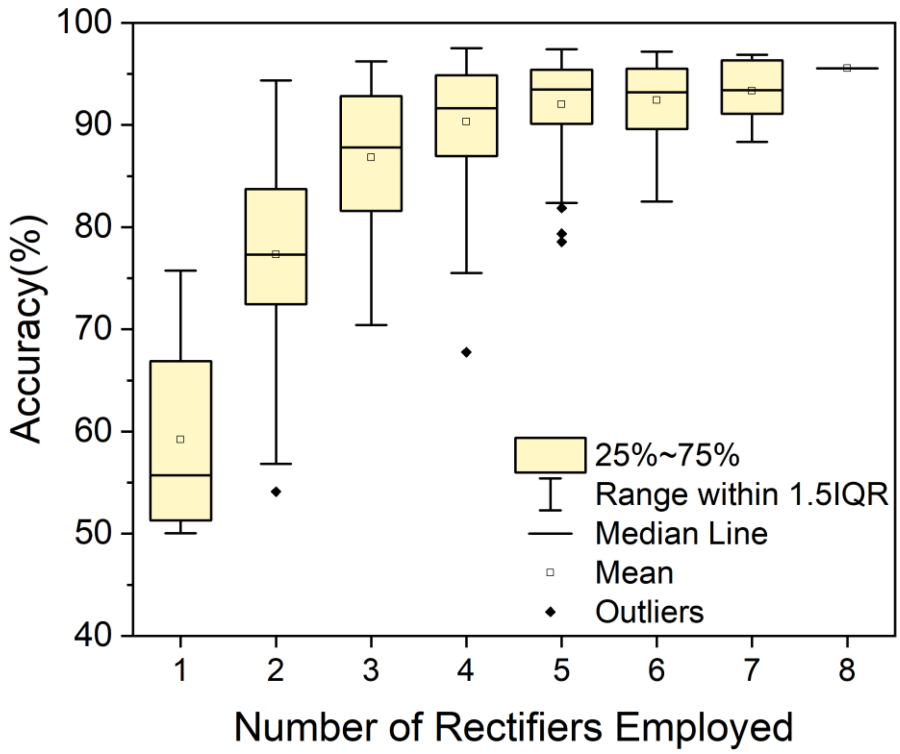

Supplementary Figure 73. The relationship between the vertical localization accuracy and the number of rectennas/beams employed, predicted by DNN model.

Supplementary Table 8. Specific accuracies for different rectifier combinations in localising a subject along a vertical space (in Supplementary Figure 71).

Rectifier	Accuracy	Rectifier	Accuracy	Rectifier	Accuracy	Rectifier	Accuracy	Rectifier	Accuracy
1;	0.7012	1;5;6;	0.9315	1;2;5;7;	0.9491	3;5;6;7;	0.8701	2;3;5;6;8;	0.864
2;	0.5121	1;5;7;	0.9133	1;2;5;8;	0.8348	3;5;6;8;	0.943	2;3;5;7;8;	0.7935
3;	0.5535	1;5;8;	0.9376	1;2;6;7;	0.9439	3;5;7;8;	0.8551	2;3;6;7;8;	0.9376
4;	0.7575	1;6;7;	0.8815	1;2;6;8;	0.936	3;6;7;8;	0.9484	2;4;5;6;7;	0.9192
5;	0.6364	1;6;8;	0.9266	1;2;7;8;	0.8907	4;5;6;7;	0.9248	2;4;5;6;8;	0.8921
6;	0.561	1;7;8;	0.8449	1;3;4;5;	0.8914	4;5;6;8;	0.9432	2;4;5;7;8;	0.914
7;	0.5136	2;3;4;	0.954	1;3;4;6;	0.9044	4;5;7;8;	0.8888	2;4;6;7;8;	0.9418
8;	0.5005	2;3;5;	0.8561	1;3;4;7;	0.9157	4;6;7;8;	0.94	2;5;6;7;8;	0.8713
1;2;	0.7645	2;3;6;	0.8049	1;3;4;8;	0.8977	5;6;7;8;	0.8437	3;4;5;6;7;	0.8598
1;3;	0.811	2;3;7;	0.7939	1;3;5;6;	0.9537	1;2;3;4;5;	0.9416	3;4;5;6;8;	0.8187
1;4;	0.8626	2;3;8;	0.7435	1;3;5;7;	0.9486	1;2;3;4;6;	0.9481	3;4;5;7;8;	0.9661
1;5;	0.8308	2;4;5;	0.7879	1;3;5;8;	0.8215	1;2;3;4;7;	0.9741	3;4;6;7;8;	0.954
1;6;	0.7811	2;4;6;	0.9028	1;3;6;7;	0.7551	1;2;3;4;8;	0.943	3;5;6;7;8;	0.9334
1;7;	0.8079	2;4;7;	0.9227	1;3;6;8;	0.9173	1;2;3;5;6;	0.9678	4;5;6;7;8;	0.9619
1;8;	0.8759	2;4;8;	0.8404	1;3;7;8;	0.8685	1;2;3;5;7;	0.9544	1;2;3;4;5;6;	0.9612
2;3;	0.7493	2;5;6;	0.9196	1;4;5;6;	0.9699	1;2;3;5;8;	0.8329	1;2;3;4;5;7;	0.9619
2;4;	0.9072	2;5;7;	0.786	1;4;5;7;	0.9647	1;2;3;6;7;	0.9339	1;2;3;4;5;8;	0.8671
2;5;	0.7652	2;5;8;	0.7645	1;4;5;8;	0.8722	1;2;3;6;8;	0.9423	1;2;3;4;6;7;	0.9129
2;6;	0.7607	2;6;7;	0.8185	1;4;6;7;	0.9318	1;2;3;7;8;	0.9329	1;2;3;4;6;8;	0.8967
2;7;	0.5685	2;6;8;	0.8346	1;4;6;8;	0.9572	1;2;4;5;6;	0.8998	1;2;3;4;7;8;	0.9301
2;8;	0.746	2;7;8;	0.7182	1;4;7;8;	0.9619	1;2;4;5;7;	0.9692	1;2;3;5;6;7;	0.9593
3;4;	0.9437	3;4;5;	0.9227	1;5;6;7;	0.975	1;2;4;5;8;	0.9514	1;2;3;5;6;8;	0.9512
3;5;	0.7561	3;4;6;	0.8981	1;5;6;8;	0.9563	1;2;4;6;7;	0.9624	1;2;3;5;7;8;	0.8699
3;6;	0.7871	3;4;7;	0.9446	1;5;7;8;	0.91	1;2;4;6;8;	0.9579	1;2;3;6;7;8;	0.9386
3;7;	0.6285	3;4;8;	0.9189	1;6;7;8;	0.9388	1;2;4;7;8;	0.9607	1;2;4;5;6;7;	0.9668
3;8;	0.7439	3;5;6;	0.9575	2;3;4;5;	0.8364	1;2;5;6;7;	0.9673	1;2;4;5;6;8;	0.9689
4;5;	0.8278	3;5;7;	0.7042	2;3;4;6;	0.9519	1;2;5;6;8;	0.9486	1;2;4;5;7;8;	0.946
4;6;	0.8437	3;5;8;	0.7206	2;3;4;7;	0.9661	1;2;5;7;8;	0.9451	1;2;4;6;7;8;	0.9717
4;7;	0.8988	3;6;7;	0.8668	2;3;4;8;	0.8799	1;2;6;7;8;	0.9692	1;2;5;6;7;8;	0.9512
4;8;	0.9012	3;6;8;	0.957	2;3;5;6;	0.9005	1;3;4;5;6;	0.9061	1;3;4;5;6;7;	0.8951
5;6;	0.8182	3;7;8;	0.7605	2;3;5;7;	0.8016	1;3;4;5;7;	0.9192	1;3;4;5;6;8;	0.8914
5;7;	0.6748	4;5;6;	0.9301	2;3;5;8;	0.6776	1;3;4;5;8;	0.7855	1;3;4;5;7;8;	0.9315
5;8;	0.5411	4;5;7;	0.961	2;3;6;7;	0.9369	1;3;4;6;7;	0.9051	1;3;4;6;7;8;	0.825
6;7;	0.6762	4;5;8;	0.8117	2;3;6;8;	0.9449	1;3;4;6;8;	0.8734	1;3;5;6;7;8;	0.9386
6;8;	0.6687	4;6;7;	0.8748	2;3;7;8;	0.9329	1;3;4;7;8;	0.9362	1;4;5;6;7;8;	0.9696
7;8;	0.7049	4;6;8;	0.9009	2;4;5;6;	0.8297	1;3;5;6;7;	0.8914	2;3;4;5;6;7;	0.9121
1;2;3;	0.9621	4;7;8;	0.918	2;4;5;7;	0.8694	1;3;5;6;8;	0.9306	2;3;4;5;6;8;	0.9014
1;2;4;	0.954	5;6;7;	0.9012	2;4;5;8;	0.7804	1;3;5;7;8;	0.9355	2;3;4;5;7;8;	0.8902
1;2;5;	0.8451	5;6;8;	0.7862	2;4;6;7;	0.9012	1;3;6;7;8;	0.8238	2;3;4;6;7;8;	0.9498
1;2;6;	0.8671	5;7;8;	0.7633	2;4;6;8;	0.9098	1;4;5;6;7;	0.9582	2;3;5;6;7;8;	0.8991
1;2;7;	0.8418	6;7;8;	0.8131	2;4;7;8;	0.9493	1;4;5;6;8;	0.9512	2;4;5;6;7;8;	0.9325
1;2;8;	0.8575	1;2;3;4;	0.9007	2;5;6;7;	0.8584	1;4;5;7;8;	0.972	3;4;5;6;7;8;	0.8848
1;3;4;	0.8657	1;2;3;5;	0.911	2;5;6;8;	0.8626	1;4;6;7;8;	0.9196	1;2;3;4;5;6;7;	0.9687
1;3;5;	0.9353	1;2;3;6;	0.935	2;5;7;8;	0.8131	1;5;6;7;8;	0.968	1;2;3;4;5;6;8;	0.9159
1;3;6;	0.8371	1;2;3;7;	0.9659	2;6;7;8;	0.7883	2;3;4;5;6;	0.9026	1;2;3;4;5;7;8;	0.8836
1;3;7;	0.8857	1;2;3;8;	0.9105	3;4;5;6;	0.8367	2;3;4;5;7;	0.9133	1;2;3;4;6;7;8;	0.9603
1;3;8;	0.8967	1;2;4;5;	0.8708	3;4;5;7;	0.9593	2;3;4;5;8;	0.8292	1;2;3;5;6;7;8;	0.9444
1;4;5;	0.8486	1;2;4;6;	0.9666	3;4;5;8;	0.8565	2;3;4;6;7;	0.9404	1;2;4;5;6;7;8;	0.9659
1;4;6;	0.9346	1;2;4;7;	0.9741	3;4;6;7;	0.9236	2;3;4;6;8;	0.9266	1;3;4;5;6;7;8;	0.9058
1;4;7;	0.9561	1;2;4;8;	0.9315	3;4;6;8;	0.9465	2;3;4;7;8;	0.9196	2;3;4;5;6;7;8;	0.9236
1;4;8;	0.9397	1;2;5;6;	0.96	3;4;7;8;	0.9621	2;3;5;6;7;	0.8834	1;2;3;4;5;6;7;8;	0.9556

Supplementary Note 17. Horizontal Localization

Note 17.1 Experiment in Space 1

The setup of horizontal localization experiment in Space 1 is shown in Supplementary Figure 74. Experiments with two kinds of TX combinations were done in this space. The confusion matrices showing the localization accuracy of Subject 1 can be found in Supplementary Figure 75-77. It can be seen that in the dual-TX case, the misdetection mainly happens in Zone 2 and Zone 3, which comes from the insufficient cover of electromagnetic wave. When TX1 is placed centred, only Zone 2 and Zone 3 can be covered well, which cause the obvious deduction of localization accuracies in another two zones.

For the experiment with dual transmitters setup, both results predicted by KNN and DNN model were proposed. It could be seen that though the total accuracy of the KNN model result is better, the detection of 'Nopeo' situation is highly lower compared with the DNN model result.

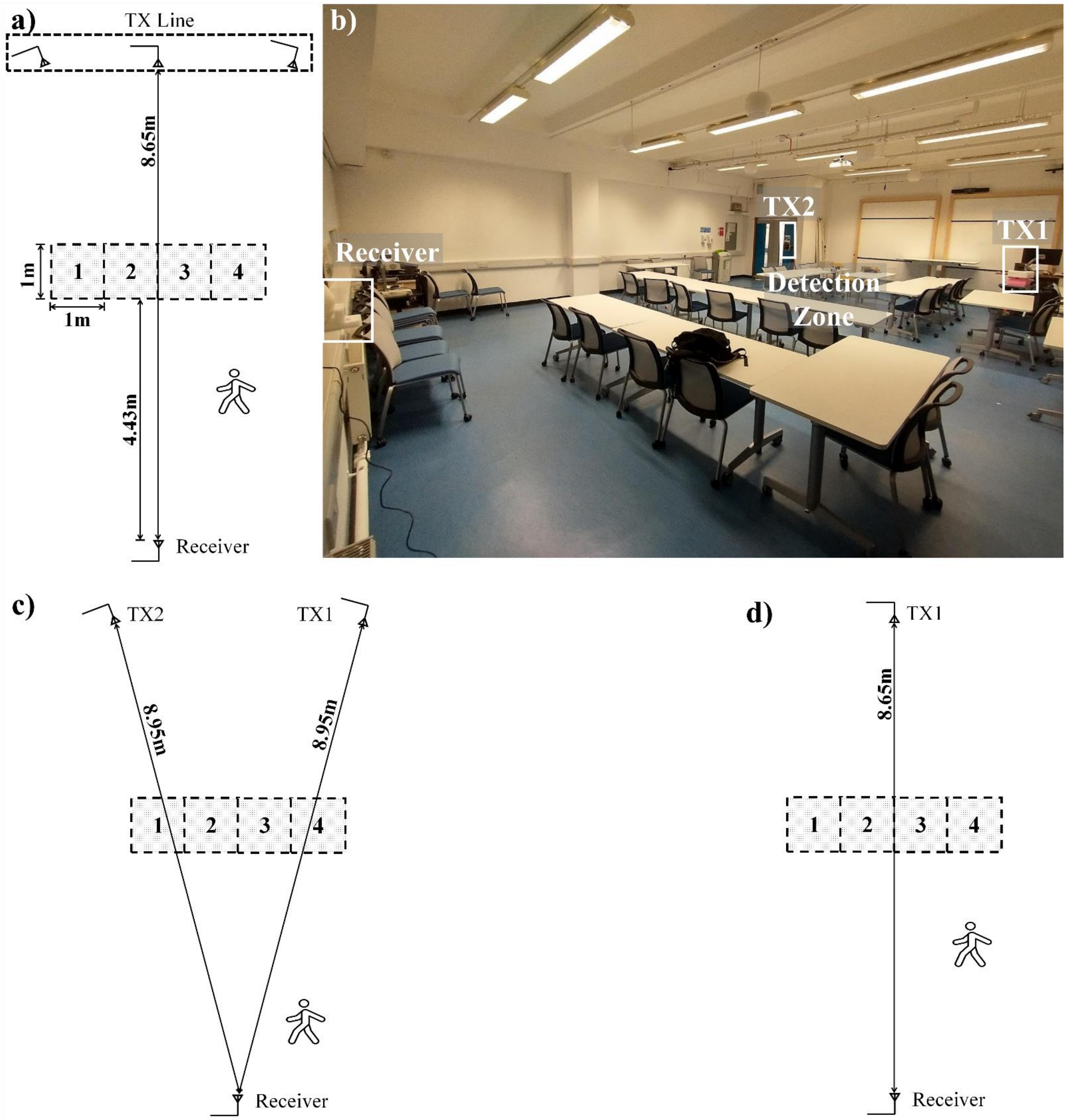

Supplementary Figure 74. The setup of horizontal localization experiment in Space 1. a) The topology of the setups; b) The actual experiment environment; c) The topology with dual-TX combination; d) The topology with single centred TX.

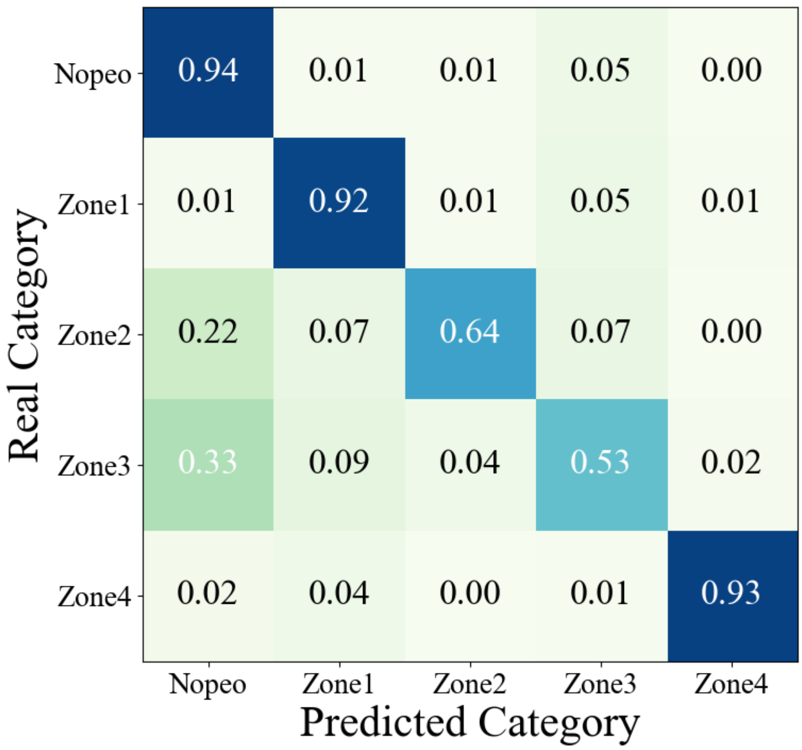

Supplementary Figure 75. The confusion matrix showing the horizontal localization accuracy of Subject 1 with Dual-TX combination in Space 1, predicted by DNN model.

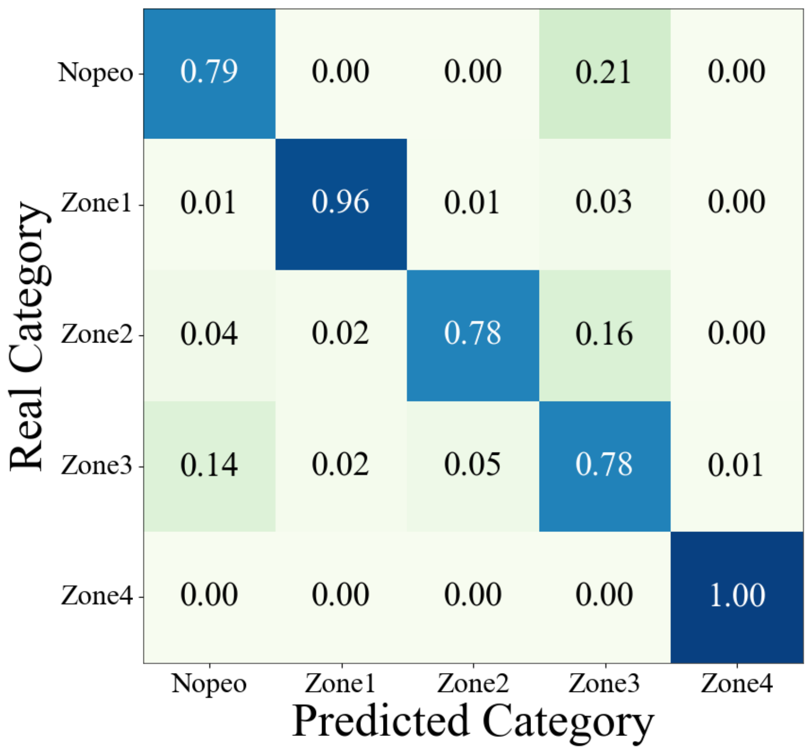

Supplementary Figure 76. The confusion matrix showing the horizontal localization accuracy of Subject 1 with Dual-TX combination in Space 1, predicted by KNN model.

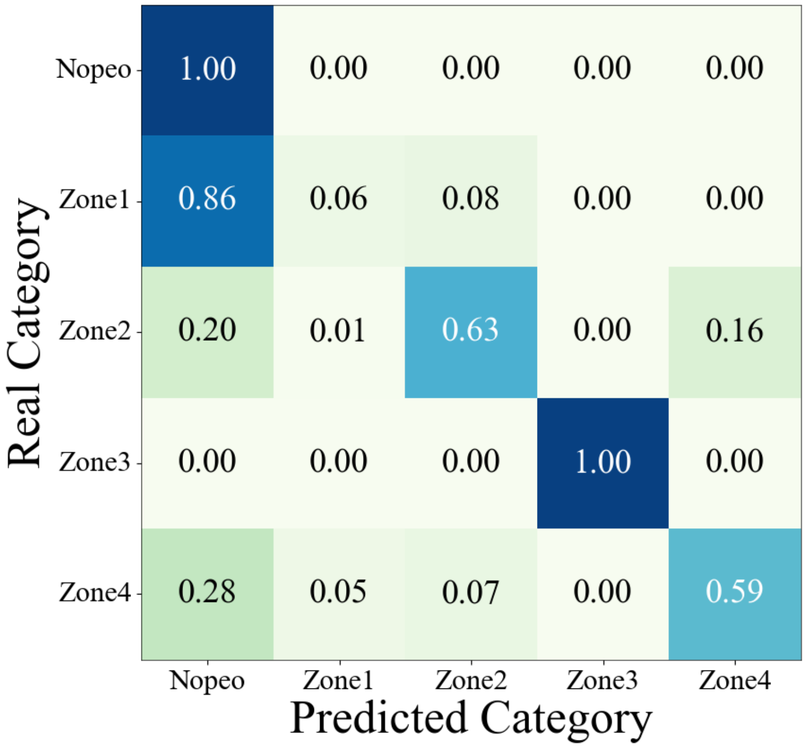

Supplementary Figure 77. The confusion matrix showing the horizontal localization accuracy of Subject 1 with single centred TX in Space 1, predicted by KNN model.

Note 17.2 Experiments in Space 2

The setup for horizontal localization experiment in Space 2 is shown in Supplementary Figure 78. Experiments with three kinds of TX combinations were done in this space. The confusion matrices showing the localization accuracy of Subject 1 can be found in Supplementary Figure 79-82.

The results clearly indicate that dual-TX combination improves the performance of the detection system. Compared to single sided TX case, the single centred TX case show an improved accuracy among most zones. This is attributed to the rich multi-path environment seen in Supplementary Figure 78(b), where the multi-paths are captured by the rectennas focused on the off-centre direction.

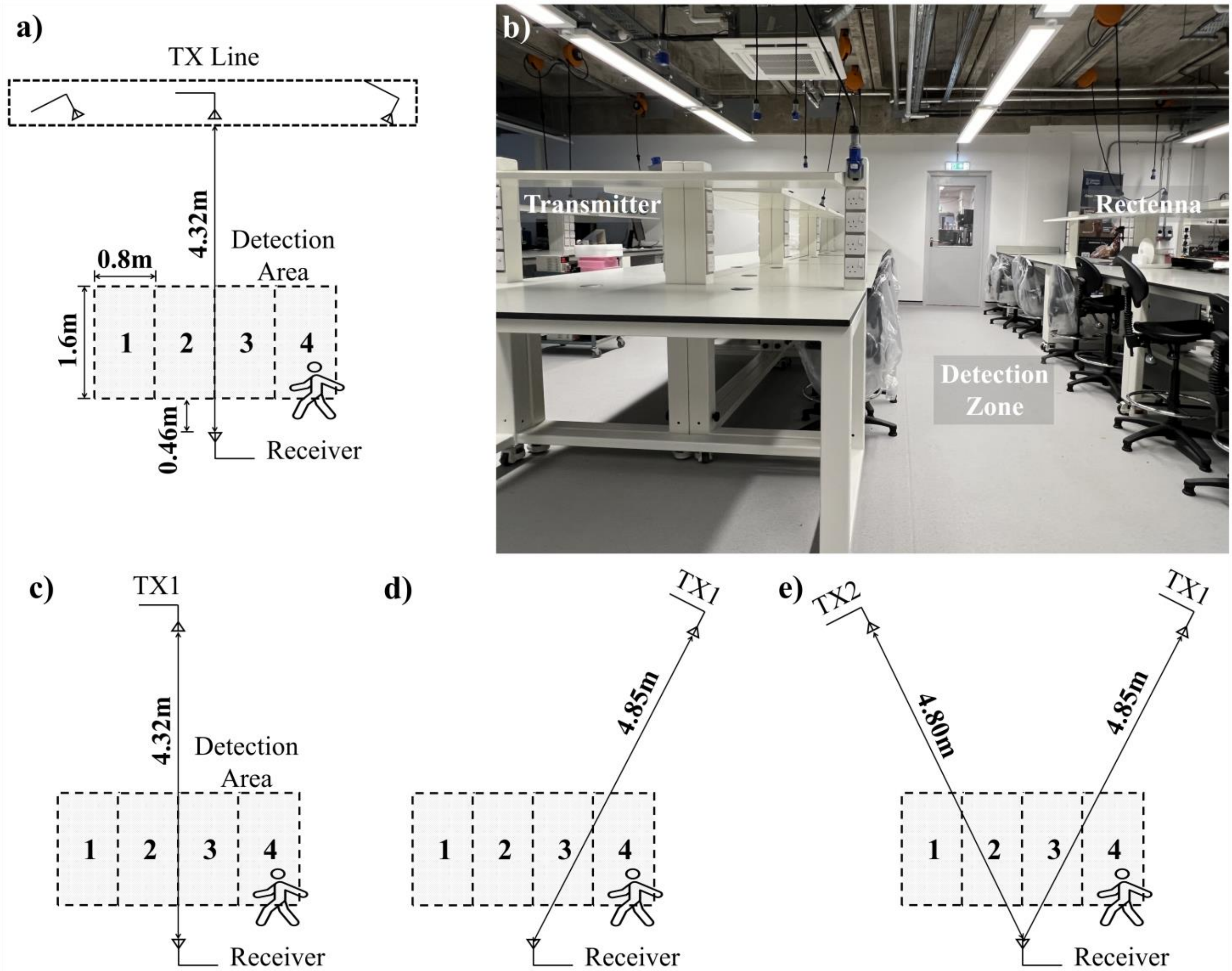

Supplementary Figure 78. The setup of horizontal localization experiment in Space 2. (a) The topology of the setups; (b) photograph of the experimental environment; (c) the setup with a single centred TX; (d) the setup with single side TX; (e) the setup with dual TX combination.

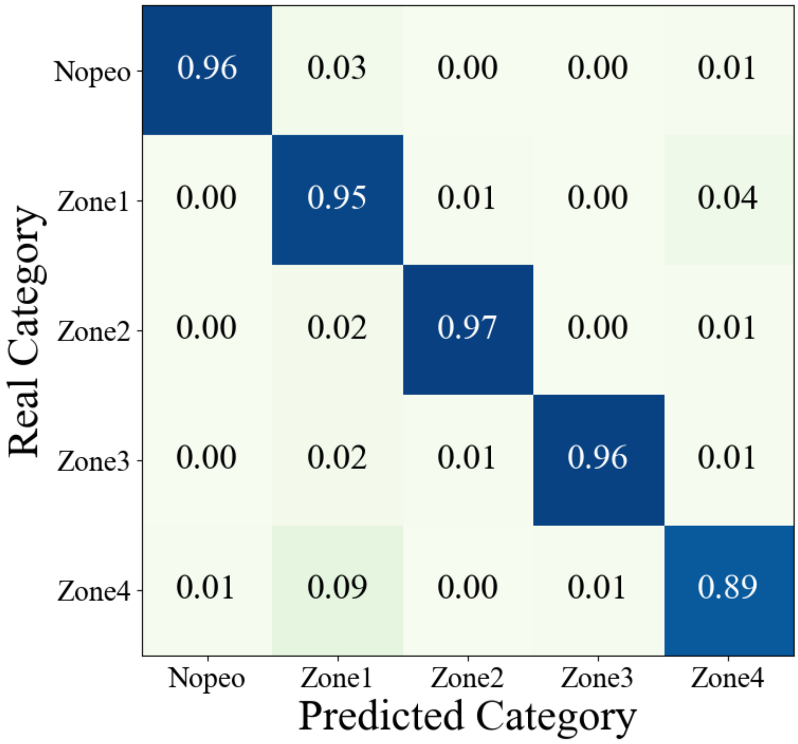

Supplementary Figure 79. The confusion matrix showing the horizontal localization accuracy of Subject 1 with single centred TX in Space 2, predicted by DNN model.

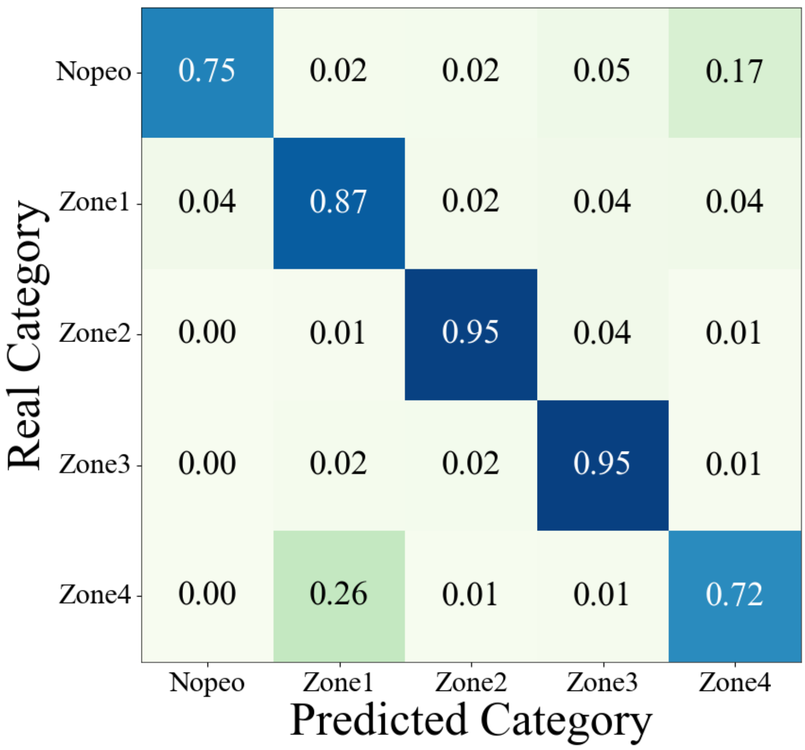

Supplementary Figure 80. The confusion matrix showing the horizontal localization accuracy of Subject 1 with single centred TX in Space 2, predicted by KNN model.

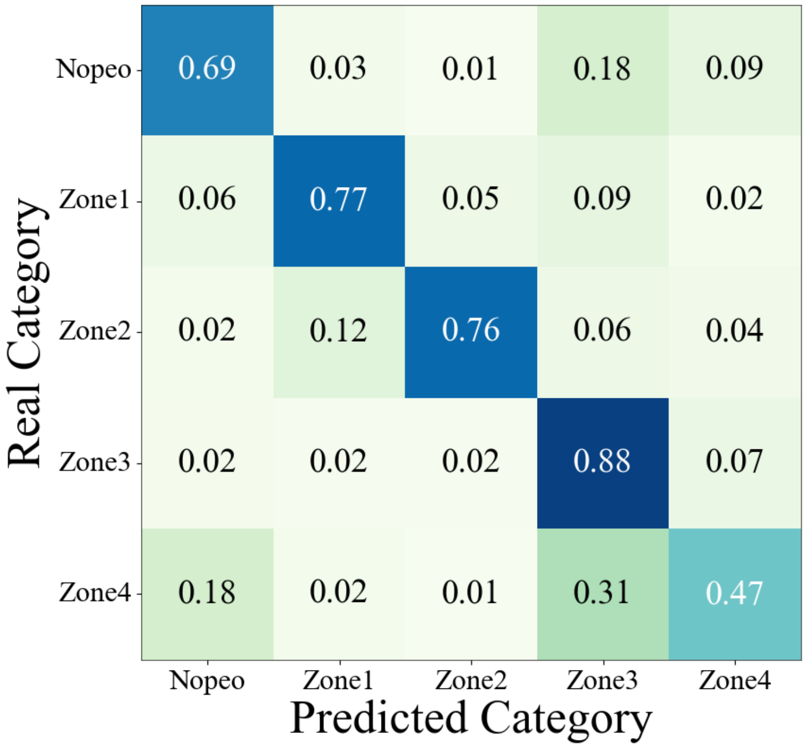

Supplementary Figure 81. The confusion matrix showing the horizontal localization accuracy of Subject 1 with single side TX in Space 2, predicted by KNN model.

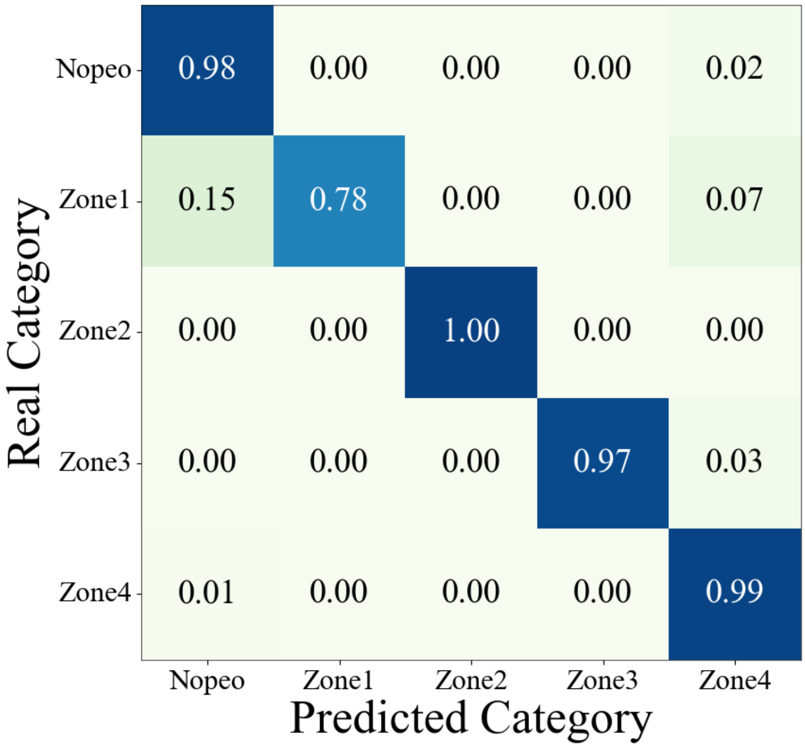

Supplementary Figure 82. The confusion matrix showing the horizontal localization accuracy of Subject 1 with dual-TX combination in Space 2.

Supplementary Note 17.3. Experiments in Space 3

To explore the effect of the distance between the transmitter and the receiver, two horizontal localization experiments were done in Space 3, with 6.9 m and 9.7 m distances. The setups of these experiments are shown in Supplementary Figure 83. Three kinds of TX combinations were done in the short-distance case with two subjects employed. The dual-TX combination was repeated in the long-distance case with three subjects employed.

Three test subjects were involved in this test, while a training dataset from a single subject was collected. The confusion matrices showing the localization accuracies of Subject 2 can be found in Supplementary Figure 84-89. The training data employed was gathered by Subject 1 and the test data was gathered by Subject 2. From the result it could be seen that the robustness of the KNN model is worse than DNN model. When the subject changes, the KNN model could not keep its advancement compared with DNN model.

The comparison of the localization accuracies is shown in Supplementary Figure 90, which indicates that the dual-TX case works better in all tested scenarios. This is particularly noticeable in the case where a different subject, to the training data, was being localised.

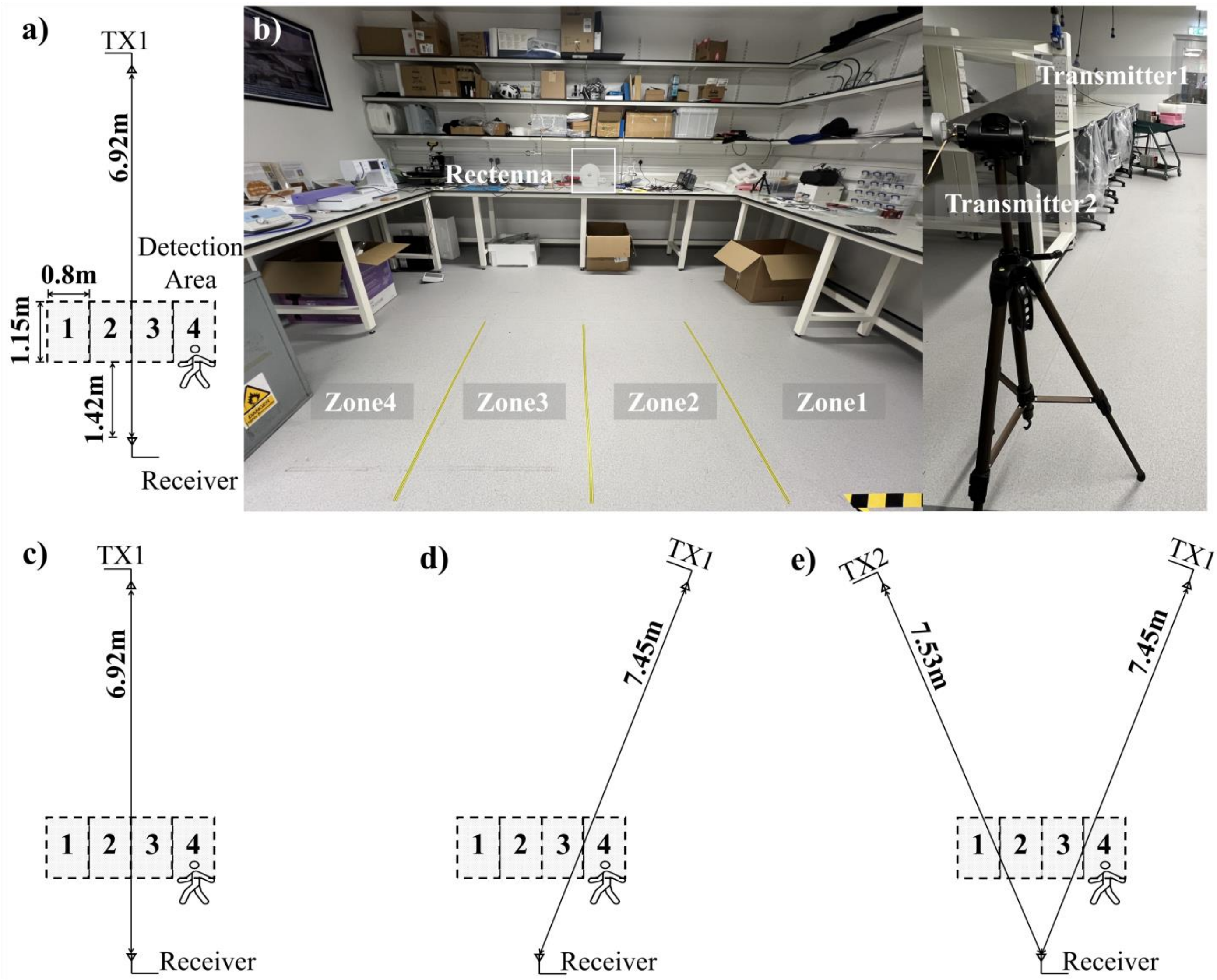

Supplementary Figure 83. The setup of horizontal localization experiment in Space 3 with 6.9 m distance between the transmitter and the receiver. a) The topology of the setups; b) The actual experiment environment; c) The topology with single centred TX; d) The topology with single side TX; e) The topology with dual TX combination.

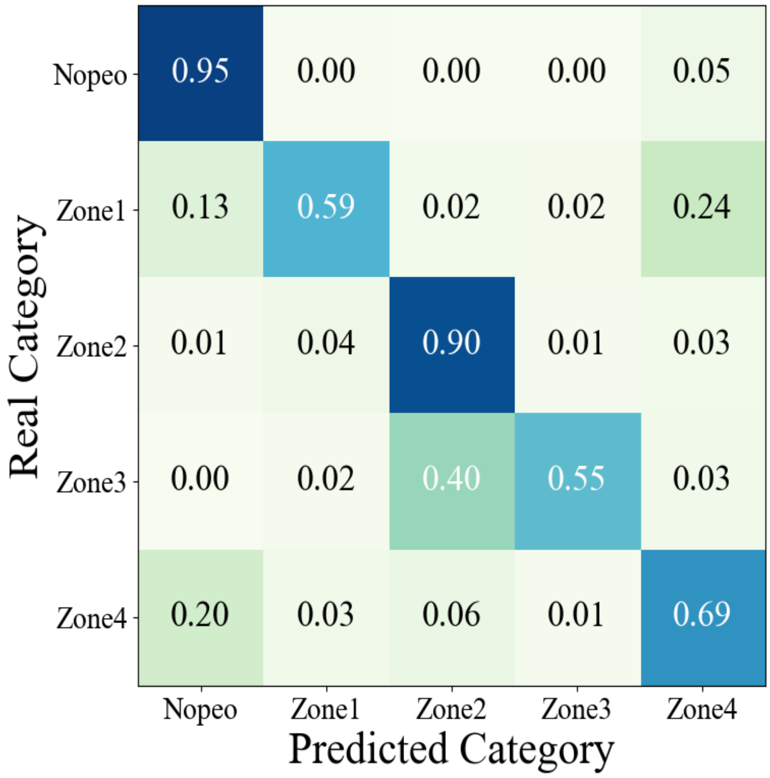

Supplementary Figure 84. The confusion matrix showing the horizontal localization accuracy of Subject 2, with single centred TX in Space3 with 6.9 m distance between the transmitter and the receiver, predicted by DNN model .

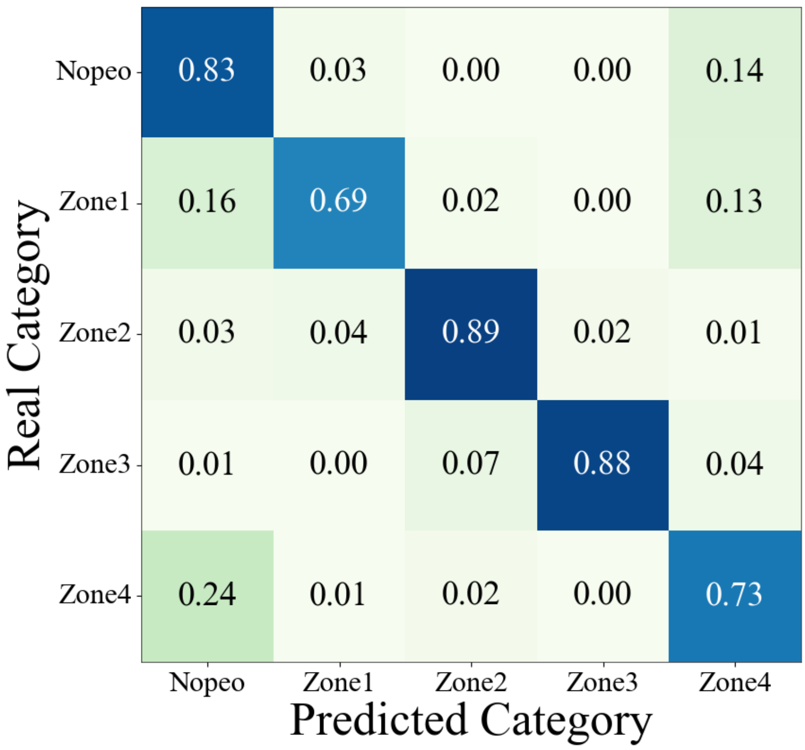

Supplementary Figure 85. The confusion matrix showing the horizontal localization accuracy of Subject 2, with single centred TX in Space3 with 6.9 m distance between the transmitter and the receiver, predicted by KNN model.

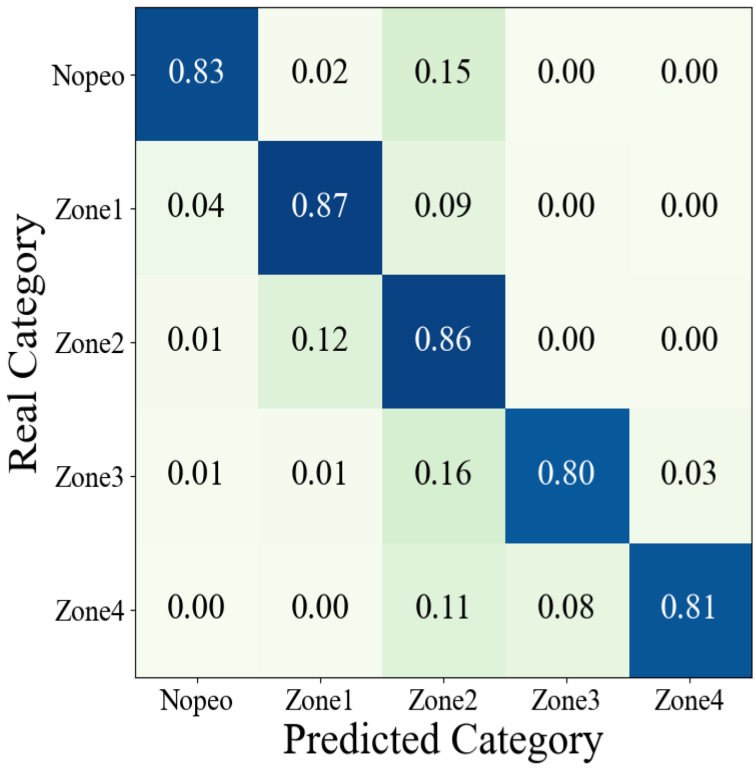

Supplementary Figure 86. The confusion matrix showing the horizontal localization accuracy of Subject 2 with single side TX in Space3 with 6.9 m distance between the transmitter and the receiver, predicted by DNN model.

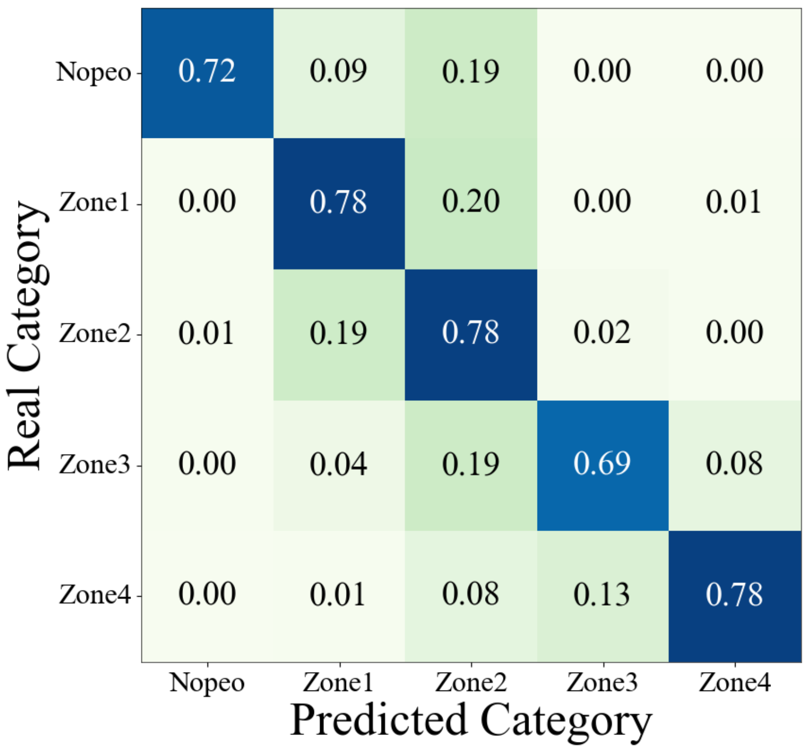

Supplementary Figure 87. The confusion matrix showing the horizontal localization accuracy of Subject 2 with single side TX in Space3 with 6.9 m distance between the transmitter and the receiver, predicted by KNN model.

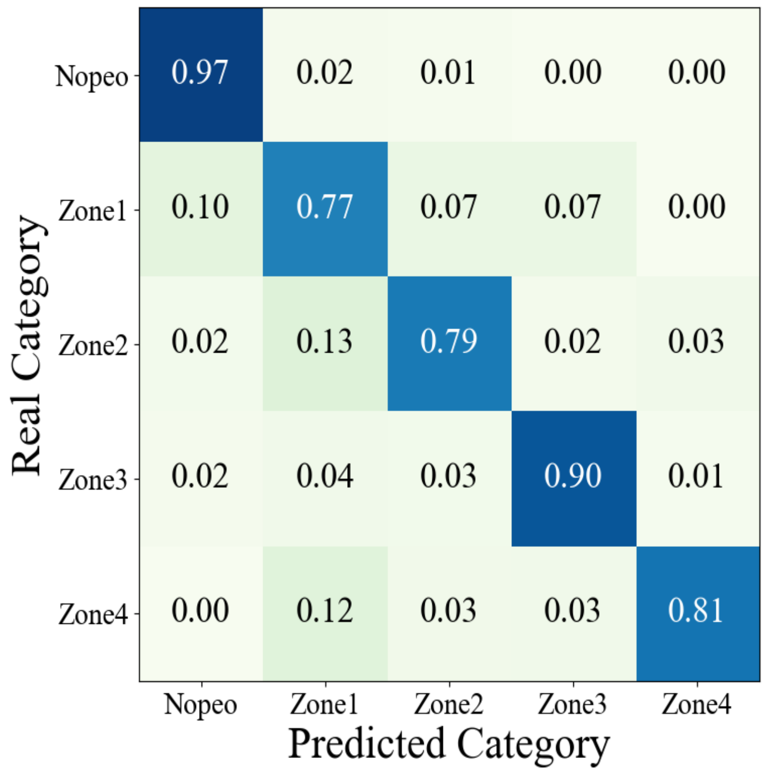

Supplementary Figure 88. The confusion matrix showing the horizontal localization accuracy of Subject 2 with dual-TX combination in Space 3 with 6.9 m distance between the transmitter and the receiver, predicted by DNN model.

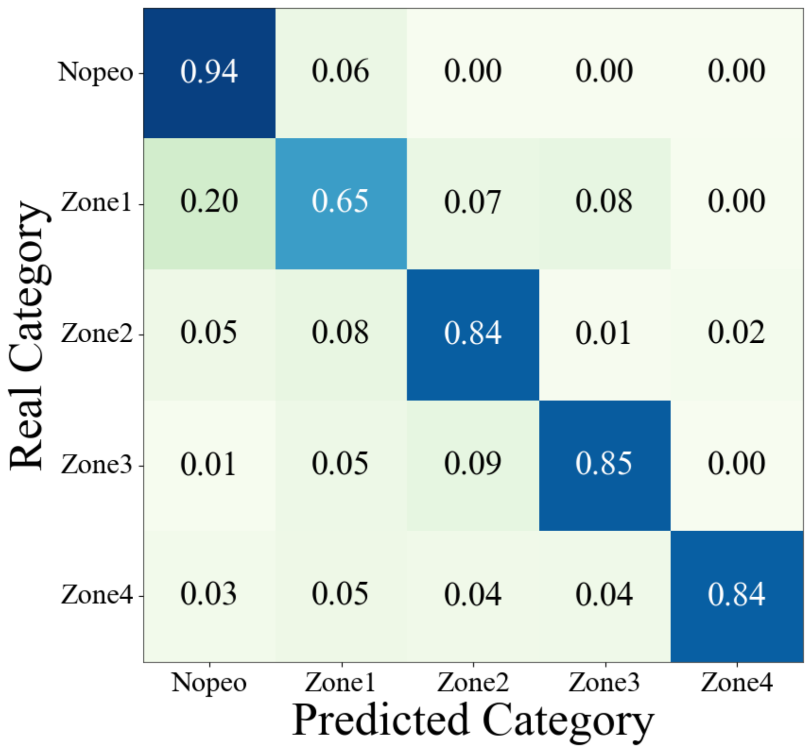

Supplementary Figure 89. The confusion matrix showing the horizontal localization accuracy of Subject 2 with dual-TX combination in Space 3 with 6.9 m distance between the transmitter and the receiver, predicted by KNN model.

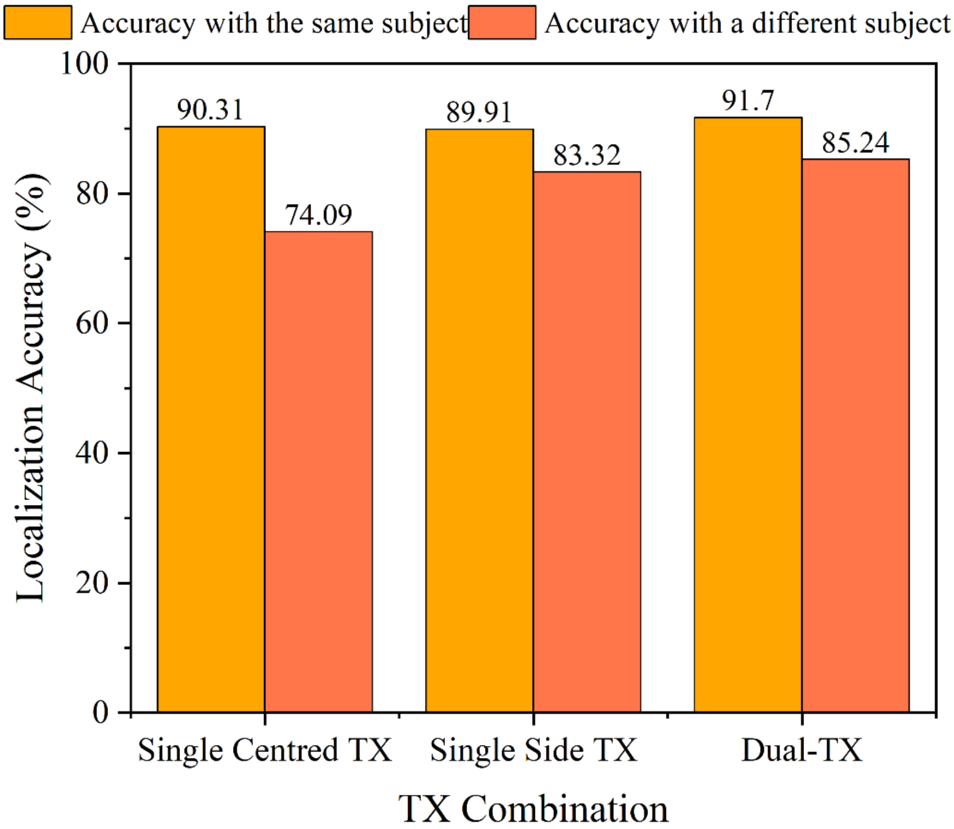

Supplementary Figure 90. The localization accuracies for different TX combinations with different subjects (i.e. between the training and classification data) in Space 3 with 6.9 m distance between the transmitter and the receiver.

Long-Range Horizontal Localization:

The setup of horizontal localization experiment with long distance is shown in Supplementary Figure 91. The transmitters were placed further with the receiver in its original place. The combined confusion matrix is shown in Supplementary Figure 92, which contains the localization results of all three subjects employed, demonstrating the robustness of the system. Compared to the experiment in Space 1, the rich multi-path environment introduces additional reflections improving the accuracy of the system, despite being over the same distance.

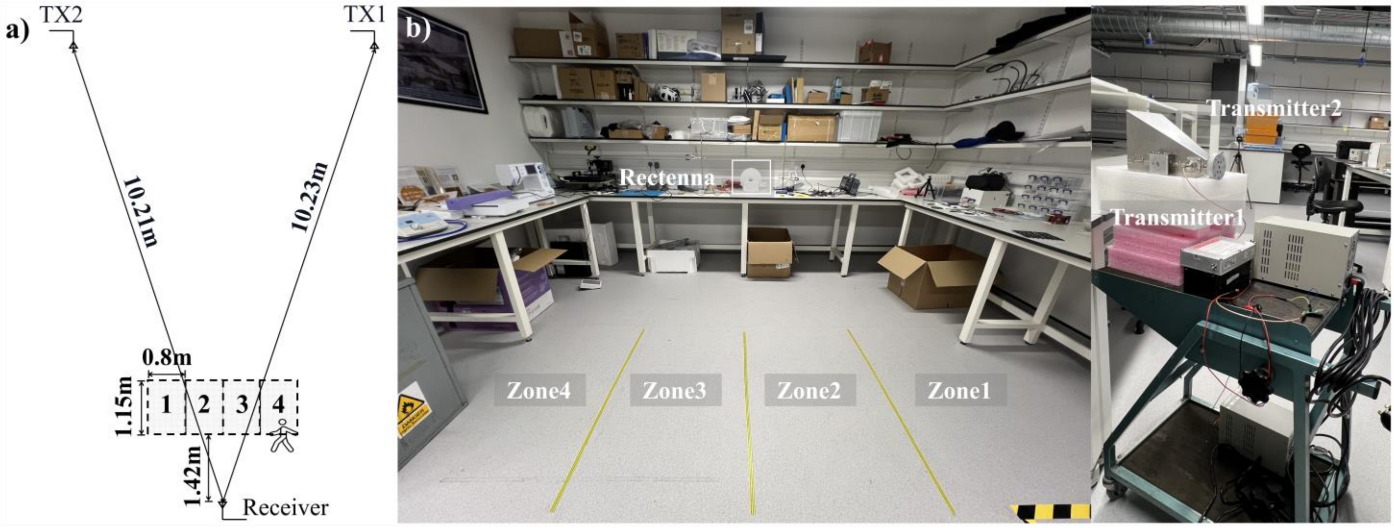

Supplementary Figure 91. The setup of horizontal localization experiment in Space 3 with 9.7 m distance between the transmitter and the receiver. A) The layout of the setups; b) The actual experiment environment.

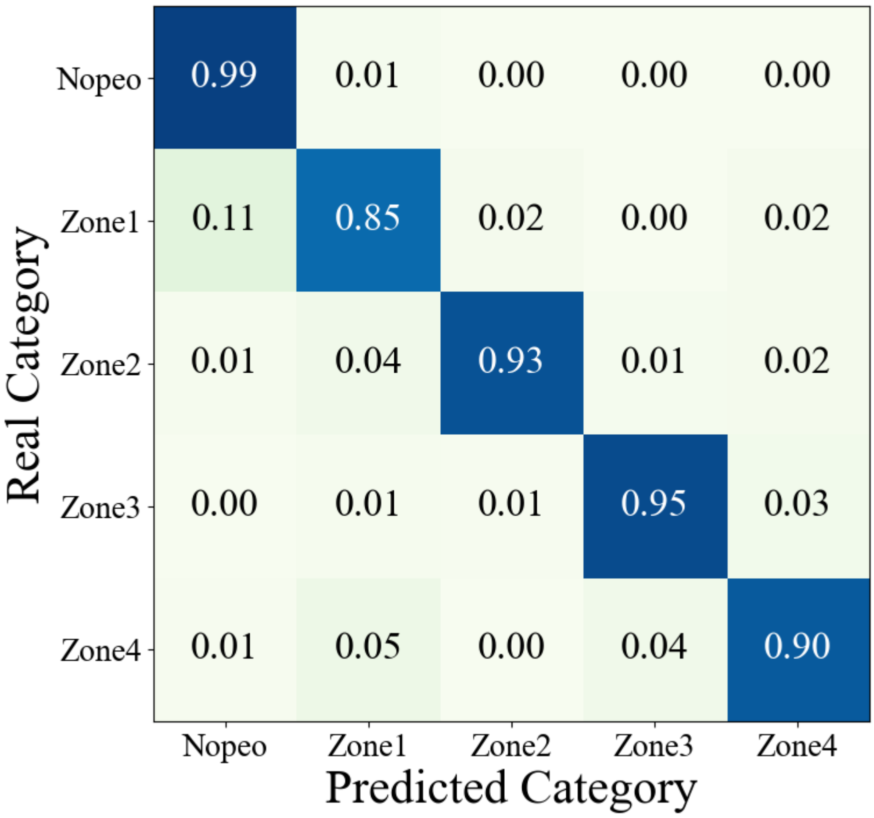

Supplementary Figure 92. The confusion matrix showing the combined horizontal localization accuracy of all three subjects with dual-TX combination in Space 3 with 6.9 m distance between the transmitter and the receiver, predicted by DNN model.

The relationship between the localization accuracy and the number of rectifiers employed was also explored, which is shown in Supplementary Figure 93. The accuracies were generated with data from all three subjects and an obvious positive relation between the accuracy and the rectifier number can be found. The specific accuracies for different rectifier combinations can be found in Supplementary Table 9.

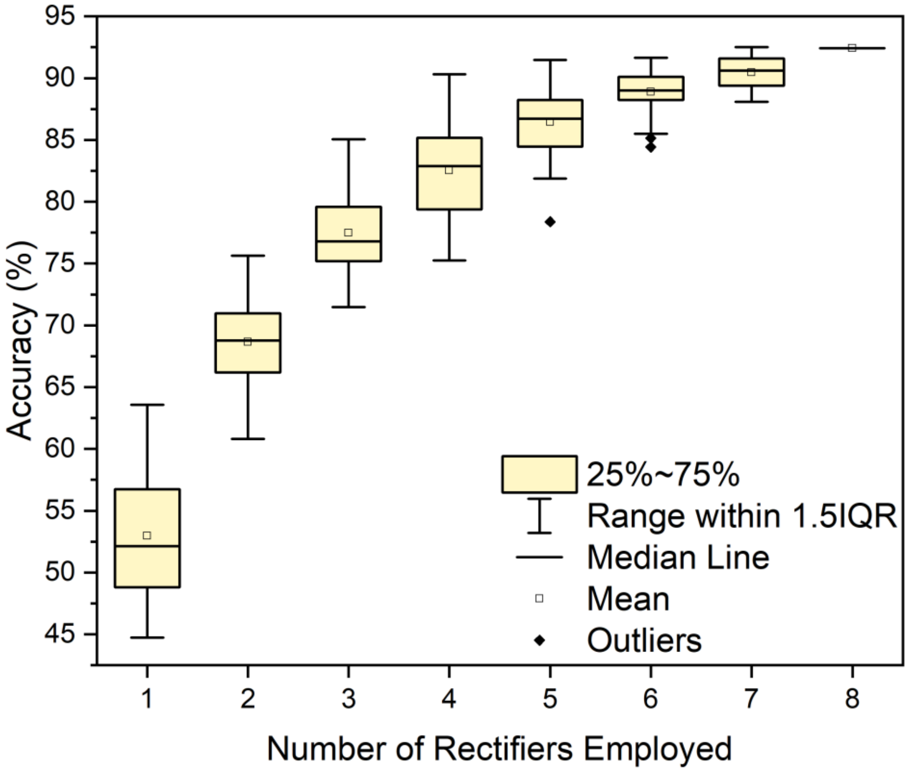

Supplementary Figure 93. The relationship between the combined horizontal localization accuracy of all three subjects and the number of rectifiers employed with dual-TX combination in Space3 with 6.9 m distance between the transmitter and the receiver.

Supplementary Table 9. Specific accuracies for different rectifier combinations in Horizontal Localization

Rectifier	Accuracy	Rectifier	Accuracy	Rectifier	Accuracy	Rectifier	Accuracy	Rectifier	Accuracy
1;	0.4474	1;5;6;	0.7479	1;2;5;7;	0.832	3;5;6;7;	0.7939	2;3;5;6;8;	0.832
2;	0.462	1;5;7;	0.7549	1;2;5;8;	0.7963	3;5;6;8;	0.7759	2;3;5;7;8;	0.8569
3;	0.5143	1;5;8;	0.736	1;2;6;7;	0.8162	3;5;7;8;	0.7914	2;3;6;7;8;	0.8261
4;	0.5642	1;6;7;	0.7822	1;2;6;8;	0.7723	3;6;7;8;	0.7852	2;4;5;6;7;	0.8679
5;	0.5163	1;6;8;	0.7147	1;2;7;8;	0.8301	4;5;6;7;	0.8088	2;4;5;6;8;	0.8725
6;	0.5704	1;7;8;	0.7507	1;3;4;5;	0.8294	4;5;6;8;	0.7931	2;4;5;7;8;	0.9079
7;	0.6357	2;3;4;	0.8245	1;3;4;6;	0.8727	4;5;7;8;	0.8421	2;4;6;7;8;	0.8673
8;	0.5266	2;3;5;	0.7523	1;3;4;7;	0.8639	4;6;7;8;	0.8358	2;5;6;7;8;	0.8436
1;2;	0.6156	2;3;6;	0.7632	1;3;4;8;	0.8639	5;6;7;8;	0.7524	3;4;5;6;7;	0.8482
1;3;	0.6507	2;3;7;	0.7743	1;3;5;6;	0.7887	1;2;3;4;5;	0.8768	3;4;5;6;8;	0.8434
1;4;	0.696	2;3;8;	0.7633	1;3;5;7;	0.831	1;2;3;4;6;	0.8967	3;4;5;7;8;	0.8625
1;5;	0.6448	2;4;5;	0.8	1;3;5;8;	0.7921	1;2;3;4;7;	0.9146	3;4;6;7;8;	0.8501
1;6;	0.7016	2;4;6;	0.8505	1;3;6;7;	0.8114	1;2;3;4;8;	0.9024	3;5;6;7;8;	0.7837
1;7;	0.7115	2;4;7;	0.8416	1;3;6;8;	0.8114	1;2;3;5;6;	0.8639	4;5;6;7;8;	0.8605
1;8;	0.6647	2;4;8;	0.8132	1;3;7;8;	0.7937	1;2;3;5;7;	0.8712	1;2;3;4;5;6;	0.907
2;3;	0.608	2;5;6;	0.7685	1;4;5;6;	0.8361	1;2;3;5;8;	0.8616	1;2;3;4;5;7;	0.9114
2;4;	0.6981	2;5;7;	0.7961	1;4;5;7;	0.8468	1;2;3;6;7;	0.8462	1;2;3;4;5;8;	0.893
2;5;	0.6481	2;5;8;	0.7394	1;4;5;8;	0.8254	1;2;3;6;8;	0.8454	1;2;3;4;6;7;	0.8958
2;6;	0.7287	2;6;7;	0.7865	1;4;6;7;	0.8102	1;2;3;7;8;	0.867	1;2;3;4;6;8;	0.8992
2;7;	0.7438	2;6;8;	0.7475	1;4;6;8;	0.8311	1;2;4;5;6;	0.8825	1;2;3;4;7;8;	0.903
2;8;	0.6534	2;7;8;	0.7965	1;4;7;8;	0.8464	1;2;4;5;7;	0.8922	1;2;3;5;6;7;	0.8705
3;4;	0.6694	3;4;5;	0.7743	1;5;6;7;	0.8071	1;2;4;5;8;	0.8778	1;2;3;5;6;8;	0.855
3;5;	0.6649	3;4;6;	0.8108	1;5;6;8;	0.7705	1;2;4;6;7;	0.8878	1;2;3;5;7;8;	0.8892
3;6;	0.6871	3;4;7;	0.8039	1;5;7;8;	0.7793	1;2;4;6;8;	0.8704	1;2;3;6;7;8;	0.8848
3;7;	0.7565	3;4;8;	0.8127	1;6;7;8;	0.7778	1;2;4;7;8;	0.9007	1;2;4;5;6;7;	0.8988
3;8;	0.6881	3;5;6;	0.7363	2;3;4;5;	0.8341	1;2;5;6;7;	0.855	1;2;4;5;6;8;	0.8843
4;5;	0.6839	3;5;7;	0.7527	2;3;4;6;	0.8917	1;2;5;6;8;	0.8403	1;2;4;5;7;8;	0.9025
4;6;	0.7168	3;5;8;	0.7509	2;3;4;7;	0.9031	1;2;5;7;8;	0.8426	1;2;4;6;7;8;	0.8786
4;7;	0.744	3;6;7;	0.7686	2;3;4;8;	0.879	1;2;6;7;8;	0.8358	1;2;5;6;7;8;	0.8581
4;8;	0.7498	3;6;8;	0.7466	2;3;5;6;	0.7769	1;3;4;5;6;	0.8695	1;3;4;5;6;7;	0.8994
5;6;	0.6648	3;7;8;	0.7825	2;3;5;7;	0.8366	1;3;4;5;7;	0.8812	1;3;4;5;6;8;	0.8891
5;7;	0.708	4;5;6;	0.7658	2;3;5;8;	0.7718	1;3;4;5;8;	0.882	1;3;4;5;7;8;	0.8905
5;8;	0.6588	4;5;7;	0.8014	2;3;6;7;	0.7929	1;3;4;6;7;	0.8758	1;3;4;6;7;8;	0.8896
6;7;	0.6939	4;5;8;	0.7848	2;3;6;8;	0.7877	1;3;4;6;8;	0.8674	1;3;5;6;7;8;	0.8442
6;8;	0.6684	4;6;7;	0.7595	2;3;7;8;	0.804	1;3;4;7;8;	0.8749	1;4;5;6;7;8;	0.886
7;8;	0.7053	4;6;8;	0.7475	2;4;5;6;	0.8518	1;3;5;6;7;	0.8327	2;3;4;5;6;7;	0.9118
1;2;3;	0.7956	4;7;8;	0.8217	2;4;5;7;	0.878	1;3;5;6;8;	0.8187	2;3;4;5;6;8;	0.8937
1;2;4;	0.7808	5;6;7;	0.7679	2;4;5;8;	0.8585	1;3;5;7;8;	0.8419	2;3;4;5;7;8;	0.9165
1;2;5;	0.7537	5;6;8;	0.74	2;4;6;7;	0.8655	1;3;6;7;8;	0.8277	2;3;4;6;7;8;	0.915
1;2;6;	0.7667	5;7;8;	0.7378	2;4;6;8;	0.8552	1;4;5;6;7;	0.8661	2;3;5;6;7;8;	0.8514
1;2;7;	0.7862	6;7;8;	0.7452	2;4;7;8;	0.8752	1;4;5;6;8;	0.8561	2;4;5;6;7;8;	0.8887
1;2;8;	0.7513	1;2;3;4;	0.8729	2;5;6;7;	0.8227	1;4;5;7;8;	0.8706	3;4;5;6;7;8;	0.8801
1;3;4;	0.7646	1;2;3;5;	0.8233	2;5;6;8;	0.7857	1;4;6;7;8;	0.8603	1;2;3;4;5;6;7;	0.9175
1;3;5;	0.7697	1;2;3;6;	0.8362	2;5;7;8;	0.8222	1;5;6;7;8;	0.8191	1;2;3;4;5;6;8;	0.9126
1;3;6;	0.7669	1;2;3;7;	0.8562	2;6;7;8;	0.8291	2;3;4;5;6;	0.8991	1;2;3;4;5;7;8;	0.925
1;3;7;	0.7655	1;2;3;8;	0.8518	3;4;5;6;	0.8266	2;3;4;5;7;	0.9064	1;2;3;4;6;7;8;	0.8994
1;3;8;	0.756	1;2;4;5;	0.8392	3;4;5;7;	0.84	2;3;4;5;8;	0.8871	1;2;3;5;6;7;8;	0.8809
1;4;5;	0.7677	1;2;4;6;	0.86	3;4;5;8;	0.8219	2;3;4;6;7;	0.9088	1;2;4;5;6;7;8;	0.8964
1;4;6;	0.7953	1;2;4;7;	0.872	3;4;6;7;	0.8103	2;3;4;6;8;	0.8919	1;3;4;5;6;7;8;	0.8912
1;4;7;	0.8259	1;2;4;8;	0.8616	3;4;6;8;	0.8057	2;3;4;7;8;	0.8918	2;3;4;5;6;7;8;	0.9141
1;4;8;	0.8309	1;2;5;6;	0.8289	3;4;7;8;	0.8345	2;3;5;6;7;	0.8339	1;2;3;4;5;6;7;8;	0.9242

Note 17.4 Summary of Conducted Experiments

To test the robustness and scalability of the horizontal localization system, the experiments were done in multiple spaces with different subjects employed. Experiments with diverse combinations of transmitters were also done to compare their performances. An overview of these experiments can be seen in Supplementary Table 5. The devices and deep learning model were fixed across all experiments.

For the experiment spaces with separation from 4.3 m to 9.7 m, the localization system can deal with the detection and have good performance. Compared to single centred TX and single side TX, the dual-TX combination shows significant improvement on the localization accuracy, especially for the detection of different subjects. The advancement mainly comes from wider electromagnetic wave coverage and stronger power levels. The high localization accuracy of different subject also indicates that the system can work well without specific retraining of different subjects. The relatively low result of Space 1 comes from the emptier room and consequently fewer reflection of electromagnetic wave, which informs that the layout of the room will also affect the performance of the system.

The setups and specific results will be illustrated later with the sequence of Space 1, Space 2, and Space 3. The research about the relationship between performance and number of rectifiers were done with the data gathered in Space 3 Long. A timeline experiment to show how the output voltage changes with subject moving in the detection zone will be shown latter as well.

Supplementary Note 18. Time-Varying Data and Real-Time Detection

To clearly show how the rectifier output voltage, normalized data and prediction result varies with the subject moving throughout the detection zone, timeline experiments were repeated for three subjects separately. Supplementary Figure 94 shows how the subject will move through the detection zone. The subject will stay in Zone1 before the experiment start, then moves to Zone 4 and walk back.

The rectifier voltage, normalized data and prediction result changing with time of different subjects are shown in Supplementary Figure 95-97. Some similar features of voltage variations for subject in specific zone can be seen in all three timeline graphs. The prediction result varying with time shows a good tracking effect result to the motion of subject.

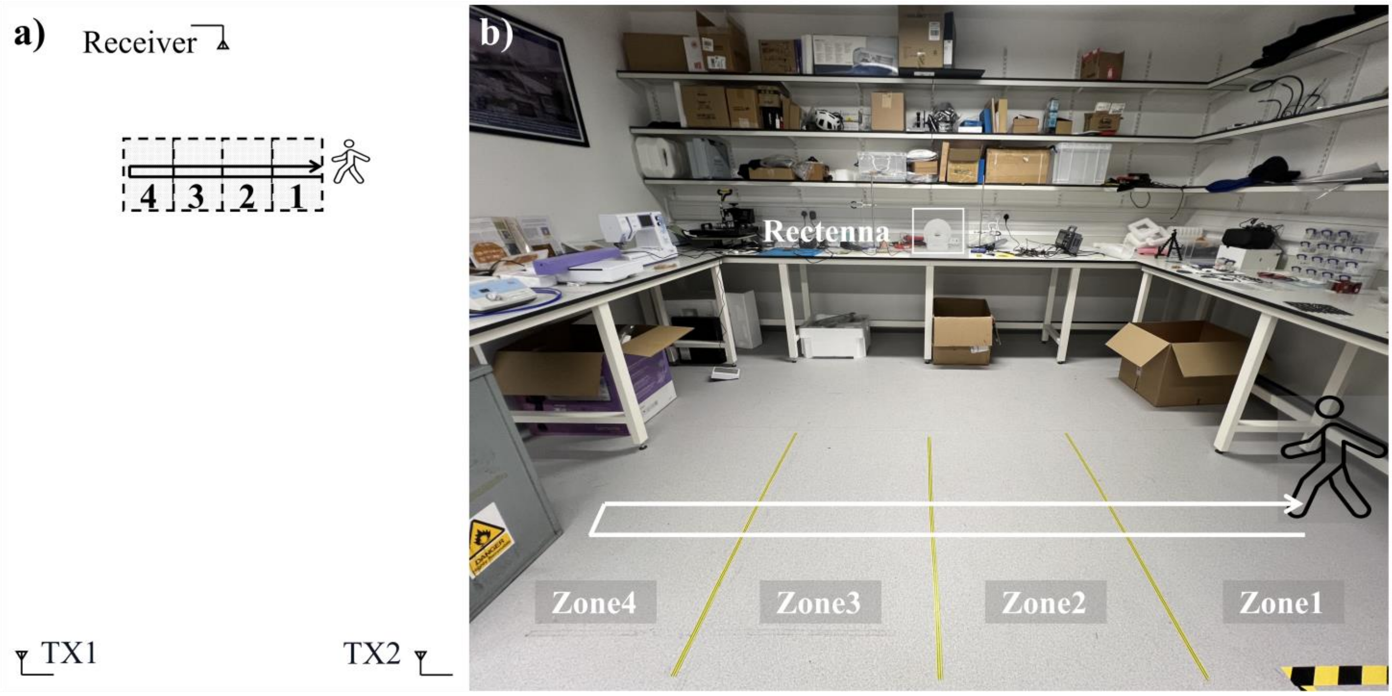

Supplementary Figure 94. Schematic (a) and photograph (b) of the horizontal localization in Space 2; Supplementary Video 3 shows the full experiment.

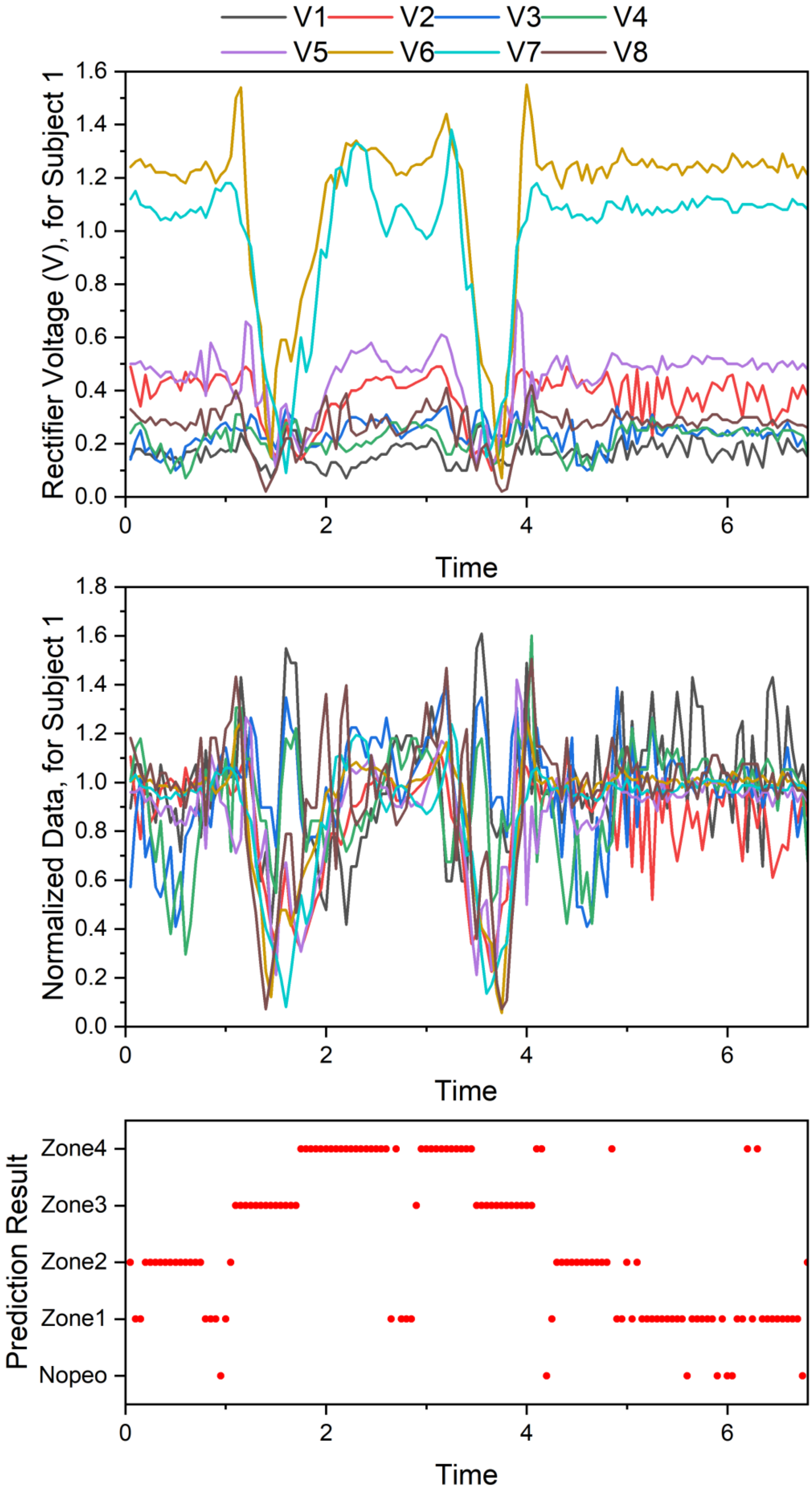

Supplementary Figure 95. The normalized data and prediction result varying with time of subject 1.

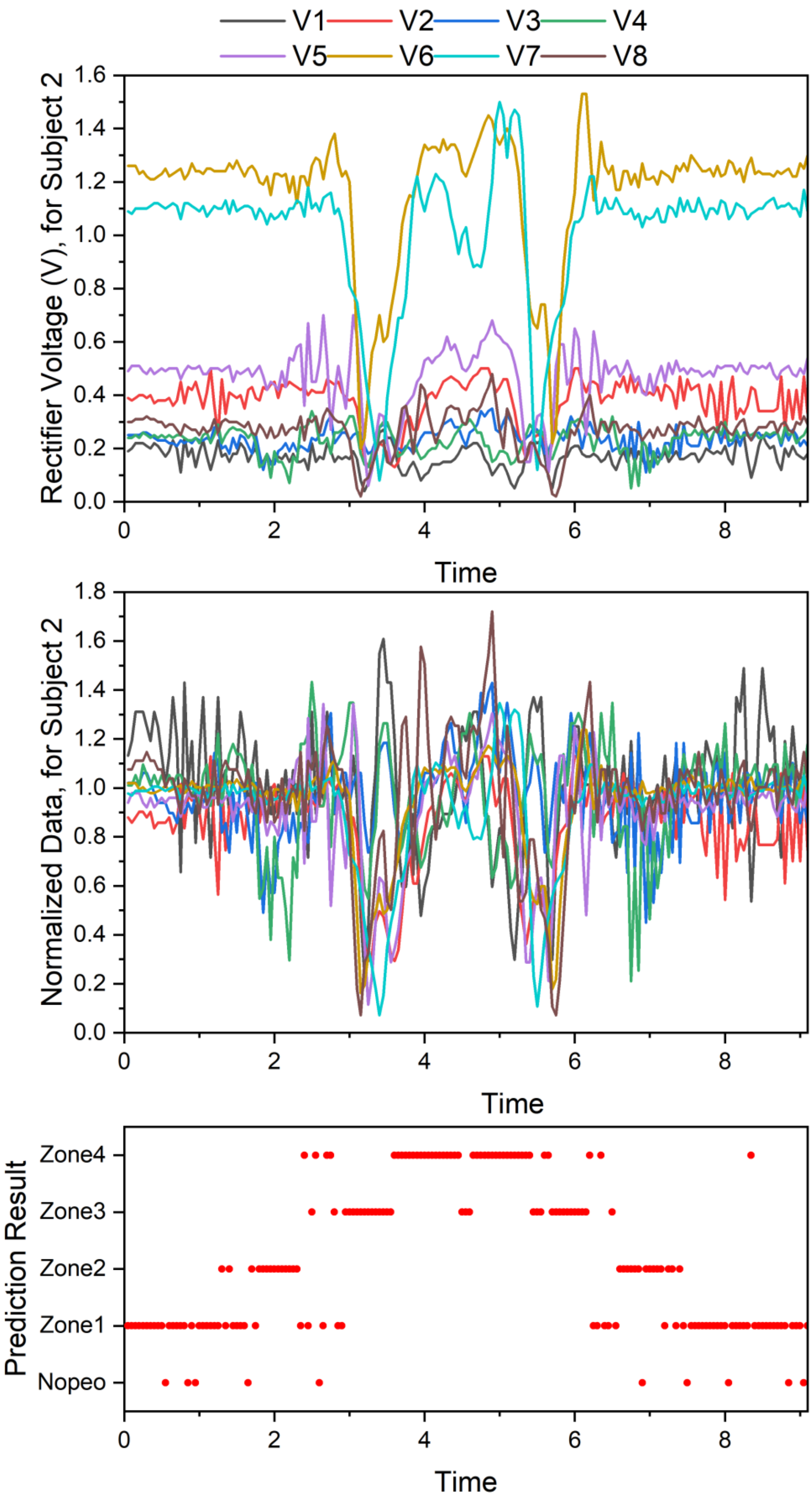

Supplementary Figure 96. The standardized data and prediction result varying with time of subject 2.

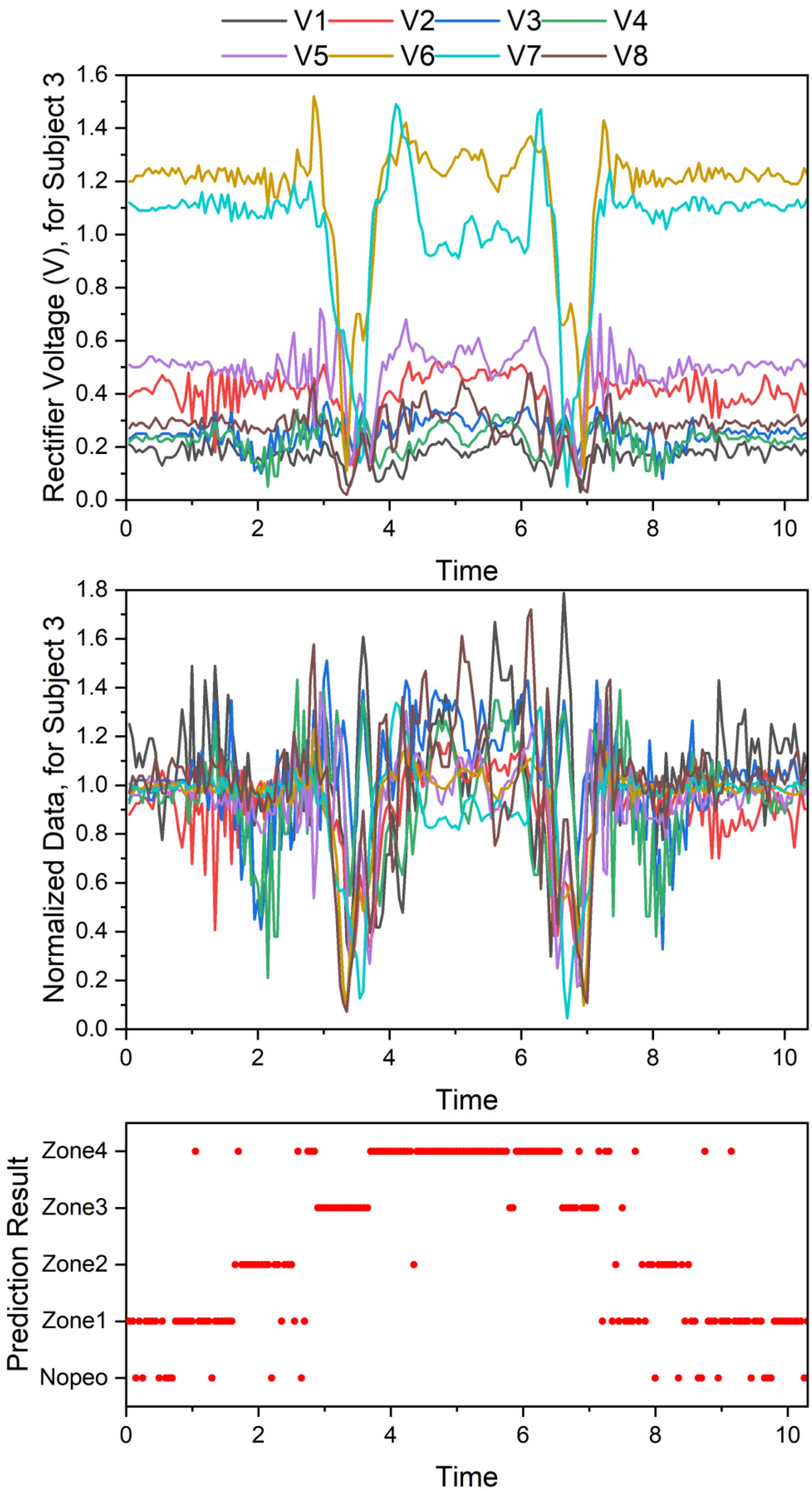

Supplementary Figure 97. The normalized data and prediction result varying with time of subject 3.

Supplementary Note 19. Power Consumption of Edge RF Sensing Receiver

To verify the feasibility of wirelessly powering of different receiver systems to fulfil data collection and Bluetooth transmission, the power consumptions of the two micro-controllers (Arduino Nano 33 BLE and Texas Instruments CC2640R2) employed were measured. The MCUs the eight DC output voltages through analogue digital conversion (ADC) and transmit these data through Bluetooth Low Energy (BLE) advertisement. During the working process, the MCU samples the 8 DC rectenna output voltages, store them as uint_8 type, and advertise the sampled data through BLE function. The current consumption was measured across a 10 Ω current-sense series resistor. The Arduino Nano 33 BLE supply was kept at 1.8 V with the Texas Instruments CC2640R2 maintained at 2 V DC voltage.

The ADC-sampling functionalities were tested on both microcontrollers as shown in Supplementary Figure 98 and 99(a). The ADC-sampling process can be fulfilled within 15 ms. The power consumptions of the analogue digital conversion (ADC) and the BLE broadcasting function in one period can be seen in Supplementary Figure 99. The instantaneous power consumption over time in multiple periods can be seen in Supplementary Figure 100. The average power consumption over a 10 s period is 0.30 mW.

With up to 37 available bytes in a standard BLE advertisement, it is possible to encode the instantaneous voltage readings from up to 12 ADC channels. With most MCUs having up to 12 ADC channels, a BLE beacon-based readout is sufficient to collect the data required for ML-based localization and transmitting it to a BLE gateway connected to a PC, or a BLE-enabled smartphone. Given the 2.4 GHz carrier and 0 dBm transmitted power level, a communication range of 20-100 m could be maintained.

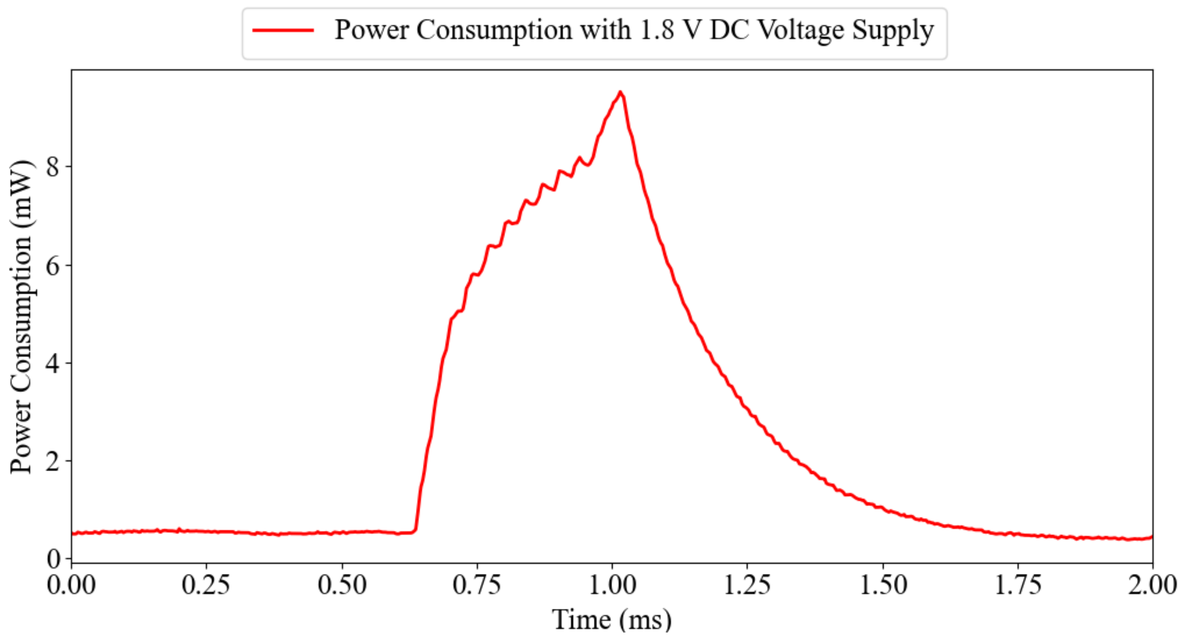

Supplementary Figure 98. The measured power consumption of the nRF52840 (Arduino BLE Nano)-based data sampling MCU.

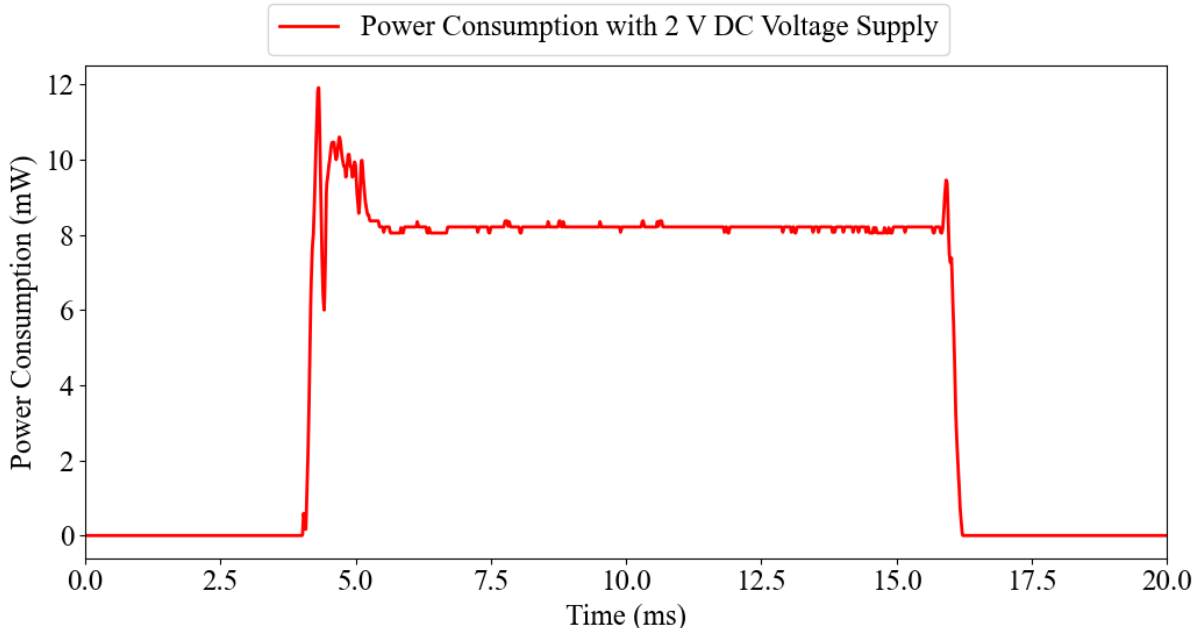

(a)

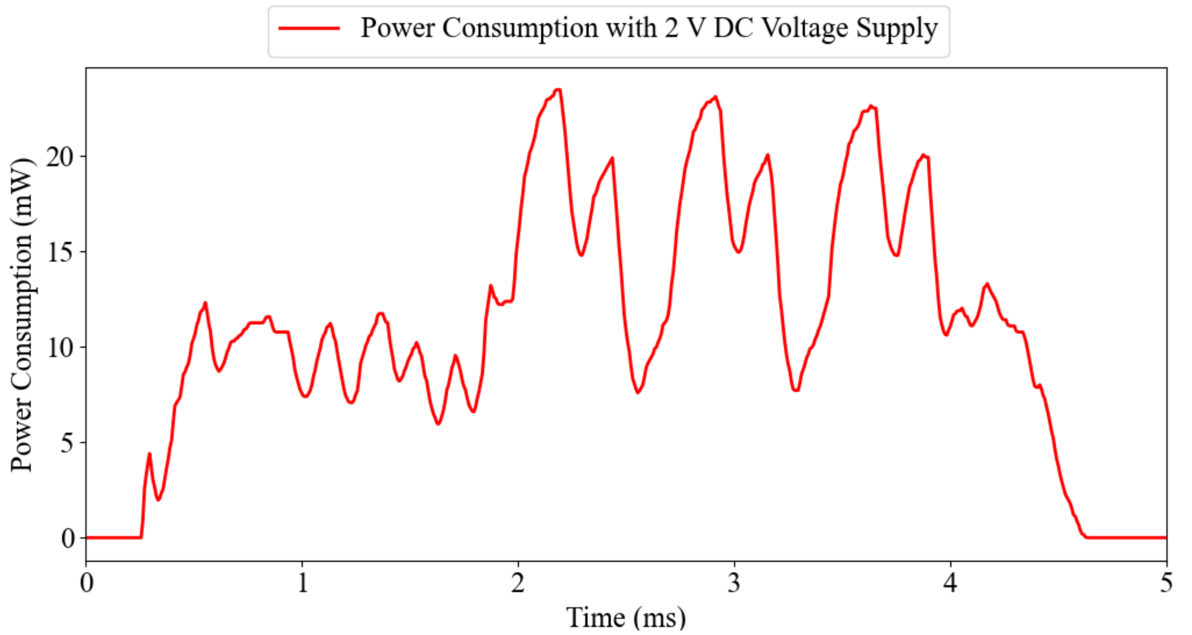

(b)

Supplementary Figure 99. Power consumption of two functions in one period, using the IT CC2640-R2F. (a) ADC sampling; (b) BLE advertising.

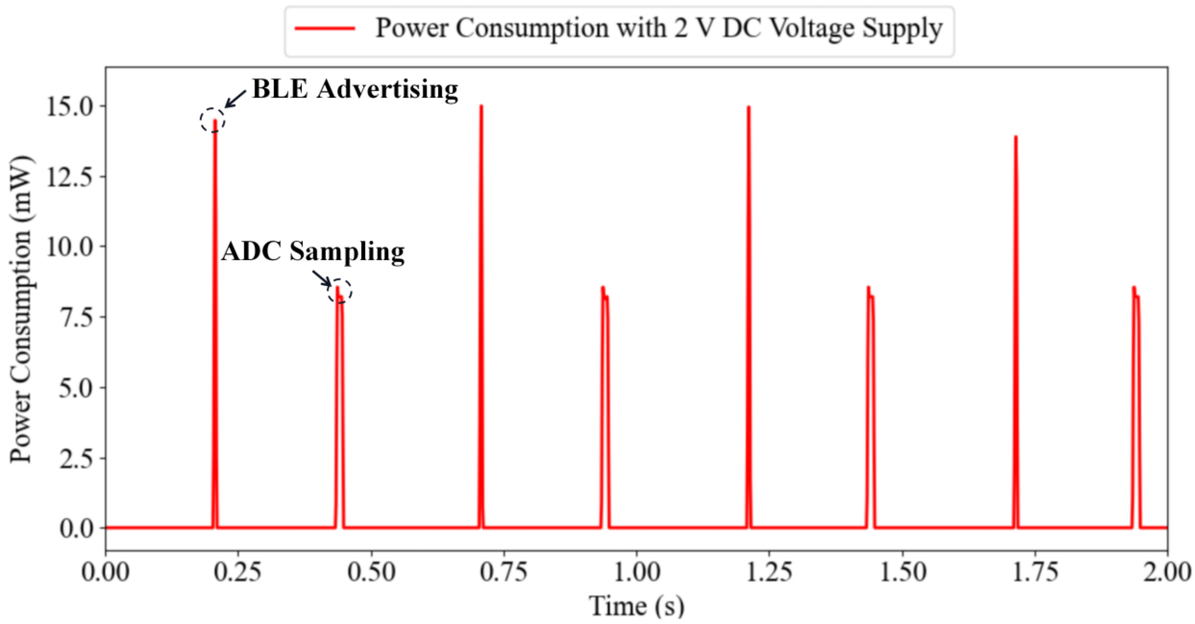

Supplementary Figure 100. Power consumption of the ADC sampling and BLE advertisements over multiple sampling and advertising periods.

Supplementary Videos Details

Supplementary Video 1: DC power pattern measurements in an anechoic chamber.

Supplementary Video 2: Long-range Bluetooth tag powering demo showing uninterrupted operation with LoS obstruction.

Supplementary Video 3: Real-time horizontal localisation in Setup 3.

Supplementary References:

[S1] Nadeem Javed, Ngoc-Luu Nguyen, Syed Farhan Ali Naqvi, and Jinyong Ha, "Long-range wireless optical power transfer system using an EDFA," *Opt. Express* 30, 33767-33779 (2022)

[S2] Wang, Y., Zheng, Z., Wang, J. et al. Organic laser power converter for efficient wireless micro power transfer. *Nat Commun* 14, 5511 (2023). https://doi.org/10.1038/s41467-023-41270-1

[S3] Zhang, X., Grajal, J., Vazquez-Roy, J.L. et al. Two-dimensional MoS2-enabled flexible rectenna for Wi-Fi-band wireless energy harvesting. *Nature* 566, 368–372 (2019). https://doi.org/10.1038/s41586-019-0892-1

[S4] E. Vandelle, D. H. N. Bui, T. -P. Vuong, G. Ardila, K. Wu and S. Hemour, "Harvesting Ambient RF Energy Efficiently With Optimal Angular Coverage," in IEEE Transactions on Antennas and Propagation, vol. 67, no. 3, pp. 1862-1873, March 2019, doi: 10.1109/TAP.2018.2888957.

[S5] M. Wagih and S. Beeby, "Thin Flexible RF Energy Harvesting Rectenna Surface With a Large Effective Aperture for Sub μW/cm2 Powering of Wireless Sensor Nodes," in IEEE Transactions on Microwave Theory and Techniques, vol. 70, no. 9, pp. 4328-4338, Sept. 2022, doi: 10.1109/TMTT.2022.3192532.

[S6] Z. Popović et al., "Scalable RF Energy Harvesting," in *IEEE Transactions on Microwave Theory and Techniques*, vol. 62, no. 4, pp. 1046-1056, April 2014, doi: 10.1109/TMTT.2014.2300840.

[S7] F. Erkmen, T. S. Almoneef and O. M. Ramahi, "Electromagnetic Energy Harvesting Using Full-Wave Rectification," in *IEEE Transactions on Microwave Theory and Techniques*, vol. 65, no. 5, pp. 1843-1851, May 2017, doi: 10.1109/TMTT.2017.2673821.

[S8] V. Palazzi et al., "A Novel Ultra-Lightweight Multiband Rectenna on Paper for RF Energy Harvesting in the Next Generation LTE Bands," in *IEEE Transactions on Microwave Theory and Techniques*, vol. 66, no. 1, pp. 366-379, Jan. 2018, doi: 10.1109/TMTT.2017.2721399.

[S9] Sasatani, T., Sample, A.P. & Kawahara, Y. Room-scale magnetoquasistatic wireless power transfer using a cavity-based multimode resonator. *Nat Electron* 4, 689–697 (2021). https://doi.org/10.1038/s41928-021-00636-3

[S10] M. Rajendran, J. E. H. Yang, J. L. Kaibin, L. C. Ping and S. Y. Huang, "Birdcage Transmitter for Wireless Power Transfer," in *IEEE Microwave and Wireless Components Letters*, vol. 32, no. 7, pp. 919-922, July 2022, doi: 10.1109/LMWC.2022.3153669.

[S11] W. Shao et al., "Graded-Index-Fiber-Inspired 3-D Printed Surface Focusing Porous Dielectric Structure With GaAs MMIC Rectenna Toward Millimeter-Wave Wireless Power Transfer Application," in *IEEE Antennas and Wireless Propagation Letters*, vol. 22, no. 12, pp. 3177-3181, Dec. 2023, doi: 10.1109/LAWP.2023.3312691.

[S12] A. Eid, J. Hester and M. M. Tentzeris, "Extending the Range of 5G Energy Transfer: Towards the Wireless Power Grid," *2022 16th European Conference on Antennas and Propagation (EuCAP)*, Madrid, Spain, 2022, pp. 1-4, doi: 10.23919/EuCAP53622.2022.9769572.

[S13] Eid, A., Hester, J.G.D. & Tentzeris, M.M. 5G as a wireless power grid. *Sci Rep* **11**, 636 (2021). https://doi.org/10.1038/s41598-020-79500-x

[S14] F. Deng and K. M. Luk, "A Broadband High-Gain Multibeam Ambient Millimeter-Wave Energy-Harvesting System," in *IEEE Internet of Things Journal*, vol. 11, no. 3, pp. 4888-4898, 1 Feb.1, 2024, doi: 10.1109/JIOT.2023.3301536.

[S15] K. Matsui *et al*., "Development of 94GHz microstrip line rectenna," *2018 IEEE Wireless Power Transfer Conference (WPTC)*, Montreal, QC, Canada, 2018, pp. 1-4, doi: 10.1109/WPT.2018.8639081.

[S16] Y. Wang *et al*., "Highly Efficient Broadband Ambient Energy Harvesting System Enhanced by Meta-Lens for Wirelessly Powering Batteryless IoT Devices," in *IEEE Internet of Things Journal*, vol. 11, no. 16, pp. 26916-26928, 15 Aug.15, 2024, doi: 10.1109/JIOT.2023.3328209.

[S17] A. -H. Hobballah, R. Négrier and M. Lalande, "A Dielectric Lens Rectenna for Wireless Power Transmission," *2021 51st European Microwave Conference (EuMC)*, London, United Kingdom, 2022, pp. 672-675, doi: 10.23919/EuMC50147.2022.9784274.

[S18] J. Budhu, Y. Rahmat-Samii, R. E. Hodges, D. C. Hofmann, D. F. Ruffatto and K. C. Carpenter, "Three-Dimensionally Printed, Shaped, Engineered Material Inhomogeneous Lens Antennas for Next-Generation Spaceborne Weather Radar Systems," in IEEE Antennas and

Wireless Propagation Letters, vol. 17, no. 11, pp. 2080-2084, Nov. 2018, doi: 10.1109/LAWP.2018.2848263
[S19] J. M. Monkevich and G. P. Le Sage, "Design and Fabrication of a Custom-Dielectric Fresnel Multi-Zone Plate Lens Antenna Using Additive Manufacturing Techniques," in *IEEE Access*, vol. 7, pp. 61452-61460, 2019, doi: 10.1109/ACCESS.2019.2916077.
[S20] Zhang, S., Arya, R.K., Pandey, S., Vardaxoglou, Y., Whittow, W. and Mittra, R. (2016), 3D-printed planar graded index lenses. IET Microw. Antennas Propag., 10: 1411-1419. https://doi.org/10.1049/iet-map.2016.0013
[S21] Poyanco, J.-M.; Pizarro, F.; Rajo-Iglesias, E. 3D-Printing for Transformation Optics in Electromagnetic High-Frequency Lens Applications. *Materials* **2020**, *13*, 2700. https://doi.org/10.3390/ma13122700
[S22] Y. -H. Lou, Y. -X. Zhu, G. -F. Fan, W. Lei, W. -Z. Lu and X. -C. Wang, "Design of Ku-Band Flat Luneburg Lens Using Ceramic 3-D Printing," in *IEEE Antennas and Wireless Propagation Letters*, vol. 20, no. 2, pp. 234-238, Feb. 2021, doi: 10.1109/LAWP.2020.3046489.
[S23] M. Liang, W. -R. Ng, K. Chang, K. Gbele, M. E. Gehm and H. Xin, "A 3-D Luneburg Lens Antenna Fabricated by Polymer Jetting Rapid Prototyping," in *IEEE Transactions on Antennas and Propagation*, vol. 62, no. 4, pp. 1799-1807, April 2014, doi: 10.1109/TAP.2013.2297165.
[S24] Ma, H., Cui, T. Three-dimensional broadband and broad-angle transformation-optics lens. *Nat Commun* **1**, 124 (2010). https://doi.org/10.1038/ncomms1126
[S25] E. Erfani, M. Niroo-Jazi and S. Tatu, "A High-Gain Broadband Gradient Refractive Index Metasurface Lens Antenna," in *IEEE Transactions on Antennas and Propagation*, vol. 64, no. 5, pp. 1968-1973, May 2016, doi: 10.1109/TAP.2016.2526052.
[S26] Y. Wang and Y. Zheng, "TagBreathe: Monitor Breathing with Commodity RFID Systems," in *IEEE Transactions on Mobile Computing*, vol. 19, no. 4, pp. 969-981, 1 April 2020, doi: 10.1109/TMC.2019.2900214.
[S27] M. C. Caccami, M. Y. S. Mulla, C. Occhiuzzi, C. Di Natale and G. Marrocco, "Design and Experimentation of a Batteryless On-Skin RFID Graphene-Oxide Sensor for the Monitoring and Discrimination of Breath Anomalies," in *IEEE Sensors Journal*, vol. 18, no. 21, pp. 8893-8901, 1 Nov.1, 2018, doi: 10.1109/JSEN.2018.2867208.
[S28] D. Patron et al., "On the Use of Knitted Antennas and Inductively Coupled RFID Tags for Wearable Applications," in *IEEE Transactions on Biomedical Circuits and Systems*, vol. 10, no. 6, pp. 1047-1057, Dec. 2016, doi: 10.1109/TBCAS.2016.2518871.
[S29] Y. Liu et al., "E-Textile Battery-Less Displacement and Strain Sensor for Human Activities Tracking," in *IEEE Internet of Things Journal*, vol. 8, no. 22, pp. 16486-16497, 15 Nov.15, 2021, doi: 10.1109/JIOT.2021.3074746.
[S30] Khan, M.Z., Usman, M., Ahmad, J. et al. Tag-free indoor fall detection using transformer network encoder and data fusion. *Sci Rep* 14, 16763 (2024). https://doi.org/10.1038/s41598-024-67439-2
[S31] Wagih, M., Shi, J., Li, M. et al. Wide-range soft anisotropic thermistor with a direct wireless radio frequency interface. *Nat Commun* 15, 452 (2024). https://doi.org/10.1038/s41467-024-44735-z
[S32] J. G. D. Hester and M. M. Tentzeris, "Inkjet-Printed Flexible mm-Wave Van-Atta Reflectarrays: A Solution for Ultralong-Range Dense Multitag and Multisensing Chipless RFID Implementations for IoT Smart Skins," in *IEEE Transactions on Microwave Theory and Techniques*, vol. 64, no. 12, pp. 4763-4773, Dec. 2016, doi: 10.1109/TMTT.2016.2623790.
[S33] Mercuri, M., Lorato, I.R., Liu, YH. et al. Vital-sign monitoring and spatial tracking of multiple people using a contactless radar-based sensor. *Nat Electron* 2, 252–262 (2019). https://doi.org/10.1038/s41928-019-0258-6
[S34] “NOVELDA UWB Occupancy Sensor” Online [Available: https://novelda.com/ultra-wideband-occupancy-sensor/], accessed 14/7.
[S35] Ni et al. “Towards Battery-Free Wireless Sensing via Radio-Frequency Energy Harvesting” *preprint Arxiv,* (2024) https://arxiv.org/abs/2409.00086
[S36] D. Ma, G. Lan, M. Hassan, W. Hu and S. K. Das, "Sensing, Computing, and Communications for Energy Harvesting IoTs: A Survey," in *IEEE Communications Surveys & Tutorials*, vol. 22, no. 2, pp. 1222-1250, Secondquarter 2020, doi: 10.1109/COMST.2019.2962526.

[S37] “Ambient Power-enabled IoT Second Edition of “Zero Power Communication”” Online [Available: https://www.oppo.com/content/dam/oppo/common/mkt/footer/Ambient-Power-enabled-IoT-White-Paper.pdf] Accessed: 3/5/2026

[S38] Jameel F., Ristaniemi T., Khan K., Lee I. “Simultaneous Harvest-and-Transmit Ambient Backscatter Communications under Rayleigh Fading,” *EURASIP J. Wireless Commun. Netw*., 2019.

[S39] Zhou Z., Li X., Zhu G., Xu J., Huang K., Cui S. “Integrating Sensing, Communication, and Power Transfer: Multiuser Beamforming Design,” *arXiv*:2311.09028 (2023).

[S40] Ni, Tao, et al. “Towards Battery-Free Wireless Sensing via Radio-Frequency Energy Harvesting.” arXiv:2409.00086, *arXiv*, 26 Aug. 2024. arXiv.org, https://doi.org/10.48550/arXiv.2409.00086.

[S41] A. J. Soares Boaventura, A. Collado, A. Georgiadis and N. Borges Carvalho, "Spatial Power Combining of Multi-Sine Signals for Wireless Power Transmission Applications," in IEEE Transactions on Microwave Theory and Techniques, vol. 62, no. 4, pp. 1022-1030, April 2014, doi: 10.1109/TMTT.2014.2300452.